Copyright

by

Patrick Loring Hanks

2008

The Dissertation Committee for Patrick Loring Hanks Certifies that this is the approved version of the following dissertation:

Post Coarsening Effects on Membrane Microstructure

Committee:

Douglas Lloyd, Supervisor

Eric Becker

Roger Bonnecaze

Benny Freeman

Nicholas Peppas

Post Coarsening Effects on Membrane Microstructure

by

Patrick Loring Hanks, BChE

Dissertation

Presented to the Faculty of the Graduate School of
The University of Texas at Austin
in Partial Fulfillment
of the Requirements
for the Degree of

Doctor of Philosophy

The University of Texas at Austin
May, 2008

Dedication

To my friends and family.

Acknowledgements

Thanks are due to a number of people including: my advisor, Douglas Lloyd; my committee members of Eric Becker, Roger Bonnecaze, Benny Freeman, and Nicolas Peppas; my undergraduate colleagues of Kelsie Kaczorowski and Caitlin Forshner; my labmate, sounding board, friend and compatriot for four years Caleb Funk; and my beautiful wife Rose Marie.

Post Coarsening Effects on Membrane Microstructure

Publication No._____________

Patrick Loring Hanks, PhD
The University of Texas at Austin, 2008

Supervisor: Douglas Lloyd

The goal of this research was to determine relationships between post-coarsening processing conditions and the microporous morphology of membranes. Specifically, the processes of matrix solidification in liquid – liquid thermally induced phase separation (L−L TIPS), the drying of the microporous structure, and the uni-axial elongation of a simple microporous structure were examined. Additionally, the effect uni-axial elongation has on pore shape was included in a sieve filtration model to look at the impact on performance.

A deterministic approach was taken to predict membrane morphologies resulting from the matrix solidification step that occurs in L–L TIPS. Many studies have examined the growth rate of droplets in the coarsening stage of membrane formation, but few have attempted to extend this information into the subsequent processing steps of matrix solidification, diluent extraction/exchange, and drying. The modeling of matrix solidification utilized Monte-Carlo routines to provide quantitative information on cell size and cell size distribution for a representative polymer – diluent system. The predicted structures were in agreement with experimentally formed membranes.

The information gained from matrix solidification modeling was used to make finite element (FE) simulations in ABAQUS CAE to model the drying of the microporous morphology, with capillary forces being the dominant force driving shrinkage and collapse of the structure. These FE simulations predicted no permanent deformation arising from only capillary forces, which was confirmed through experimental evidence showing no correlation to surface tension. For polar polymers an additional heuristic was proposed: use extractants that are more alkane-like, regardless of surface tension, to reduce the collapse of the structure.

FE simulations were used to model the uni-axial elongation of track-etch membranes in an effort to change performance characteristics. The FE simulations accurately predicted pore shape changes comparable to experimental values. The pore shape change information was used to modify standard sieve filtration models. The modified sieve filtration models show that a relatively modest strain of 35% can double the initial flux of track-etch membranes.

Table of Contents

List of Tables xi

List of Figures xii

Chapter 1: Introduction 1

1.1 Hypothesis and Objectives of Research 1
1.2 Membrane Applications 3
1.3 Significance of the work 4
1.4 Structure of the dissertation 5
1.5 References 5

Chapter 2: Matrix Solidification in L – L TIPS 8

2.1 introduction 8
2.1 Model Development 10
  2.2.1 Physical Steps occurring during L – L TIPS 10
  2.2.2 Modeling Procedure 12
2.2 Materials and Methods 25
  2.2.1 Materials 25
  2.2.2 Experimental Procedure 25
2.3 Results and discussion 26
2.4 Conclusions 31
2.5 References 32

Chapter 3: Drying of Microporous Membranes 36

3.1 Introduction 36
3.2 Model Development 40
  3.2.1 Modeling Approach 40
  3.2.2 Part Generation and Mesh 40
  3.2.3 Material Property Models 43
  3.2.4 Forces and Boundary Conditions 44
  3.2.5 Available Drying Rate Models 48

3.2.6 Simulation Steps 51
3.3 Model Results and Discussion 52
3.3.1 Deformation Results 52
3.3.2 Potential Forces and Phenomena in the System 53
3.4 Experimental Materials and Methods 59
3.4.1 Materials 59
3.4.2 Physical Property Determination 60
3.4.3 Drying Experimental Procedure 61
3.5 Experimental Results And Discussion 62
3.6 Conclusion 67
3.7 References 69

Chapter 4: Modeling uni-axial elongation of track-etch membranes 72
4.1 Introduction 72
4.1.1 Void Growth Models 74
4.2 Materials and Methods 75
4.2.1 Materials 75
4.2.2 Experimental Procedures 76
4.2.3 Modeling 78
4.3 Results and Discussion 84
4.4 Conclusion 90
4.5 References 90

Chapter 5: Performance Effects of Pore Shape Change 93
5.1 Introduction 93
5.1.1 Basic Sieve Mechanism Model for Circular pores 94
5.2 Modeling Methods 98
5.2.1 Modified Sieve Mechanism for Elliptical pores 98
5.2.2 Discrete method for modeling circular pores 102
5.2.3 Discrete method for modeling elliptical pores 102
5.2.4 Flow through partially blocked elliptical pores 102
5.2.5 Distribution Determination 106

5.3 Results and Discussion 107

5.3.1 Circular pore results..107

5.3.2 Elliptical pore results 108

5.4 Conclusions..114

5.6 References..116

Chapter 6: Conclusions and Recommendations 118

6.1 Conclusions..118

6.1.1 Matrix Solidification..118

6.1.2 Drying of Microporous Membranes 119

6.1.3 Modeling uni-axial elongation of TE membranes 119

6.1.4 Performance effects of pore shape change..120

6.2 Recommendations for Future Work..120

6.3 References..123

Appendix A: Nomenclature 124

Appendix B: Program Code..127

Appendix C: Shrinkage dependence on extractant parameters..129

Bibliography 139

Vita..148

List of Tables

Table 2.1: Initial starting conditions for solidification of iPP–DPE 14

Table 2.2: Parameters used to calculate the diffusion coefficient of DPE in an iPP–DPE liquid matrix 18

Table 3.1: Physical response parameters of studied polymers obtained through experiments described in section 3.4.2 44

Table 4.1: Physical characteristics of the PET TE membranes. 76

Table 4.2: Material properties of PET 81

Table 5.1: The blockage factor is the fraction of unfouled flux for a pore with a given aspect ratio and a given particle to minor axis ratio. 105

Table 5.2: Distribution parameters of the 0.6 μm membranes represented by normal distributions................................107

Table 5.3: Distribution parameters of particles represented by normal distributions......107

List of Figures

Figure 2.1: The cellular morphology 9

Figure 2.2: iPP – DPE phase diagram...12

Figure 2.3: Simplified schematic of the steps included in the simulation. 16

Figure 2.4: Viscosity (Pa*s) of iPP – DPE system as a function of temperature. 20

Figure 2.5: The growth of the polymer-lean droplets and the polymer-rich matrix solidification lead from isolated droplets to a co-continuous structure. 24

Figure 2.6: Cell diameter as a function of time in the liquid – liquid region for four representative starting polymer-lean volume fractions (Phi). 30

Figure 3.1: The effect of extractant surface tension on final relative volume 38

Figure 3.2: The predominant force in collapsing a cell is the capillary forces 39

Figure 3.3: A geometrically repeating unit 41

Figure 3.4: This simple object shows the mesh of tetrahedrals in the midst of drying 42

Figure 3.5: A simple schematic of a cell divided into four sections for computation of capillary forces 45

Figure 3.6: Extreme distortion on an arm of elements can result in solution algorithms breaking down due to extreme stress and distortion of elements 46

Figure 3.7: By eliminating the shared edges between part faces, errors in ABAQUS could be avoided to allow the analysis to proceed...48

Figure 3.8: Stress is developed as the structure collapses under capillary force, but only results in elastic deformation, allowing the structure to return to its original configuration after drying is complete 53

Figure 3.9: The shape of a meniscus in a hollow sphere for a fluid with a contact angle of 20° 55

Figure 3.10: In figure 10a (top) there is a noticeable size difference between cells in the interior and exterior of the membrane that is not observed with other extractants, like cyclohexane pictured in 10b (bottom) 58

Figure 3.11: EVAL – glycerol phase diagram from Shang *et al*. [34].............................60

Figure 3.12: Acetone on an EVAL44 film..62

Figure 3.13: EVAL44–glycerol membranes formed at different temperatures and compositions exhibit no correlation with surface tension..63

Figure 3.14: The shrinkage of EVAL44 – glycerol membranes show no definitive trend with the index of refraction of the extractant..64

Figure 3.15: The shrinkage of EVAL44 – glycerol membranes show no definitive trends with solubility parameters...65

Figure 3.16: EVAL44 50-50 wt%, 150°F membranes show no correlation between cell diameter and surface tension..66

Figure 4.1: Cross-sectional and top view of 2 μm TE PET..78

Figure 4.2: The experimentally measured minor axis (a) and angle from normal (b) distributions for the pores of the 2 μm PET membranes 79

Figure 4.3: The experimentally determined stress–strain response curve of the dense PET film..80

Figure 4.4: A sample 2D model of the TE membranes containing 64 pores.....................83

Figure 4.6: Comparison of 3D and 2D results for 8-pore 2 μm model.............................86

Figure 4.7: Comparison of 2D model and experimental results for the membrane with a nominal reported pore diameter of 2 μm 87

Figure 4.8: Comparison of 2D model and experimental results for the membrane with a nominal reported pore diameter of 10 μm 88

Figure 4.9: Comparison of 2D model and experimental results for the membrane with a nominal reported pore diameter of 0.6 μm 89

Figure 5.1: Schematic presentation of the MF sieving process 94

Figure 5.2: A graphical representation of β for a single circular pore..............................96

Figure 5.3: Schematic presentation of the MF sieving process 99

Figure 5.4: Definition of characteristic lengths of an elliptical pore. 99

Figure 5.5: A comparison of the solution for velocity profile along the major axis for the elliptical pore and the velocity profile from Stoke's flow around a sphere....................104

Figure 5.6: A graphical representation of the data in Table 5.1, showing the effect of aspect ratio and particle size ratio on flow through a partially blocked pore. 106

Figure 5.7: The difference between Equation 5.9 and the discrete model......................108

Figure 5.8: The particle distributions and distributions of minor axis used in the models for the 0.6 μm PET TE membrane. 109

Figure 5.9: The effect of stretching on initial flux and flux decline for a 0.6 micron PET membrane with 0.652 micron particles in the feed. 111

Figure 5.10: Experimental data corresponding to conditions in Figure 5.9....................112

Figure 5.11: A 0.6 μm membrane at various strains fed particles with an average size of 1 μm and a standard deviation of 0.05 μm..113

Figure 5.12: Volume of permeate generated over time 114

Chapter 1: Introduction

1.1 HYPOTHESIS AND OBJECTIVES OF RESEARCH

Microporous materials are widely used in a variety of applications such as microfiltration [1], water treatment [2], blood oxygenation [3], plasma separation [4] and controlled release devices [5]. There is interest in understanding the fundamentals of membrane formation in order to be able to create new membranes and control membrane structure for exisiting and potential new applications. A major concern in developing new membranes is the long lead times for production and the amount of resources consumed. As heat transfer is generally one to two orders of magnitude faster than mass transfer, thermally induced phase separation (TIPS) membranes are of interest to the community [6]. Membranes produced by liquid – liquid (L–L) TIPS are of particular interest because of the potential for high porosity membranes with substantial strength. The TIPS process is also industrially advantageous because it is a binary system, does not form macrovoid defects, and can be produced with a relatively uniform cell size.

The TIPS process begins by heating a polymer and a diluent to a sufficiently high temperature to melt-blend the components into a homogenous phase [7-9]. The diluent is a low molecular weight, high-boiling point chemical that is not a solvent for the polymer at room temperature, but acts as one at higher temperatures. When the homogenous blend is cooled, it undergoes phase separation. Through the appropriate choice of diluent and initial polymer concentration [10-12], the solution undergoes L–L TIPS to form a dispersed diluent-rich phase inside of the polymer-rich matrix phase. Further quenching solidifies the matrix phase establishing the base morphology of the membrane. Steps of extraction exchange to remove the high-boiling point diluent and the evaporation of the extractant can lead to changes in the morphology of the membrane and complete the production process.

Uni-axial elongation of membranes, whether they are produced via TIPS, non-solvent induced phase separation, or through a track-etch process, is an optional post-production process [13-15]. Uni-axial elongation is used to manipulate the morphology to change a variety of performance properties. Recent studies have shown that the pore geometry affects the fouling of membranes by changing the cake growth patterns [16]. Previous work in our research group have shown that uni-axial elongation can increase initial flux, and reduce the amount of flux decline during particulate microfiltration [17, 18].

The performance of a microporous membrane is determined by six primary factors: membrane material, pore size, pore size distribution, porosity, surface roughness, and tortuosity. The membrane material is the only performance factor that does not fall under the category of morphology. Rather, membrane material falls under a separate category of membrane chemistry. The ability for certain fluids to wet the membrane and the particulate affinity for the membrane are a function of the material type, polarity, and surface charge. The mechanical properties, namely the strength of the polymer and the glass transition temperature, and the chemical resistance of the material are also considered when selecting an appropriate material for a specific application. Additionally, the fluid flow patterns produced by membrane module design will impact the performance of the membrane. However, the manipulation of the morphology provides the largest opportunity to affect performance.

There is a definable and quantifiable relationship between membrane production conditions and the resulting microporous morphologies. The objective of this work is to describe and model steps of microporous membrane production and the resulting impact on performance. Specifically, the steps of matrix solidification in L – L TIPS in which the polymer solidifies during cooling, drying of the microporous structure, and modifying pore shapes in a simplified geometry by uni-axial elongation are examined. The change in performance due to a change in pore shape is examined through numerical methods.

1.2 MEMBRANE APPLICATIONS

Several applications can benefit from increased knowledge and control over the evolution of the membrane microstructure. Fields of particular impact are those that require a narrow pore size distribution. Battery separators are known to need a tightly controlled morphology of small pores in order to have a rapid "shut off" capability during a short circuit [19-21]. This "shut off" capability originates from the polymer matrix melting during the rapid temperature rise during a short circuit and flowing to close the small pores of the separator. While many current battery separators are made by the Celgard process [22], the porosity is limited to less than 50% which limits capacity. Formation of battery separators through a TIPS process has the potential to increase the porosity and the resulting capacity of the battery and has been the focus of recent patent literature [23-25].

Another potential field to benefit from control over membrane microstructure is membrane distillation. While not a currently a large commercial opportunity, membrane distillation (MD) has the potential to complement reverse osmosis (RO) desalination processes [26]. In MD, a hydrophobic material is used with small pores. A hot salt solution flows on one side of the membrane, and typically, a cold salt-free solution on the other. The difference in partial pressures drives the process, which is capable of functioning at higher salt loadings than conventional RO membranes [27]. Small pores with a tight distribution are required so that the hot salt solution does not wet the membrane under pressure, which will cause salt contamination of the cold stream. Additionally, for peak performance, conduction of heat from the hot side to the cold side through the polymer matrix should be minimized [26]. Microporous structures with large porosities would meet the need for minimizing conduction and can be produced through L−L TIPS.

Additionally, the new concept of ZeoTIPS membranes requires control over the cellular structure [28], but not necessarily over the pore size distribution. While applications that require narrow pore size distributions like battery separators and membrane distillation could be improved the most, other traditional particulate microfiltration applications like water purification can derive a benefit from the research detailed herein. By tailoring the morphology of membranes, permeability, rejection, and selectivity, could be optimized for several separations.

1.3 SIGNIFICANCE OF THE WORK

The technological significance of this study is focused on removing some of the uncertainty and art behind membrane formation and modification. This work is the first to provide a quantitative model for understanding matrix solidification in L–L TIPS systems. This work provides additional guidance for extractation/exchange and drying steps of membrane production regardless of the phase separation mechanism. The guidance provided establishes a set of heuristics to follow in order to minimize pore collapse during the drying process.

This work also shows a simple method to predict accurately pore shape change in a simplified track-etch geometry due to uniaxial elongation. To examine the theoretical benefits of uniaxial elongation, a sieve method of microfiltration is modified to calculate numerically the resulting effect on performance curves. This work seeks to provide the membrane science community with tools to relate membrane production conditions to the performance of the membrane by accurately predicting the microporous morphology.

1.4 STRUCTURE OF THE DISSERTATION

The remainder of this dissertation is organized as follows. Chapter 2 discusses the relationship between processing conditions (weight percent polymer, isothermal coarsening temperature, isothermal coarsening time, cooling rate) and the solidified membrane structure. Chapter 3 analyzes the effects of evaporation of a variety of extractants on the morphology of the membrane. Chapter 4 looks at modeling the simplified membrane geometry of track-etch membranes during a modification procedure in which uniaxial elongation is used to change the pore shape from circular to elliptical. Numerical solutions to a modified sieve mechanism of microfiltration are presented in Chapter 5. These modifications account for elliptical pore shapes in dead end microfiltration. The conclusions from each of the chapters are summarized in Chapter 6 along with recommendations to extend the research efforts described in this dissertation. The majority of references are cited in the appropriate subsequent chapters, rather than included in this chapter. The appendices at the end of this dissertation contain a nomenclature section defining the symbols used, a listing of computer code for the various models developed herein, and supplementary data to Chapter 3.

1.5 REFERENCES

1 L.J. Zeman and A.L. Zydney, *Microfiltration and Ultrafiltration*, Marcel Dekker, Inc., New York, 1996.

2 K.K. Sirkar and W.S. Ho, *Membrane Handbook*, 1st ed, van Nostrand Reinhold, New York, 1992.

3 M.B. Douglas, D.N. Gray, B. Watson, and C.S. Youngen, *Poly(sulfone-alpha-olefin) composite permselective membrane article for use in blood oxygenation*, US Patent 5,391,580, 1995.

4 T. Masuoka, O. Hirasa, M. Onishi, and Y. Seita, *Porous hydrophilic polypropylene membrane, method for production thereof, and blood plasma separation apparatus*, US Patent 5,186,835, 1993.

5 A.R. Zembrodt, *Air freshener with microporous membrane*, US Patent 4,948,047, 1990.

6 K.S. McGuire, *Membrane formation via liquid-liquid thermally induced phase separation*, Dissertation, The University of Texas at Austin, 1995.

7 A.J. Castro, *Method for making microporous products*, US Patent 4,247,498, 1980.

8 W.C. Hiatt, G.H. Vitzthum, K.B. Wagener, K. Gerlach, and C. Josefiak, *Microporous membranes via upper critical temperature phase separation*, in: D.R. Lloyd (Ed.), Materials Science of Synthetic Membranes, ACS Symposium Series, #269, ACS Press, Washington, DC, 1985, pp. 229-244.

9 G.T. Caneba and D.S. Soong, *Polymer membrane formation through the thermal-inversion process. 1. Experimental study of membrane structure formation*, Macromolecules, 18 (1985) 2538-2545.

10 D.R. Lloyd, K.E. Kinzer, and H.S. Tseng, *Microporous membrane formation via thermally-induced phase separation. I. Solid-liquid phase separation*, Journal of Membrane Science, 52 (1990) 239-261.

11 D.R. Lloyd, S.S. Kim, and K.E. Kinzer, *Microporous membrane formation via thermally-induced phase separation. II. Liquid-liquid phase separation*, Journal of Membrane Science, 64 (1991) 1-11.

12 S.S. Kim and D.R. Lloyd, *Microporous membrane formation via thermally-induced phase separation. III. Effect of thermodynamic interactions on the structure of isotactic polypropylene membranes*, Journal of Membrane Science, 64 (1991) 13-29.

13 G.H. Shipman, *Microporous sheet material method of making and articles made therewith*, US Patent 4,539,256, 1985.

14 K.E. Kinzer, *Oriented microporous films*, US Patent 4,867,881, 1989.

15 S.B. McCray, D.T. Friesen, D.R. Sidwell, D.K. Lyon, and D. Sakashita, *Ethylene-vinyl alcohol hollow fiber membranes*, USA Patent 6,793,820, 2001.

16 M. Chandler and A. Zydney, *Effects of membrane pore geometry on fouling behavior during yeast cell microfiltration*, Journal of Membrane Science, 285 (2006) 334-342.

17 L.S. Worrel, L.A. Shimko, J.A. Morehouse, D. R. Lloyd, B.D. Freeman, and D.F. Lawler, *Enhancement of Track-etched Membrane Performance via Stretching*, Separation and Purifications Technology, 53 (2007) 71-80.

18 J. Morehouse, *The effect of uni-axial stretching on microporous phase-separation membrane structure and performance*, Dissertation, University of Texas at Austin, 2006.

19 K.M. Abraham, *Directions in secondary lithium battery research and development*, Electrochimica Acta, 38 (1993) 1233-1248.

20 S. Atlung, K. West, and T. Jacobsen, *Dynamic aspects of solid solution cathodes for electrochemical power sources*, J. of Electrocheical Science and Technology, 126 (1979) 1311-1321.

21 F.C. Laman, M.A. Gee, and J. Denovan, *Impedance studies for separators in rechargeable lithium batters*, J. of Electrochm. Soc., 140 (1993) L51-L53.

22 R.B. Isaacson and H.S. Bierenbaum, *Process for preparing microporous film*, US Patent 3,558,764, 1971.

23 K. Takita, K. Kono, T. Takashima, and K. Okamoto, *Microporous polyolefin membrane and method of producing same*, US Patent 5,051,183, 1991.

24 T. Hasegawa and T. Kondo, *Polyethylene microporous film and process for producing the same*, US Patent 6,127,438, 2000.

25 T. Hasegawa and T. Kondo, *Microporous polyethylene membranes having low fusing temperatures*, US Patent 6,168,858, 2001.

26 K.W. Lawson and D.R. Lloyd, *Membrane distillation*, Journal of Membrane Science, 124 (1997) 1-25.

27 K.W. Lawson and D.R. Lloyd, *Membrane distillation. II. Direct contact MD*, Journal of Membrane Science, 120 (1996) 123-133.

28 C.V. Funk and D.R. Lloyd, *Zeolite-filled microporous mixed matrix (ZeoTIPS) membranes: Prediction of gas separation performance.*, Journal of Membrane Science, 313 (2008) 224-231.

Chapter 2: Matrix Solidification in L – L TIPS [1]

2.1 INTRODUCTION

Cellular microporous membranes are typically made through either non-solvent induced phase separation/phase inversion or through the thermally induced phase separation (TIPS) process [1-3]. The TIPS process begins by heating a polymer and a diluent to a sufficiently high temperature to melt-blend the components into a homogenous phase. The diluent is a low molecular weight, high-boiling point chemical that is not a solvent for the polymer at room temperature, but acts as one at higher temperatures. When the homogenous blend is cooled, it undergoes phase separation. Through the appropriate choice of diluent and initial polymer concentration [4-6], the solution undergoes liquid–liquid (L–L) TIPS to form diluent-rich and polymer-rich liquid phases. Under most L–L TIPS membrane preparation conditions, the diluent-rich phase forms droplets in a liquid polymer-rich matrix phase. With the passage of time, the diluent-rich droplets grow through a process known as *coarsening*. While most industrial membrane formation processes pass through the L–L region in a non-isothermal manner, many researchers have focused on the simplified case of isothermal coarsening in order to understand the droplet growth mechanism [7-11]. At the end of the isothermal coarsening period used in these studies, the sample is further cooled to terminate the growth by solidifying the polymer-rich matrix phase. The research reported here addresses the post-coarsening stages.

---

[1] The content of this chapter has been published as "Deterministic model for matrix solidification in Liquid – Liquid Thermally Induced Phase Separation," *Journal of Membrane Science*, 306 (2007) 125-133.

During the post-coarsening cooling through the liquid–liquid region, the polymer-rich liquid matrix phase expels diluent causing the droplets to continue growing. Upon reaching the crystallization temperature, the matrix solidifies to establish the nascent morphology of the membrane. Following the solidification of the matrix phase, the diluent is extracted and the extractant is evaporated to yield a cellular microporous structure as seen in Figure 2.1. In Figure 2.1, the pores connecting cells are clearly shown, as is the fact that there is a distribution of cell sizes.

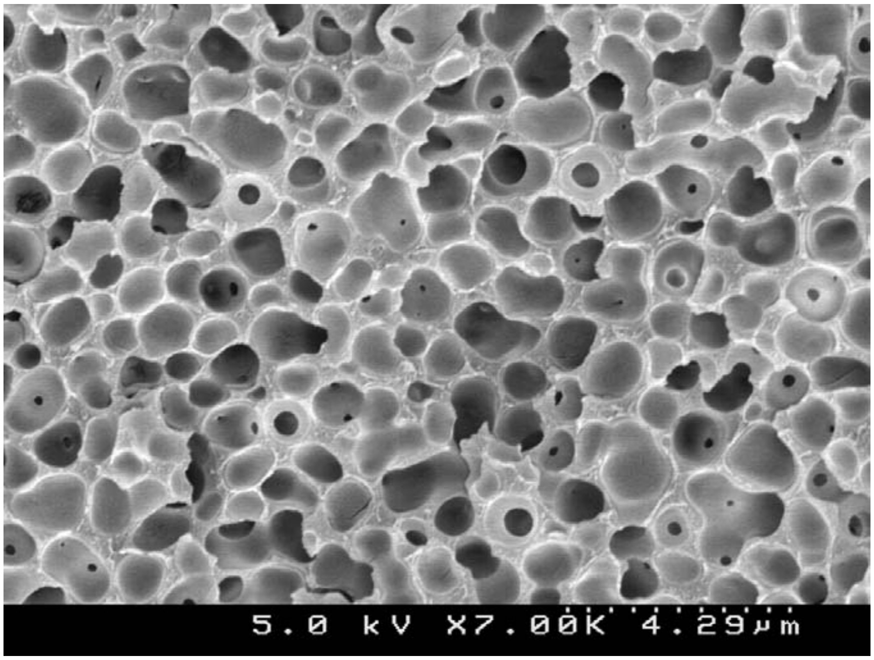

Figure 2.1: The cellular morphology of roughly spherical cells connected by circular pores is typical of L–L TIPS.

For the purposes of the research reported here, one advantage of the TIPS method of structure formation is that heat transfer is rapid; therefore, the cellular structure resulting from the droplet growth is rapidly locked in upon quenching the sample. Many of the reported fundamental studies on TIPS have focused on the mechanism and rate of droplet growth [7-34]. Unfortunately, few studies have investigated the stages in the TIPS process in which the matrix phase solidifies, and the subsequent steps of diluent extraction and material drying. A notable exception is the work of Li *et al.* [35] who have extended work of Avrami [36-38] and Caneba and Soong [39] in modeling the growth of spherelites in solid–liquid (S–L) TIPS. The *objective* of the research reported here is to model the effects of matrix phase solidification, diluent–extractant exchange, and extractant drying on the cell size and cell size distribution of membranes formed via L–L TIPS. This research is the first to take into account the compositional change of the matrix phase during non-isothermal quenching of an L–L TIPS system that has gone through droplet coarsening. This chapter examines the solidification process by taking the into account conditions at the end of the isothermal coarsening period, cooling-rate, solution composition, and the compositional change of the matrix phase during isothermal quenching, in order to establish their connection to the solidified cellular microstructure.

2.1 MODEL DEVELOPMENT

2.2.1 Physical Steps occurring during L – L TIPS

Figure 2.2 shows the phase diagram for isotactic polypropylene (iPP) – diphenyl ether (DPE). When conducting coarsening studies, a homogenous solution in the one-phase region (above the binodal curve) is cooled to a point under the binodal curve (for example, point A), where phase separation occurs. At point A, the composition of the two phases is easily computed. The polymer-lean liquid phase is taken to be 100% DPE (point B), and the polymer-rich liquid phase has the composition of point C. The volume fraction, ϕ, of polymer-lean phase is computed with the lever rule:

$$\phi = \frac{\overline{AC}}{\left(\overline{AC} + \overline{AB}\right)} \tag{2.1}$$

The volume fraction of the polymer-rich phase is simply $1-\phi$. In the isothermal studies mentioned above, point A is maintained for a length of time to allow isothermal growth of the polymer-lean droplets via traditional *coarsening* mechanisms and coalescence-induced-coalescence. Subsequent q*uenching* or cooling from point A causes diluent to be expelled from the polymer-rich matrix, which translates on the phase diagram to point C moving down and to the right along the binodal curve. This non-isothermal diluent expulsion continues until the dynamic crystallization curve (represented by ▲ in Figure 2.2) is reached. At this point crystallization of the polymer and solidification of the polymer-rich matrix phase begins. The crystallization and solidification of the polymer-rich matrix establishes the structure of the nascent membrane. The structure may then be further manipulated through a drying process, compression, or elongation, but those effects are not within the scope of the research presented here. Instead, this chapter focuses on droplet growth during the non-isothermal quench period that follows the isothermal droplet coarsening described above. The model then continues through the crystallization and solidification of the matrix phase.

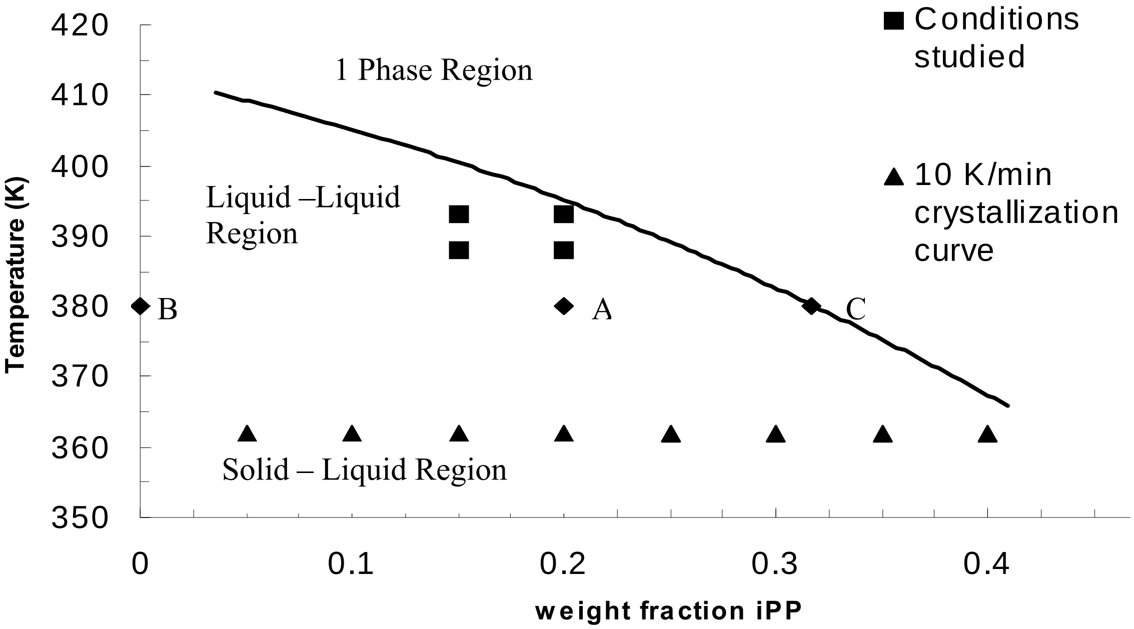

Figure 2.2: iPP – DPE phase diagram.

2.2.2 Modeling Procedure

The model reported here is intended to be used in sequence with knowledge gained through kinetic experiments or modeling of isothermal L–L TIPS droplet coarsening. As such, it does not model nucleation and growth, spinodal decomposition, or any initial coarsening mechanisms. Instead, the model accepts information on the polymer-lean dispersed droplets from previous studies [12, 40, 41]. While the model currently accepts information from studies based upon coalescence-induced-coalescence because that is the dominant mechanism for isothermal coarsening of iPP–DPE, the model is not limited to only that coarsening mechanism or polymer–diluent system provided the necessary physical data are available.

To commence the modeling process, a box of a specified size is created and approximately 75 polymer-lean droplets are randomly placed in the box in such a way that they do not overlap. The size and size distribution of the droplets is determined from experimental data [41] for a specified polymer–diluent composition, coarsening temperature, and length of isothermal coarsening time. Alternatively, if size data are available from a simulation, that data could be used as input. In the current study, the experimental size distribution of the approximately 75 polymer-lean droplets is input as a Gaussian distribution. Table 2.1 contains the information pertaining to the conditions studied in this research and the corresponding droplet size characteristics [41]. The box has periodic boundary conditions and is created large enough so that it is representative of the bulk nascent membrane. The size of the box is dependent upon the size of the polymer-lean droplets and the volume fraction of the diluent at the specified starting temperature. For example, for a 20 wt-% iPP solution coarsened at 393 K, Figure 2.2 and Table 2.1 indicate $\phi = 0.32$ and for 60 seconds of coarsening average droplet diameter is 4.005 μm. For this case the box has dimensions of 40 x 40 x 40 μm. The model computes a series of material balances for this representative periodic box. As explained in the following paragraphs, these balances account for: movement of diluent and further merging events occurring during the quench to the crystallization curve; shrinkage due to cooling beyond the crystallization temperature; and swelling of the solidified polymer.

Table 2.1: Initial starting conditions for solidification of iPP–DPE. The initial volume fraction of diluent is determined from the phase diagram and the size information from previous studies [41].

Composition of Sample	15 wt-% iPP						20 wt-% iPP					
Coarsening Temperature	120°C			115°C			120°C			115°C		
Minutes at coarsening temperature	1	2	3	1	2	3	1	2	3	1	2	3
Initial volume fraction of diluent	0.10	0.10	0.10	0.23	0.23	0.23	0.32	0.32	0.32	0.42	0.42	0.42
Average Droplet diameter (μm)	4.589	5.521	6.382	5.66	7.08	8.12	4.005	5.089	5.603	5.551	6.434	7.29
Droplet standard deviation (μm)	0.74	0.78	1.01	1.13	1.37	1.578	0.507	0.589	0.682	0.872	1.098	1.27

During the quench to the crystallization curve, the diluent is assumed to be expelled in a random direction from the polymer-rich matrix phase into the polymer-lean droplets. Since the diluent is assumed to move in a random direction, it follows that diluent will statistically be incorporated into the nearest polymer-lean droplet. A Monte-Carlo method is used to determine a *volume of influence* for each polymer-lean droplet; that is, the surrounding polymer-rich volume that is closest to that droplet. This Monte-Carlo method chooses a random point within the periodic box approximately 25,000 times, checks to ensure that each random point is outside of any polymer-lean droplets, computes the distance of each random point to all of the polymer-lean droplets, determines the closest polymer-lean droplet for each random point, and determines a ratio of the number of random points closest to each polymer-lean droplet divided by the total number of random points. As the sample is quenched and diluent is expelled from the polymer-rich matrix, each polymer-lean droplet incorporates the expelled diluent from the associated volume of influence. As explained above, the amount of diluent expelled from the polymer-rich phase is computed by utilizing the lever rule, the phase diagram, and established swelling theory that is detailed below. The top half of Figure 2.3 shows a simplified situation in which two droplets incorporate expelled diluent from their respective volumes of influence; the boundary between the droplets' volumes of influence is marked by the dashed line.

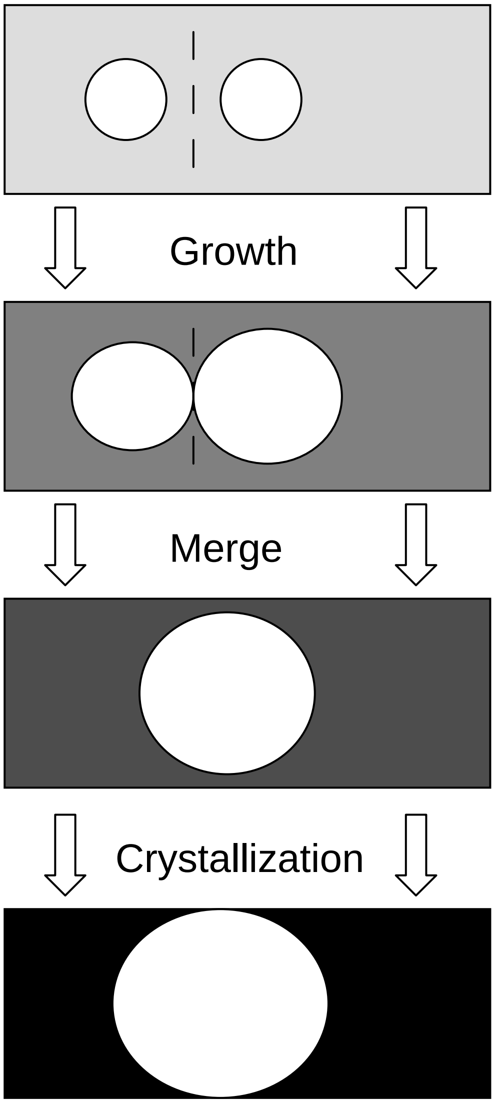

Figure 2.3: Simplified schematic of the steps included in the simulation. A volume of influence is determined (marked by the dashed line) that determines how the polymer-lean droplets will grow. If the droplets touch, the droplets will merge. Finally the simulation accounts for crystallization of the polymer-rich matrix. The shading represents the increasing polymer concentration in the polymer-rich matrix.

An order of magnitude analysis of the distance a diluent molecule can travel through the polymer-rich liquid phase in order to reach a polymer-lean droplet is possible. Matsuyama *et al.* [42] estimated the diffusion coefficient in iPP–DPE using free volume theory developed by Vrentas and Duda [43-46]. Batarseh [47] used the same method with more accurate parameters, given in Table 2.2, for Equations 2.2 and 2.3.

$$D = D_d^*(1-\phi_d)^2(1-2\chi\phi_d) \tag{2.2}$$

$$D_d^* = D_{od} \exp\left[\frac{-\left(\omega_d V_d^* + \omega_p \xi V_p^*\right)}{\omega_d \frac{K_{1d}}{\gamma}\left(K_{2d} - T_{gd} + T\right) + \omega_p \frac{K_{1p}}{\gamma}\left(K_{2p} - T_{gp} + T\right)}\right] \tag{2.3}$$

D_{od} is the pre-exponential factor, D_d^* is the diluent self diffusion coefficient, the subscripts d and p refer to the diluent and polymer, respectfully, K symbols represent free volume, T is temperature, T_g is the glass transition temperature, V^* is the specific critical hole free volume, ξ is the ratio of the critical molar volumes of the diluent and polymer, χ is the interaction parameter, and ω is the weight fraction.

Equation 2.2 predicts the diffusion coefficients for a 20 wt-% iPP solution vary from 1.0 x 10^{-11} m^2/s to 4.9 x 10^{-12} m^2/s over the liquid–liquid portion of the phase diagram. Performing an order of magnitude analysis with $D_{iPP-DPE}$ $O(10^{-12})$ yields a root mean square displacement of a diluent molecule to be 5.5 μm. The largest droplet to droplet distance studied in this research (for the case of 20 wt-% iPP, diluent volume fraction = 0.10, and 3 minutes of isothermal coarsening) is 6.6 μm. A diluent molecule would only need to travel 3.3 μm to find a polymer-lean droplet. As the order of magnitude analysis predicts a molecule will be able to travel 5.5 μm, it is reasonable to expect the diffusion of diluent molecules can be accurately simulated by the described Monte Carlo method.

Table 2.2: Parameters used to calculate the diffusion coefficient of DPE in an iPP–DPE liquid matrix [55].

Parameter	Value
D_{od} [cm^2/s]	2.36 x 10^{-4}
V_d* [cm^3/g]	0.795
V_p* [cm^3/g]	1.034
ξ	1.18
K_{ld}/γ [cm^3/g-K]	8.34 x 10^{-4}
$K_{2d} - T_{gd}$ [K]	–142.0
K_{lp}/γ [cm^3/g-K]	4.99 x 10^{-4}
K_{2p} [K]	227.6
T_{gp} [K]	257.0

As the polymer-lean droplets grow via this *expulsion* mechanism, they continue to merge until arrested by the solidification of the polymer-rich matrix phase. In the simulation presented here, traditional mechanisms used to describe isothermal coalescence [15-42] are ignored because, as demonstrated below, the growth rate of the polymer-lean droplets is dominated by the expulsion of diluent and the resulting droplet merges. It has been observed during coarsening and quenching experiments that simultaneous coalescence of any given droplet with two neighbors is rare; consequently, a model of the merging of droplets during the quenching process is restricted to the merging of a droplet with only one neighbor at a time. To simplify the modeling, the polymer-lean droplets can only merge when they come into contact, as represented by Figure 2.3, and are prohibited from further merging until sufficient time has passed for the two droplets to finish merging. The time required for two droplets to merge is given in the literature by:

$$t_r = \frac{a_o \sigma}{\gamma} \tag{2.4}$$

where t_r is the relaxation time required to complete coalescence, a_o is the average radius of the two droplets that are merging, σ is the temperature-dependent apparent viscosity of the bulk suspension, and γ is the temperature-dependent surface tension between the polymer-rich and polymer-lean phases. However, using the experimental values of Martula *et al.*, Equation 2.4 calculates that the time for two droplets to coalesce is on the order of 0.3 seconds. This is an order of magnitude smaller than what is observed experimentally at the coarsening conditions. Thus, Equation 2.4 was modified as follows:

$$t_r = \frac{(a_o / a_{\exp})*(\sigma / \sigma_{\exp})}{(\gamma / \gamma_{\exp})}(t_{r\_\exp}) \qquad (2.5)$$

where the subscript *exp* designates experimental values. Values of $a_{\exp}$, $\sigma_{\exp}$, $\gamma_{\exp}$ and $t_{r\_\exp}$ for use in Equation 2.5 were obtained from rheology and isothermal coarsening experiments [48]. Values of σ and γ were obtained as described in the following two paragraphs using the temperature at the time when the merge commences, and a_o is calculated from the size of the two merging droplets.

The value of γ to be used in Equation 2.5 was obtained from Martula *et al.* [48] who demonstrated that experimental observations varied as suggested by [49-51]:

$$\gamma \propto M_w^{(1-\kappa)}\left(\frac{T_c - T}{T_c}\right)^{\mu} \qquad (2.6)$$

where M_w is the molecular weight of the polymer, T_c is the critical temperature of the system, T is the temperature, and κ and μ are experimentally determined constants with values of 0.86 and 1.13, respectively for the iPP used in this study.

The value of σ to be used in Equation 2.5 was again obtained from Martula *et al.* [48] who observed that while the iPP–DPE suspension is non-Newtonian, the Reynolds number for the system is of the order *O(–9)*, so the non-Newtonian behavior can be reduced to Newtonian mechanics. Thus, the experimental viscosities of Martula *et al.* can be extrapolated without introducing significant error. Additionally, viscosity exhibits such a slight dependency on the size of the polymer-lean droplets that it can be safely neglected for this system [52]. Figure 2.4 demonstrates the viscosity dependence on temperature.

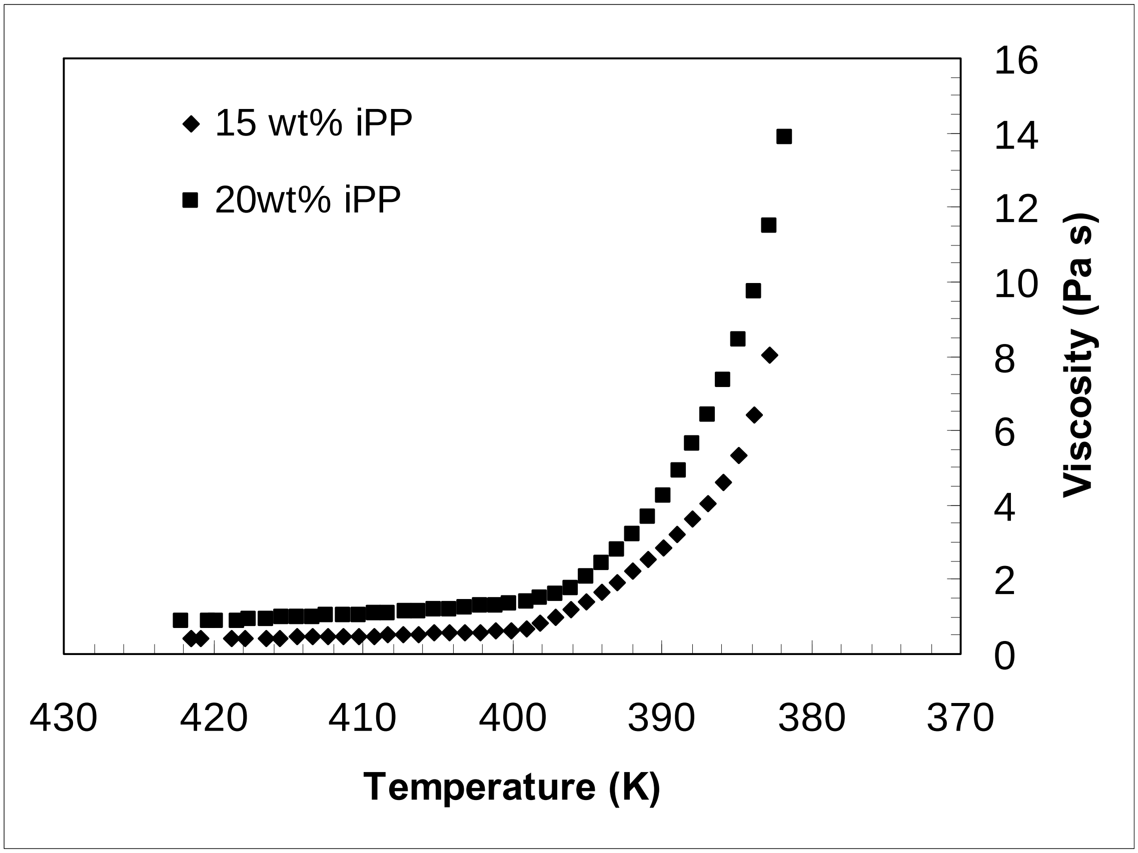

Figure 2.4: Viscosity (Pa*s) of iPP – DPE system as a function of temperature.

For example, according to Equation 2.5, two polymer-lean droplets with diameters of 3.5 and 4.5 micrometers in a 20 wt-% iPP mixture at 380 K will take approximately 8.6 seconds to finish merging given a_o = 4.0 μm, γ = 0.2253 dyne/cm, σ = 13.9 Pa·s, and the experimental values from isothermal coalescence experiments at 393 K for a_{exp}, γ_{exp}, σ_{exp} and t_{r_exp} are 3.0 μm, 0.098 dyne/cm, 2.8 Pa·s, and 3 seconds, respectively. This calculated value for t_r is comparable to observations made under a microscope of quenching experiments.

During the quench period, the growth of polymer-lean droplets by the expulsion of diluent by the polymer-rich matrix is calculated for every one Kelvin degree. After the diluent has been incorporated into the polymer-lean droplets, all of the droplets are compared to their neighbors to see if a merging opportunity exists. If so, the two droplets are allowed to merge, but are ineligible to merge with other droplets until the merge is complete, as calculated by Equation 2.5. The position of the merged droplet is the center of mass of the two merging droplets. The above procedure is repeated until the temperature of the system reaches to dynamic crystallization curve. The number, position, volume fraction, size, and size distribution of droplets at the time when crystallization starts is then used in the crystallization and solidification calculations described in the following paragraphs.

Merging of droplets is prohibited once the temperature has dropped to the crystallization curve because of the rapid and dramatic increase in the viscosity accompanying the solidification of the polymer-rich matrix. The diluent present in the polymer-rich matrix phase at the time of solidification is expelled to the droplets so that the droplets can grow and overlap, but not complete a merge due to the few seconds available compared to the more than 20 seconds required for the merge to finish. The amount of diluent in the matrix phase at the time of solidification is computed from swelling theory and the phase diagram as described in the following paragraphs. The crystallization is represented by the final box in Figure 2.3.

Determining the amount of diluent remaining in the solidified polymer is calculated using the Flory–Rehner Equation [53]:

$$\ln(1-\phi_2)+\phi_2+\chi\phi_2{}^2+\tilde{V}_1 n(\phi_2{}^{1/3}-\frac{\phi_2}{2})=0 \qquad (2.7)$$

The volume fraction of the polymer, ϕ_2, is affected by the Flory–Huggins interaction parameter, χ, the molar volume of the diluent, $\tilde{V}_1$, and the crosslink density, n. Since diluents in the L–L TIPS process are typically chosen to have little or no affinity for the polymer at room temperature, the amount of swelling in the solidified polymer is negligible. This has been experimentally demonstrated by immersing an iPP film in DPE for 6 months and determining that no measurable swelling occurred.

The periodic box is reduced in size to account for the densification of the polymer-rich matrix. Additive volumes are assumed, and the corresponding change in density with temperature is used to generate a shrinkage factor of ρ_{L-L} / ρ_{S-L} using the arithmetic averages as shown in equations 2.8 and 2.9:

$$\rho_{L-L} = \phi_{drop}\rho_{diluent} + (1-\phi_{drop})(x_{mp}\rho_{molten} + (1-x_{mp})\rho_{diluent}) \tag{2.8}$$

$$\rho_{S-L} = \phi_{drop}\rho_{diluent} + (1-\phi_{drop})(x_{mp}(w_{cryst}\rho_{cryst} + (1-w_{cryst})\rho_{amorph}) + (1-x_{mp})\rho_{diluent}) \tag{2.9}$$

where, ρ is the system density, ϕ_{drop} is the volume fraction of diluent droplets, x_{mp} is the fraction of the polymer-rich matrix phase that is polymer, w_{cryst} is the fraction of the polymer that is crystalline, and ρ with a subscript denotes the density of an individual component. Values of the molten, crystalline, and amorphous phase densities of the polymer matrix are available in literature [54] and a crystallinity for the final sample is assumed. Since iPP has been shown to achieve a crystallinity of 31% with a direct quench into water [54], this value was used in the model. The computed shrinkage factor is used to reduce the size of the repeat unit by multiplying the edge-lengths and the coordinates of the droplets with the shrinkage factor. For example, using Equations 2.8 and 2.9 to calculate the shrinkage factor of ρ_{L-L} / ρ_{S-L} of a 20 wt-% iPP solution with an initial volume fraction of diluent of 0.32 will have a volume shrinkage factor of 0.9748, which by taking the cube root, results in an edge shrinkage factor of 0.9915.

The last portion of the model uses a Monte-Carlo method that determines the volume fraction of the polymer-lean droplet phase. Random points are selected within the periodic box and evaluated to determine if the points are inside drops. The ratio of random points within drops to the total number of random points selected, found to be approximately 15,000 points, is the polymer-lean droplet fraction. If this fraction is below 99% of the theoretical volume fraction due to overlapping droplets, a multiplier is used to increase all of the diameters uniformly until the 99% of the theoretical volume fraction is met. This multiplier is needed to account for the overlaps between cells and is often small, approximately 1.06. A time lapse graphical rendition of the polymer-lean droplet growth and resulting polymer-rich solidified matrix is shown in Figure 2.5.

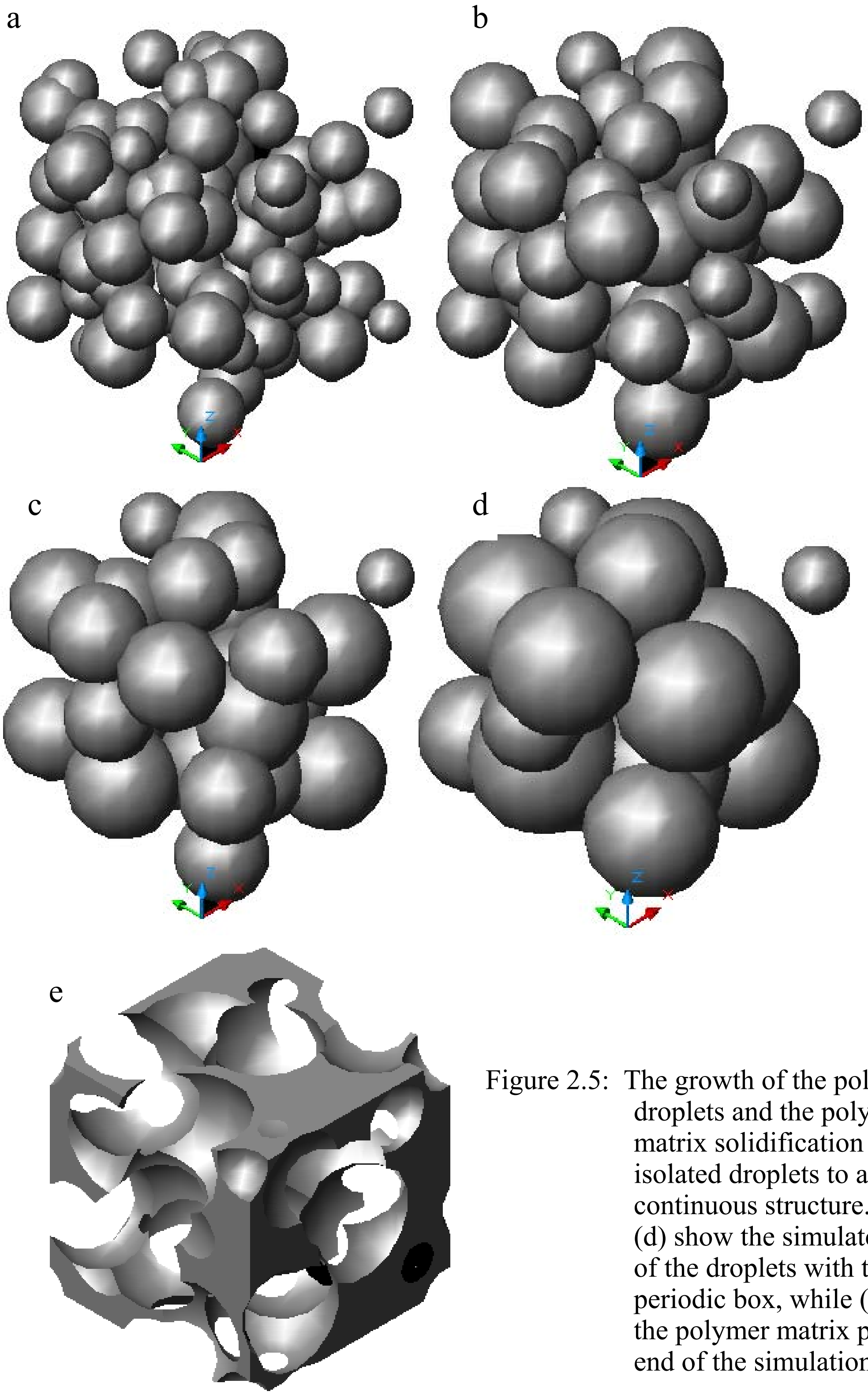

Figure 2.5: The growth of the polymer-lean droplets and the polymer-rich matrix solidification lead from isolated droplets to a co-continuous structure. (a) through (d) show the simulated growth of the droplets with time in the periodic box, while (e) shows the polymer matrix phase at the end of the simulation.

2.2 MATERIALS AND METHODS

2.2.1 Materials

The polymer–diluent system selected for this study is isotactic polypropylene–diphenyl ether (iPP–DPE). The iPP was obtained from Exxon Chemical and has a reported M_w of 138,000 grams/mole; the polydispersity index is not reported. DPE was obtained from Aldrich at 99% purity. Both the iPP and DPE were used as received from the manufacturers without further purification. This system was selected because: it forms well defined cellular morphologies; it has a large miscibility gap [55] allowing for several different quench conditions; the difference between refractive indices of the polymer-rich matrix and polymer-lean droplets allow for easy viewing [56]; the condition of the polymer-rich liquid matrix and polymer-lean droplets at various stages of the coarsening process are known [7, 48, 57]; and it undergoes rapid crystallization to terminate droplet growth upon quenching [58-60].

2.2.2 Experimental Procedure

iPP–DPE samples were prepared as previously reported [6, 41] by heat sealing appropriate amounts of polymer and diluent in a test tube after purging with nitrogen for one minute. These samples were heated at 180°C for 48 hours to ensure homogeneity. The samples were then frozen in liquid nitrogen, broken open, and slices from the frozen sample were placed between two glass coverslips of dimensions 22 x 22 x 0.17 mm. The glass coverslips were separated by a 0.13 mm Teflon spacer. The edges were coated with vacuum grease to prevent diluent evaporation. The samples were heated on a Linkham TMS 91 hotstage to 180°C for ten minutes, which has been shown to eliminate thermal history [5], cooled at 120°C/min to either 115°C or 120°C, held for 1, 2, or 3 minutes to allow for coarsening, and then cooled at 120°C/min to room temperature to induce solidification.

After solidification, the membranes were to be extracted, dried, and analyzed in such a way that the final dry membrane represented the membrane structure at the end of the solidification; in other words, to minimize the effects of post-solidification processing. To achieve this goal, the membranes were first extracted in isopropyl alcohol for at least four hours. The IPA was then exchanged by soaking the membrane in pentane for at least four hours. The membranes were dried at room temperature without restraint. Pentane, with its low surface tension of 15.5 mN/m, was selected as the final liquid extractant in order to minimize the shrinkage during drying. By comparison of the film size after solidification, after extraction with IPA, after exchange with pentane and after drying, it was concluded that no significant shrinkage occurred during extraction and drying. After drying, the membranes were freeze-fractured in liquid nitrogen and sputter coated with gold before being imaged in a Hitachi S-4500 SEM. The images were analyzed with ImagePro software (www.imagepro.com) to measure cell size and cell size distribution.

2.3 RESULTS AND DISCUSSION

Membranes produced as outlined above were analyzed to obtain information on cell size and cell size distribution. When the membranes are freeze-fractured, the membranes do not break in a manner such that all cells break at their widest point. Therefore, in order to compare directly simulation results and experimental results, a correction factor was used to account for cells not breaking at their widest diameter. This factor was obtained by computing

$$D_{obs} = \frac{\int_0^{0.9R} 2 * \sqrt{R^2 - h^2}\, dh}{0.9R} \approx 0.88 D_{true} \tag{2.10}$$

where D_{obs} is the observable average diameter, D_{true} is the real diameter of the cell, R is the radius of a sphere, h is the distance from the center of the cell to the plane on which the cell is fractured. The integrand is the Pythagorean Theorem for a triangle created by the radius, h, and the observed diameter at the break point. The limit of zero corresponds to a break across the widest cell diameter, and the upper limit of 0.9R roughly corresponding to the smallest acceptable measurement of a cell diameter. The experimentally observed cell diameters are divided by this factor to obtain what will be reported as the experimental diameters.

Figure 2.6 shows the comparison between experimental and computed cell diameters for the four initial volume fractions of the polymer-lean phase (see Table 2.1 and Figure 2.2 for the experimental conditions). Within each plot, droplet size at the end of the coarsening period, simulated cell size, and experimental cell size are plotted versus coarsening time. The error bars represent the standard deviation for the cell size distribution rather than the error associated with the average value. Each data point represents at least three experiments or three simulations. Each simulation used a different data set, but each data set is representative of the initial starting conditions. As evidenced by each of the plots in Figure 2.6, the simulation results are in statistical agreement with the experimentally measured cell size results. However, it is also noted that the model consistently predicts a slightly larger cell diameter than experimentally observed. This is primarily attributed to the effects of blooming, in which diluent is expelled to the surface of the membrane rather than simply collecting in the droplets that become cells. The blooming effect was noticed in the experiments, as the glass coverslips contained a diluent residue. Blooming is also often noticed in extrusion of membranes into a bath, where a layer of diluent will build up on the surface of the bath. Blooming was not included in this simulation as it is dependent upon: geometry; method of production; the polarity of the glass coverslips; the polymer–diluent system; and can vary from individual to individual. Some of the slight difference between the model and the experimental results may also be attributed to the simulation being restricted to only considering spherical cells, while experimentally formed membranes contain cells that are often slightly deformed from the spherical ideal. The limitation of only considering spherical cells in the simulation also results in pores larger than one would expect and limits the functionality of the simulation to only cell size and cell size distribution prediction.

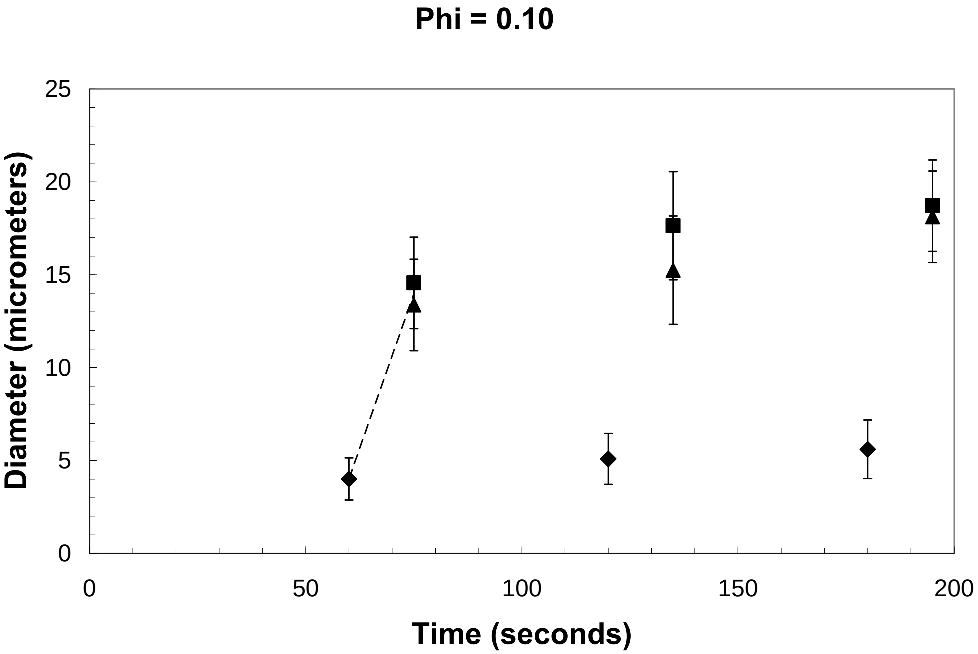
Phi = 0.10
Diameter (micrometers)
0
5
10
15
20
25
Time (seconds)
0
50
100
150
200

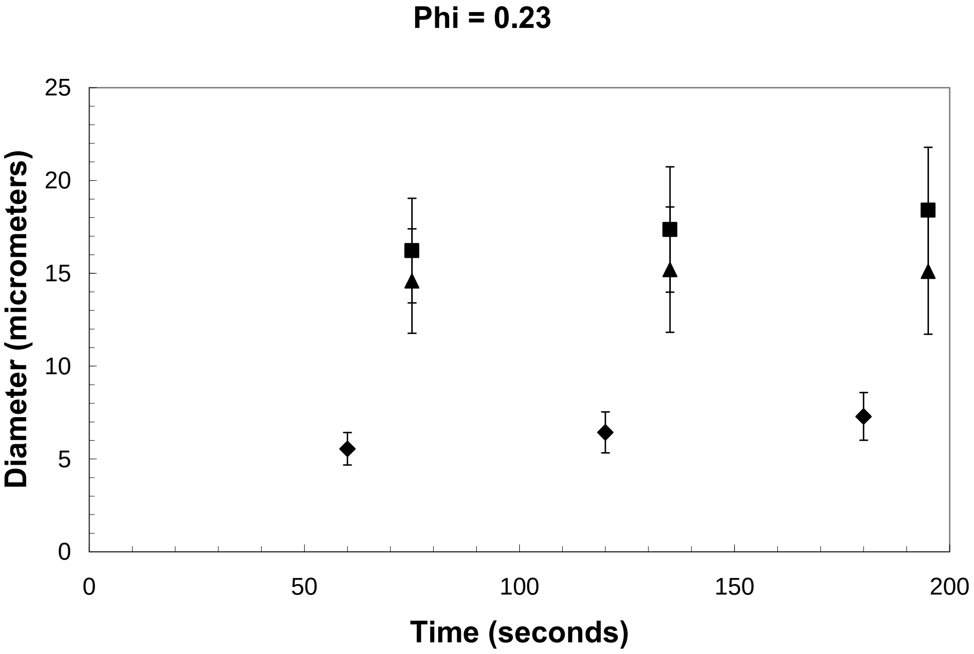
Phi = 0.23
Diameter (micrometers)
0
5
10
15
20
25
Time (seconds)
0
50
100
150
200

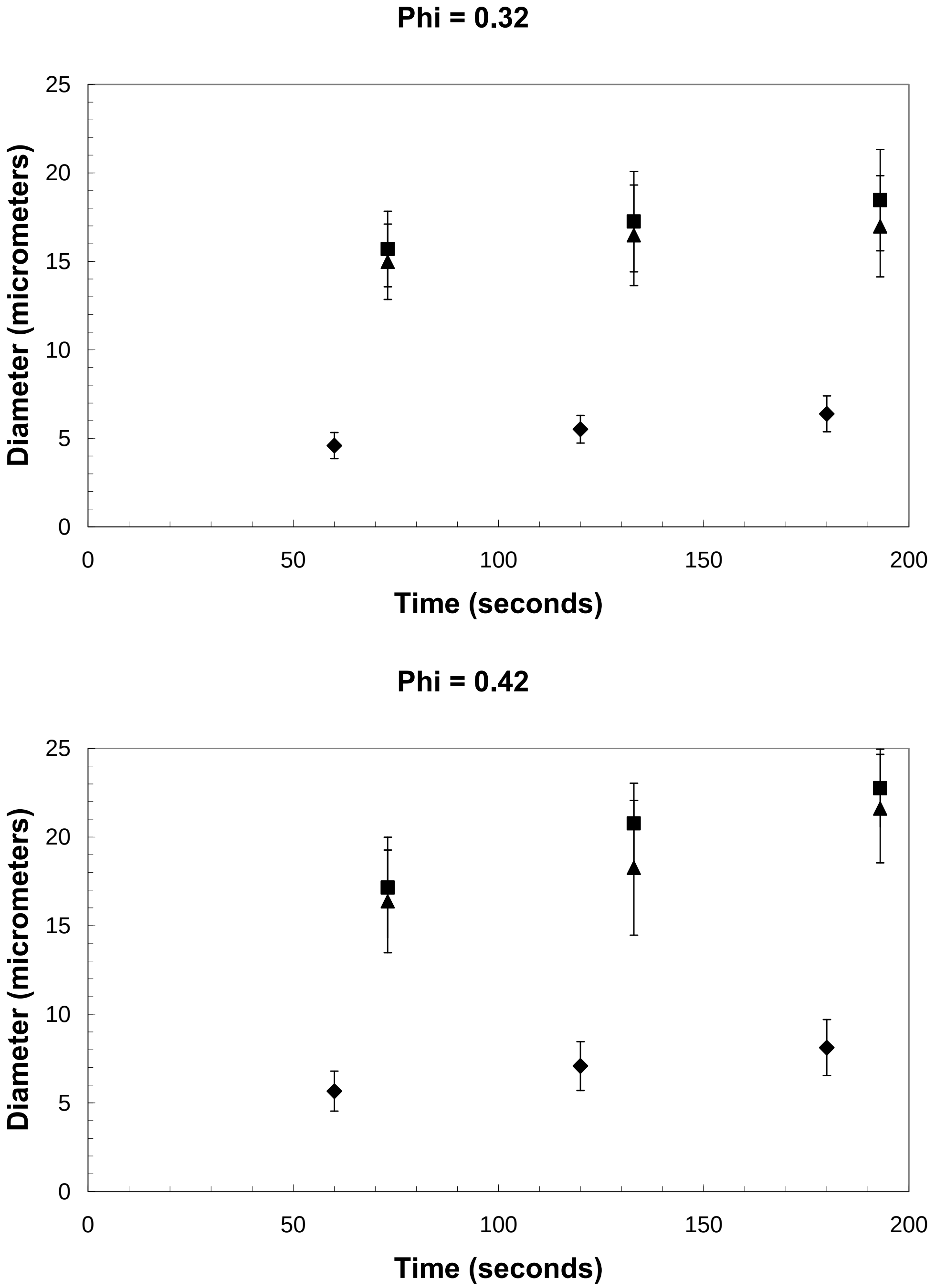

Figure 2.6: Cell diameter as a function of time in the liquid – liquid region for four representative starting polymer-lean volume fractions (Phi). The droplet size at the end of the coarsening period is represented by ♦. The simulated final cell size is represented by ■. The experimental cell size is represented by ▲.

Figure 2.6 also justifies that the simulation does not incorporate modeling of the dominant isothermal coarsening mechanism. Taking the plot for $\phi = 0.10$ (20 wt-% iPP at 393 K) as a typical example, one sees that during the isothermal coarsening period between 60 seconds and 180 seconds the average polymer-lean droplet size grows by 1.6 μm. The dashed line in Figure 6 represents quenching and solidifying the same mixture after 60 seconds of isothermal coarsening. In the approximately 15 seconds of quenching and solidification indicated by the dashed line, the polymer-lean droplets nearly triple in size by growing by 9.36 μm. Thus, droplet growth by expulsion is considered to be the dominant growth mechanism during the non-isothermal quench and matrix solidification.

The modeling program was written and implemented in Matlab 2006 (www.matlab.com). The code developed for the simulation is listed in Appendix A and is available. It takes between 15-25 minutes for a periodic box to run using a dedicated 1.6 GHz processor. The run time can be reduced if the program is coded into a language that can use multiple processors.

2.4 CONCLUSIONS

This simulation is another step in a sequence of programs designed to model the initial formation of polymer-lean droplets, initial coarsening, matrix solidification, diluent extraction/exchange, and drying. The simple deterministic approach for modeling matrix solidification using a series of material balances utilized in this research can provide accurate predictions of final cell size diameter and distribution for isotropic L–L TIPS membranes given information about the polymer-lean phase in the liquid–liquid region. These material balances account for: movement of diluent and further merging events occurring during the quench to the crystallization curve; shrinkage due to densification caused by cooling beyond the crystallization curve; and swelling of the solidified polymer. While requiring significant physical data, the run-time is short enough to be useful and is the first simulation to take into account the compositional change of the matrix phase during non-isothermal quenching of a L–L TIPS system that has gone through droplet coarsening. The simulation also yields information that would allow formation of a membrane with a desired cell size, but with variable porosities resulting from different starting conditions.

2.5 REFERENCES

1 A.J. Castro, *Methods for making microporous products*, US Patent 4,247,498, 1981.

2 W.C. Hiatt, G.H. Vitzthum, K.B. Wagener, K. Gerlach, and C. Josefiak, *Microporous membranes via upper critical temperature phase separation*, in: D.R. Lloyd (Ed.), Materials Science of Synthetic Membranes, ACS Symposium Series, #269, ACS Press, Washington, DC, 1985, pp. 229-244.

3 G.T. Caneba and D.S. Soong, *Polymer membrane formation through the thermal-inversion process. 1. Experimental study of membrane structure formation*, Macromolecules, 18 (1985) 2538-2545.

4 D.R. Lloyd, K.E. Kinzer, and H.S. Tseng, *Microporous membrane formation via thermally-induced phase separation. I. Solid-liquid phase separation*, Journal of Membrane Science, 52 (1990) 239-261.

5 D.R. Lloyd, S.S. Kim, and K.E. Kinzer, *Microporous membrane formation via thermally-induced phase separation. II. Liquid-liquid phase separation*, Journal of Membrane Science, 64 (1991) 1-11.

6 S.S. Kim and D.R. Lloyd, *Microporous membrane formation via thermally-induced phase separation. III. Effect of thermodynamic interactions on the structure of isotactic polypropylene membranes*, Journal of Membrane Science, 64 (1991) 13-29.

7 K.S. McGuire, A. Laxminarayan, and D.R. Lloyd, *Kinetics of droplet growth in liquid-liquid phase separation of polymer-diluent systems: experimental results*, Polymer, 36 (1995) 4951-4960.

8 C.K. Haas and J.M. Torkelson, *2D coarsening in phase-separated polymer solutions: dependence on distance from criticality*, Physical Review Letters, 75 (1995) 3134-3137.

9 P.D. Graham, A.J. Pervan, and A.J. McHugh, *The dynamics of thermal-induced phase separation in PMMA solutions*, Macromolecules, 30 (1997) 1651-1655.

10 E.D. Siggia, *Late stages of spinodal decomposition in binary mixtures*, Physical Review A, 20 (1979) 595-605.

11 Y.C. Chou and W.I. Goldburg, *Angular distribution of light scattered from critically quenched liquid mixtures*, Physical Review A, 23 (1981) 858-864.

12 K.S. McGuire, *Membrane formation via liquid-liquid thermally induced phase separation*, Dissertation, The University of Texas at Austin, 1995.

13 N.-C. Wong and C.M. Knobler, *Light scattering studies of phase separation in isobutyric acid + water mixtures*, Journal of Chemical Physics, 69 (1978) 725-735.

14 T. Hashimoto, J. Kumaki, and H. Kawai, *Time-resolved light scattering studies on kinetics of phase separation and phase dissolution of polymer blends. 1. Kinetics of phase separation of a binary mixture of polystyrene and poly(vinyl methyl ether)*, Macromolecules, 16 (1983) 641-648.

15 L.P. McMaster, *Aspects of liquid-liquid phase transition phenomena in multicomponent polymeric systems*, in: N.A. Platzer (Ed.), Advances in Chemistry Series, 142, Washington, 1975, pp. 43-65.

16 I.G. Voigt-Martin, K.-H. Leister, R. Rosenau, and R. Koningsveld, *Kinetics of phase separation in polymer blends for deep quenches*, Journal of Polymer Science B: Polymer Physics, 24 (1986) 723-751.

17 S. Nojima, K. Tsutsumi, and T. Nose, *Phase separation in polymer systems. II. Microscopic studies on a polystyrene and diisodecyl phthalate mixture*, Polymer Journal, 14 (1982) 289-294.

18 Z.H. Stachurski, G.H. Edward, M. Yin, and Y. Long, *Particle coarsening in polypropylene/polyethylene blends*, Macromolecules, 29 (1996) 2131-2137.

19 U. Sundararaj and C.W. Macosko, *Drop breakup and coalescence in polymer blends: the effects of concentration and compatibilization*, Macromolecules, 28 (1995) 2647-2657.

20 G. Brown and A. Chakrabarti, *Phase separation dynamics in off-critical polymer blends*, Journal of Chemical Physics, 98 (1993) 2451-2458.

21 H. Tanaka, *New coarsening mechanisms for spinodal decomposition having droplet pattern in a binary fluid mixture: collision-induced collision*, Physical Review Letters, 72 (1994) 1702-1705.

22 H. Tanaka, *A new coarsening mechanism of droplet spinodal decomposition*, J. Chem. Phys., 103 (1995) 2361-2368.

23 H. Tanaka, *Coarsening mechanisms of droplet spinodal decomposition in binary fluid mixtures*, J. Chem. Phys., 105 (1996) 10099-10114.

24 H. Tanaka, *Preservation of droplet collision history in phase separation of a binary mixture*, Physical Review E, 54 (1996) R2216-R2219.

25 H. Tanaka, *New mechanisms of droplet coarsening in phase-separating fluid mixtures*, Journal of Chemical Physics, 107 (1997) 3734-3737.

26 W.R. White and P. Wiltzius, *Real space measurement of structure in phase separating binary fluid mixtures*, Physical Review Letters, 75 (1995) 3012-3015.

27 C.K. Haas and J.M. Torkelson, *Two-dimensional coarsening and phase separation in thin polymer solution films*, Physical Review E, 55 (1997) 3191-3201.

28 C.A. Smolders, J.J.v. Aartsen, and A. Steenbergen, *Liquid-liquid phase separation in concentrated solutions of non-crystallizable polymers by spinodal decomposition*, Kolloid-Z. u. Z. Polymere, 243 (1971) 14-20.

29 P.D. Graham and A.J. McHugh, *Kinetics of thermally induced phase separation in a crystallizable polymer solution*, Macromolecules, 31 (1998) 2565-2558.

30 P.D. Graham, B.F. Barton, and A.J. McHugh, *Kinetics of thermally induced phase separation in ternary polymer solutions. II. Comparison of theory and experiments*, Journal of Polymer Science: Part B: Polymer Physics, 37 (1999) 1461-1467.

31 B.F. Barton, P.D. Graham, and A.J. McHugh, *Dynamics of Spinodal Decomposition in Polymer Solutions Near a Glass Transition*, Macromolecules, 31 (1998) 1672-1679.

32 B.F. Barton and A.J. McHugh, *Kinetics of Thermally Induced Phase Separation in Ternary Polymer Solutions. I. Modeling of Phase Separation Dynamics*, Journal of Polymer Science: Part B: Polymer Physics, 37 (1999) 1449-1460.

33 P. Bassereau, D. Brodbeck, T.P. Russell, H.R. Brown, and K.R. Shull, *Topological coarsening of symmetric diblock copolymer films: model 2D systems*, Physical Review Letters, 71 (1993) 1716-1719.

34 J. Lal and R. Bansil, *Light-scattering study of kinetics of spinodal decomposition in a polymer solution*, Macromolecules, 24 (1991) 290-297.

35 D. Li, W.B. Krantz, A.R. Greenburg, and R.L. Sani, *Membrane formation via thermally induced phase separation (TIPS): Model development and validation*, Journal of Membrane Science, 279 (2006) 50-60.

36 M. Avrami, *Kinetics of phase change, I: General theory*, Journal of Chemical Physics, 7 (1939) 1103-1112.

37 M. Avrami, *Kinetics of phase change, II: Transformation-time relations for random distribution of nuclei*, Journal of Chemical Physics, 8 (1940) 212-224.

38 M. Avrami, *Kinetics of phase change, III: Granulation, phase change and microstructure*, Journal of Chemical Physics, 9 (1941) 177-184.

39 G.T. Caneba and D.S. Soong, *Polymer membrane formation through the thermal-inversion process. 2. Mathematical modeling of membrane structure formation*, Macromolecules, 18 (1985) 2545-2555.

40 D.S. Martula, T. Hasegawa, D.R. Lloyd, and R.T. Bonnecaze, *Coalescence-induced coalescence of inviscid droplets in a viscous fluid*, Journal of Colloid and Interface Science, 232 (2000) 241-253.

41 D.S. Martula, *Coalescence-induced coalescence*, Dissertation, The University of Texas at Austin, 2000.

42 H. Matsuyama, S. Berghmans, and D.R. Lloyd, *Formation of anisotropic membranes via thermally induced phase separation*, Polymer, 40 (1999) 2289-2301.

43 J.S. Vrentas and J.L. Duda, *Molecular Diffusion in Polymer Solutions*, AIChE Journal, 25 (1979) 1-24.

44 J.L. Duda, J.S. Vrentas, S.T. Ju, and H.T. Liu, *Prediction of Diffusion Coefficients for Polymer-Solvent Systems*, AIChE Journal, 28 (1982) 279-285.

45 J.M. Zielinski and J.L. Duda, *Predicting Polymer/Solvent Diffusion Coefficients Using Free-Volume Theory*, AIChE Journal, 38 (1992) 405-415.

46 J.S. Vrentas, J.L. Duda, and H.C. Ling, *Self Diffusion in Polymer-Solvent-Solvent Systems*, J. Polym. Sci., Polym. Phys. Ed., 22 (1984) 459-469.

47 M.T. Batarseh, *Formation of anisotropic hollow fiber membranes via TIPS*, Dissertation, The University of Texas at Austin, 1999.

48 D.S. Martula, R.T. Bonnecaze, and D.R. Lloyd, *The effects of viscosity on coalescence-induced coalescence*, International Journal of Multiphase Flow, 29 (2003) 1265-1282.

49 B. Widom, *Phase separation in polymer solutions*, Physica A, 194 (1993) 532-541.

50 A. Vrij, *Equation for the interfacial tension between demixed polymer solutions*, Journal of Polymer Science: Part A-2, 6 (1968) 1919-1932.

51 T. Nose and T. Van Tan, *Interfacial tension of demixed polystyrene-methylcyclohexane solution*, Journal of Polymer Science: Polymer Letters Edition, 14 (1976) 705-712.

52 D. Graebling, R. Muller, and J.F. Palierne, *Linear Viscoelastic Behavior of Some Incompatible Polymer Blends in the Melt. Interpretation of Data with a Model of Emulsion of Viscoelastic Liquids*, Macromolecules, 26 (1993) 320-329.

53 P. Flory and J. Rehner, *Statistical Mechanics of Cross-Linked Polymer Networks, II. Swelling*, Journal of Chemical Physics, 11 (1943) 521-526.

54 J. Brandrup, E.H. Immergut, and E.A. Grulke, (Eds.), Polymer Handbook, 4th ed., John Wiley & Sons, New York, 1999.

55 A. Nakajima and H. Fujiwara, *Phase relationships and thermodynamic interactions in isotactic polypropylene-diluent systems*, Journal of Polymer Science: Part A-2, 6 (1968) 723-733.

56 A. Laxminarayan, *The kinetics of membrane formation via thermally induced liquid-liquid phase separation*, Dissertation, The University of Texas at Austin, 1994.

57 K.S. McGuire, A. Laxminarayan, D.S. Martula, and D.R. Lloyd, *Kinetics of droplet growth in liquid-liquid phase separation of polymer-diluent systems: model development*, Journal of Colloid and Interface Science, 182 (1996) 46-58.

58 G.B.A. Lim, *Effects of nucleating agent on thermally induced phase separation membrane formation*, Dissertation, The University of Texas at Austin, 1990.

59 Y.F. Wang, *Crystallization of isotactic polypropylene and dotriacontane: a study of kinetics and morphology*, Dissertation, The University of Texas at Austin, 1989.

60 A. Alwattari, *Thermally induced phase separation of isotactic polyproylene and hexamethylbenzene*, Dissertation, The University of Texas at Austin, 1990.

Chapter 3: Drying of Microporous Membranes

3.1 INTRODUCTION

Microporous membranes can be formed through a variety of techniques including: track-etching, non-solvent induced phase separation (NIPS), and thermally induced phase separation (TIPS) [1-5]. The drying of membranes formed by NIPS and TIPS can be problematic due to the collapse of the membrane morphology. The collapse can lead to a reduction in porosity and reduced pore/cell size, which in turn lead to a negative impact on permeability, resistance, and fouling behavior of the membranes.

Unfortunately, there have been few in-depth studies to determine the effects of various parameters in the drying process on membrane morphology. Part of this lack of research into the effects of drying is due to industrial avoidance of the issue; they usually simply find extractants that cause minimal shrinkage without understanding the role that the extractants play. Patent literature clearly demonstrates industrial avoidance of the issue [6, 7]. Additionally, much of the attention that has been focused on membranes in the ultrafiltration (UF) [8] and reverse osmosis (RO) regimes [9]. These studies report significant shrinkage in the top/active surface layers, which significantly impacts performance. Unfortunately, many of these studies are hampered by irreproducibility from sample to sample [8]. This may be partially explained by many UF membranes being formed by NIPS and contain macrovoids. If the spatial and size distribution of the macrovoids is not consistent, irreproducibility is to be expected.

Much of the original literature on membrane formation for liquid separation membranes concentrates on the “wet” process developed and matured by Sourirajan [10, 11] and the “dry” process developed by Kesting [12]. In a description of the dry process, Kesting [12] alludes to shrinkage and warpage in the drying of membranes, but does not provide any illustrative examples with degrees of collapse or pore sizes of the membranes. Sourirajan and Matsurra allude to collapse issues in cellulose acetate NIPS reverse osmosis membranes made by the "wet" process, but also fail to provide data on the degree of collapse [13]. Vos and Burris completed the best known in-depth study of effects of drying on RO membranes [9]. Their work examined various aqueous extractants' effects on tensile strength, salt rejection, and permeance in order to find a way to dry RO membranes without severe deleterious effects. They conclude that "membrane porosity is grossly reduced…[as] indicated by shrinking and curling of the irreversible membrane upon drying as well as by a substantial loss in desalination properties" [9].

The only known published study on microfiltration (MF) membrane shrinkage during drying was conducted with solid – liquid TIPS membranes from a polyethylene – mineral oil system [14]. That study used ten extractants with relatively low surface tensions and little polarity. The study showed a strong correlation of final membrane relative volume, final volume divided by the initial volume, to surface tension as shown in Figure 3.1. The strong correlation to surface tension implies the governing force in deformation during drying would be from capillary forces, as capillary forces are directly proportional to surface tension [14]. The proportionality of capillary forces to surface tension is given by the Young – Laplace equation and is discussed in detail in section 3.2.4.

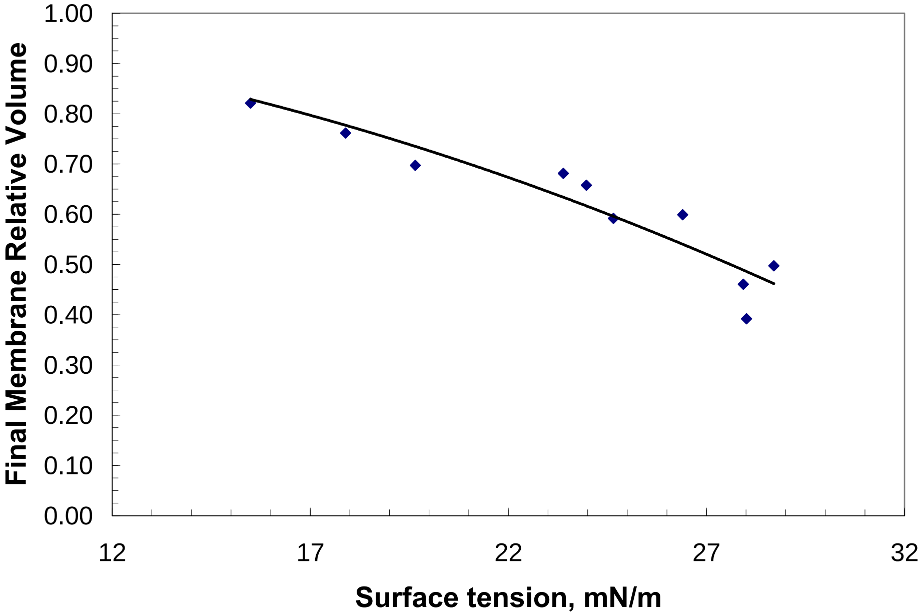

Figure 3.1: The effect of extractant surface tension on final relative volume for ten different extractants as reported by Matsuyama *et al.* [14].

In addition to the shrinkage observed by Matsuyama *et al.* [14], it is shown below that L−L TIPS polyethylene co-vinyl alcohol membranes had significant shrinkage, with cell sizes as small as 45% of the initial cell size prior to drying. Figure 3.2 below highlights the predominant forces assumed to be governing the collapse of the structure: capillary forces and elastic – plastic forces.

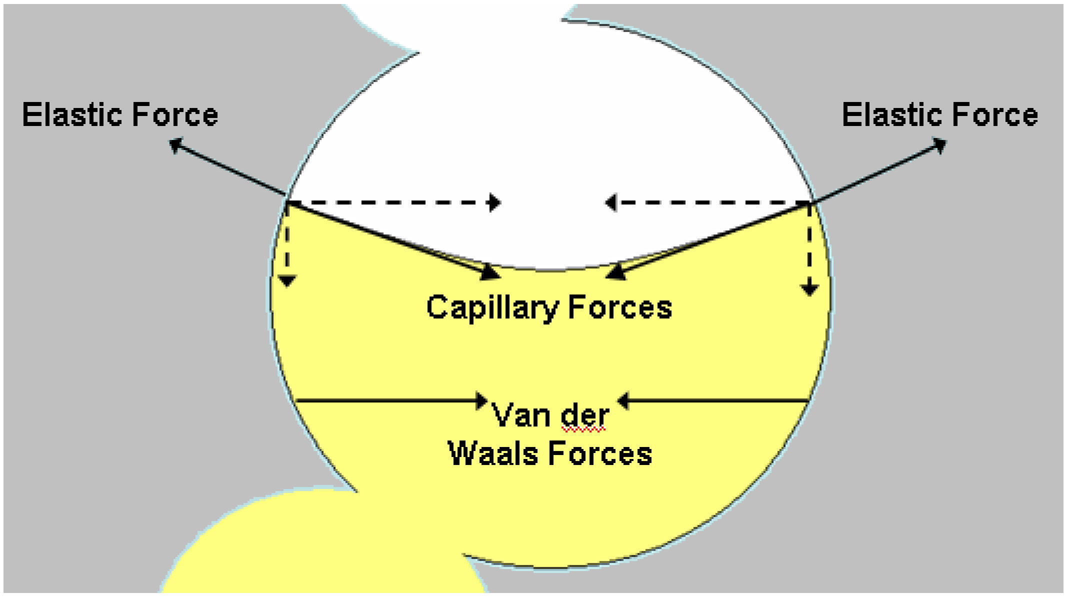

Figure 3.2: The predominant force in collapsing a cell is the capillary forces, which is resisted by the elastic forces. Van der Waals forces are included for completeness, but at length scales in micrometers the contribution of van der Waals forces are negligible. These forces are shown in a cellular structure, common from L−L TIPS membranes as shown in Chapter 2, but arise in any microporous membrane.

The work presented in this chapter seeks to relate polymer stress–strain behavior, extractant properties (surface tension, refractive index, boiling point, latent heat of vaporization, solubility parameters), and drying rate to the change in average cell size resulting from the drying. If successful, such a correlation could be used as a predictive tool to estimate the effect of drying on the final morphology of microporous membranes and thereby assist in controlling membrane morphology.

3.2 MODEL DEVELOPMENT

3.2.1 Modeling Approach

Modeling the deformation of an irregularly shaped object is a non-trivial problem and cannot be solved analytically to yield a closed form solution. As such, many problems of this nature are solved using finite element analysis. The modeling of deformation during drying was performed in this research using ABAQUS CAE, a commercial finite element software package. ABAQUS allows for multi-threaded computations of equilibrium equations to determine the deformed state of an object subject to a variety of forces and boundary conditions. ABAQUS has the ability to use implicit and explicit solution mechanics, along with static, dynamic, and nonlinear analysis.

It is worth noting that ABAQUS does not use a defined set of units. Rather, the user must maintain a set of self-consistent units. In the model described below, units are not assigned (following the ABAQUS convention), but the length scale is in micrometers, mass is in kilograms, time is in seconds, and all other units are made through a combination of these base units.

3.2.2 Part Generation and Mesh

The simulated membrane is constructed from data developed in the previous chapter. The cell location and cell sizes from the matrix solidification program are used as input in AutoCAD to create the object for an iPP membrane. For an EVAL44−glycerol membrane, the model is constructed by randomly placing spheres of a determined size and distribution inside of a cube until the appropriate porosity is attained. The spheres represent cells intersecting one another to form a co-continuous cellular structure. This co-continuous structure is subtracted from the volume of a cube to make the bi-continuous, cellular, and geometrically repeating unit as seen in Figure 3.3. The geometrically repeating unit has periodic boundaries such that a cell overlapping with one cube face appears on the opposite face as well. As in Chapter 2, this geometrically repeating unit has six identical neighbors and represents the interior of an L–L TIPS membrane, which avoids edge and end effects. AutoCAD is used because it is more user-friendly than the structure generating capabilities of the ABAQUS preprocessor. The AutoCAD object is easily imported into ABAQUS via the standardized ACIS SAT format. The repeating unit is called a part in ABAQUS and must be added to an assembly to assign forces and boundary conditions.

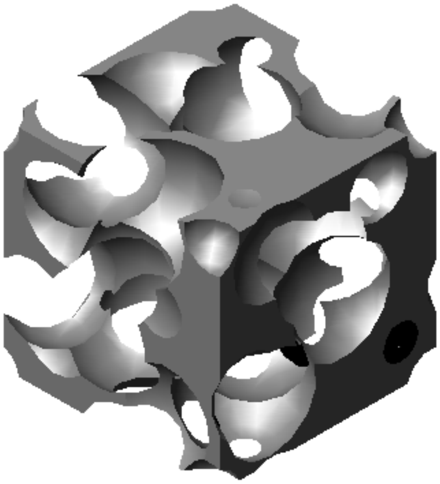

Figure 3.3: A geometrically repeating unit composed of unions of spheres to represent the connected cellular morphology typical of L–L TIPS membranes.

The 3D structure imported from AutoCAD was meshed independently with continuum 10 node modified quadratic tetrahedrals with hybrid linear pressure control (C3D10MH) elements. The quadratic version of the tetrahedral was used because the linear version is known to increase artificially the stiffness of a material due to the reduction in allowable deformations. Modified tetrahedrals reduce the computational time required. Hybrid pressure control is used to keep the volume of an element constant throughout deformation and is suggested for use when extreme distortions may appear. Hybrid pressure control is also required for this element when a material is modeled using hyperelasticity in order to capture the nonlinear portions of the stress–strain curve. Meshing algorithms are also incapable of using a less computationally intensive element, such as an 8 node rectangular brick.

A typical structural model will have a node seed size, or the distance between node placements, in the range of 0.5–0.7 (the total edge length is either 20 or 40 depending on the model), resulting in approximately 50,000 nodes and 30,000 tetrahedral elements. The nodes, node placements, and tetrahedrals are constructed by ABAQUS according to a proprietary algorithm. As there are three translational degrees of freedom for each node and one volumetric degree of freedom for each element, the problem requires significant computational power. A typical mesh is seen below in Figure 3.4.

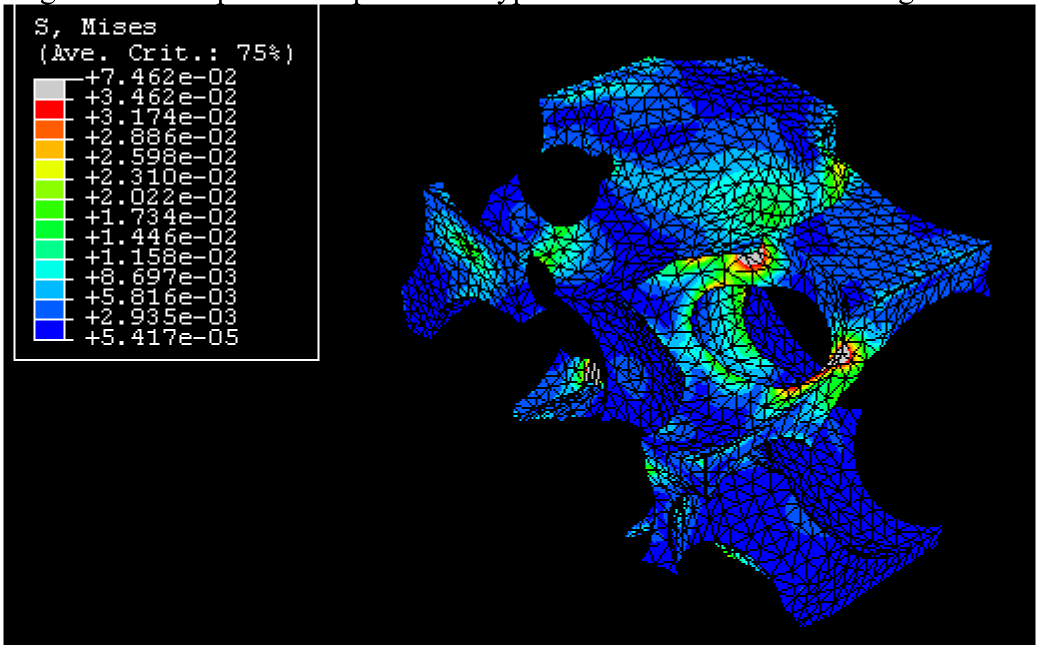

Figure 3.4: This simple object shows the mesh of tetrahedrals in the midst of drying. Higher levels of stress are indicated by hotter colors and gather on the thinner members of the object as expected.

3.2.3 Material Property Models

ABAQUS has many material models that have proven successful in modeling the behaviors of glassy and rubbery polymers [15-18]. ABAQUS has the capability to model most thermoplastic polymers used in TIPS or NIPS membrane production as a combination of hyperelastic (to capture non-elastic portions of the stress-strain curve) and viscoelastic behavior. In particular, the simulations presented here used a simple NeoHookean hyperelastic model and the proprietary ABAQUS Marlow model to model iPP and EVAL44 hyperelasticity. The Neo-Hookean hyperelastic model is given in Equation 3.1:

$$U = C_{10}\left(\bar{I}_1 - 3\right) + \frac{1}{D_1}\left(J^{el} - 1\right)^2 \qquad (3.1)$$

where U is the strain energy per unit of reference volume, C_{10} and D_1 are temperature-dependent material parameters, $\bar{I}_1$ is the first deviatoric strain invariant, and J^{el} is the elastic volume ratio. ABAQUS treats the relaxation moduli in viscoelastic problems by utilizing the Prony series [19], given by Equation 3.2:

$$E(t) = E_o \cdot \left(1 - \sum_{i=1}^{n} p_i \cdot \left(1 - e^{\frac{-t}{\tau_i}}\right)\right) \qquad (3.2)$$

where E_0 is the glassy modulus, p_i the constant coefficients, and τ_i is the relaxation time constant. The Williams–Landau–Ferry equation, given in Equation 3.3 [20]:

$$\log\left(a_t\right) = \frac{-C_1(T - T_{ref})}{C_2 + (T - T_{ref})} \qquad (3.3)$$

where C_1 and C_2 are universal constants, T is the temperature, and T_{ref} is 50°C above the polymer's glass transition temperature, was used by ABAQUS to calculate the time shift factor, a_t. The experimentally determined polymer parameters are given below in Table 3.1. Determination of the polymer properties is discussed in section 3.4.2.

Table 3.1: Physical response parameters of studied polymers obtained through experiments described in section 3.4.2. These values correspond well to literature [21, 22].

	iPP	EVAL44
Young's Modulus, E (GPa)	2.445	2.7
Yield Stress, σ_s (MPa)	28	59
Glass Transition Temperature, Tg (°C)	–17	55
Prony Series Coefficient, p_1, τ_1	0.81, 0.001	–
p_2, τ_2	0, 0.01	–
p_3, τ_3	0, 1	–
p_4, τ_4	0.2, 10	-
p_5, τ_5	0.2, 100	-

3.2.4 Forces and Boundary Conditions

The cavity space on the inside of the geometrically repeating part, such as that shown in Figure 3.4, was subject to a varying capillary force. The capillary forces are based upon the Young – LaPlace equation:

$$P_c = \gamma * \cos\beta * \frac{dS}{dV} \tag{3.4}$$

where P_c is capillary pressure, γ is surface tension, β is the contact angle, dS is the amount of surface area uncovered, dV is the amount of volume of the extractant evaporated to uncover dS. The capillary pressure is calculated for given time increments in a Matlab program referenced in Appendix B (along with the other computer code used in this chapter.) This program makes the assumption that the meniscus recedes as a plane through the structure. A set step change through the thickness of the sample allows calculation of dS and dV with a Monte Carlo routine. Once the volume of extractant evaporated is known, a drying model can be used to determine the amount of time needed for evaporation. The values for time, *dS*, and *dV* are tabulated for each step through the structure. These results from Matlab are then coded in Fortran into a user-defined ABAQUS routine, DLOAD, to allow the pressure to vary over time and throughout the structure. Once the receding meniscus has passed an element, it is no longer subjected to the capillary force and may reduce stress by rebounding according to its material response curve. Figure 3.5 below provides a simple illustration for computing *dS* and *dV*. The simple cell is divided into several sections as if a planar meniscus were receding into the structure. The sectioning allows for computation of capillary forces, as the surface area of the cell and the void volume of each section is easily calculated.

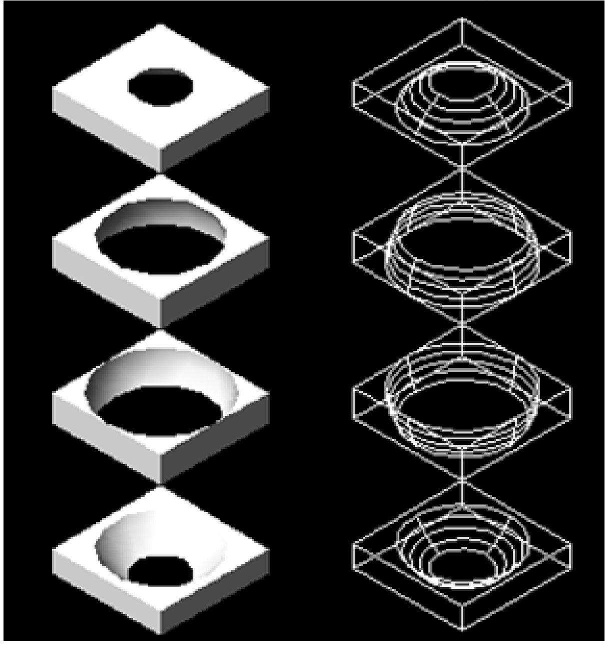

Figure 3.5: A simple schematic of a cell divided into four sections for computation of capillary forces. The same sectioning procedure for computation is carried out on the more complex models pictured elsewhere in this chapter.

Boundary conditions on the structure were required to enforce the geometrically repeating capability, prevent excessive and extraneous distortion, and prevent displacement of the entire object. Even though the structure is geometrically repeating, the stresses generated by drying do not balance, resulting in the structure attempting to accelerate and move rather than simply deforming. It is also desired to keep the remaining area of the cube's six original faces, here after referred to as the part faces, planar such that the final deformed structure can be geometrically repeating. There are also instances of significant imbalances in the forces that cause extreme distortion to certain elements, particularly if it is part of some arm of elements, which would not occur if the entire membrane could be simulated. As such, special constraints are added as needed to prevent behavior like that seen below in Figure 3.6.

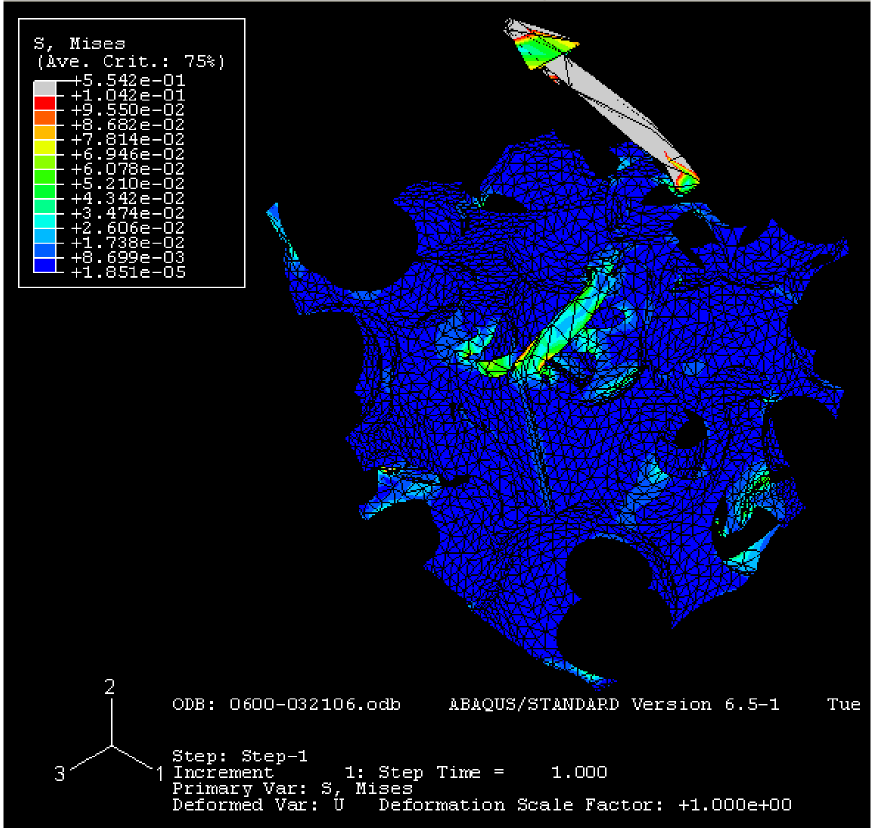

Figure 3.6: Extreme distortion on an arm of elements can result in solution algorithms breaking down due to extreme stress and distortion of elements.

Originally, boundary conditions placed on an entire part face to limit a degree of freedom in a given direction. An example would be to fix the displacement of a part face on one of each of the axes to prevent the object as a whole from displacing. However, for the few nodes that exist on the edges of two or three part faces, this meant restricting two or three degrees of freedom, respectively. This produced an error in ABAQUS, even though the program is theoretically capable of solving such a problem. Consequently, an alternative method of placing boundary conditions was necessary.

The ABAQUS error with regards to restricting multiple degrees of freedom remained persistent in the simulation development. The solution to this problem was to remove the interface between part faces, leaving a structure like that shown in Figure 3.7. It was also found best to use a combination of "tie" and "equation" restraints to make the structure deform appropriately. The part faces of the structure are tied to a reference point, such as RP-1 in Figure 3.7. This reference point then governs the displacement of the nodes that are tied to it. It is possible to put displacement restrictions on the reference point such that it can only move along a given axis, keeping the part faces planar during deformation.

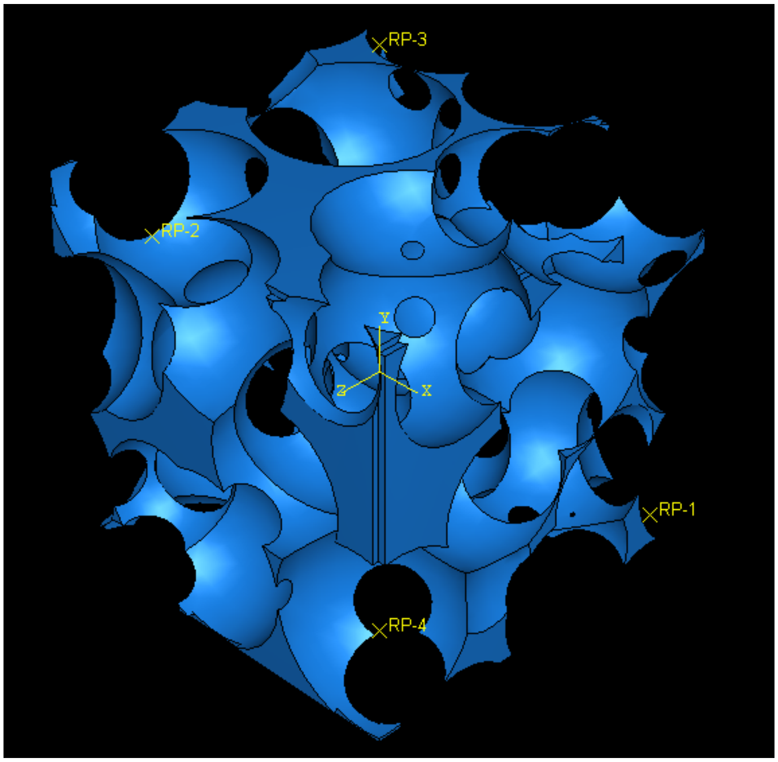

Figure 3.7: By eliminating the shared edges between part faces, errors in ABAQUS could be avoided to allow the analysis to proceed.

3.2.5 Available Drying Rate Models

Porous materials can undergo several stages of drying that correspond to specific physical phenomena.

- The first stage of drying is the constant rate period (CRP). In this stage, a thin continuous film of liquid is maintained at the surface of the membrane, resulting in the fastest portion of drying. The continuous film of liquid is continually replenished by the object contracting under capillary pressures and forcing fluid from the interior to the surface of the membrane.
- Once the object can no longer deform to maintain the continuous film, the liquid recedes inside of the pores and drying enters the *first falling rate period* (FFRP).

- Once the pores have been emptied of the unbound or bulk fluid within the cell or pore, the *second falling rate period* (SFRP) begins. In this drying regime, "bound" fluid, adsorbed or absorbed into or on the polymer, is removed through desorbtion processes.

The CRP has the fastest removal of extractant due to the large surface area, while the SFRP has the slowest removal and can take considerable lengths of time.

Drying of porous materials is an active research field, providing many choices of drying rate models from which to choose. However, many of the existing models of drying and fluid transfer through porous media are developed for specific situations that are not general enough for membrane drying, as described below.

Recent advances in drying of porous media have focused on using pore networks, where the term pore in this context would correspond to the cell of a L–L TIPS structure. The development of these networks is well reviewed by Prat [23]. While providing qualitative drying rates, the pore network models have predicted drying rates up to six-fold lower than the experimentally observed rates [24]. The discrepancy between the model and the experimental results is primarily due to the lack of inclusion of secondary capillary effects, particularly corner and flow films. Yiotis *et al.* recently included these effects of liquid films in a 2-D pore network [25]. However, several limitations still exist that preclude the use of this model to obtain quantitative results, including: the solid matrix cannot be swollen with liquid; variability in the cell microstructure is minimized; the model neglects intercluster mass transfer by films; and the mathematical transformations used ignore heterogeneity in diffusive conductances for different cells [25]. Additionally, Prat asserts that a true CRP cannot be determined through using a 2-D network; only a 3-D network will be able to predict accurately [23], while significantly increasing computation time [26]. Other issues with pore network models include:

evaporation is only from one surface, models are for "slow" drying, only perfectly wetting fluids have been modeled, and only narrow cell and pore size distributions have been modeled [23].

Another possible drying rate choice would be some kind of adaptation of the work by Whitaker concerning volume averaging methods [27, 28]. However, Whitaker's work also has limitations: solids are assumed to be rigid and the theory is limited to dilute vapor-phase solutions. The ability to predict the effective coefficients through the complex closure problems in the coupled mass and energy equations is limited to temperatures at or below 40°C for water [28]. Obviously, the walls of polymer membranes during deformation are not rigid and the temperature during drying in industrial processes is often above 40°C.

Ultimately, a simple drying rate model for porous materials was used in this research. The CRP of drying a porous material continues as long as the structure deforms in order to push liquid to the surface in order to maintain an unbroken liquid film [29]. When the material will no longer deform to push liquid to the surface, the CRP ends. Thus, the final state of the structure at the end of the CRP corresponds closely to a static–equilibrium solution of the structure under a capillary force that corresponds to the largest pore on the surface of the structure.

Once the CRP has ended, the meniscus of the fluid recedes into the cellular structure and can be modeled with one of a variety of empirical fits [30]:

$$t_f = \frac{\rho_s d\lambda\left(W_c - W_e\right)}{h_t\left(T - T_s^{'}\right)} \ln \frac{W_c - W_e}{W - W_e} \tag{3.5}$$

where t_f is the drying time in the FFRP, h_t is the total heat-transfer coefficient, λ is the latent heat of evaporation, T is the dry bulb temperature, ρ_s is the bulk density of the dry material, d is the thickness of the membrane, W_c is the moisture content at the beginning of the falling-rate period, W_e is the moisture content in equilibrium with the environment, and *W* is the moisture content at a given time. This model was used for its simplicity and that all variables are known or easily calculated. The drying rate model for the FFRP is easily substituted into a Matlab program to generate the capillary pressures for ABAQUS.

3.2.6 Simulation Steps

The simulation of drying occurs in several steps and is made with several assumptions. One assumption is that evaporative cooling has a negligible effect on the morphology change of the structure. As such, the simulation assumes an isothermal temperature of 25°C for all steps. A second assumption is that deformation occurs primarily during the CRP and the first falling rate period. While there may still be bound extractant that would evaporate during the second falling rate period, the membrane is mostly dry and no longer has a meniscus driving capillary forces during the SFRP. As such, only the CRP and the first falling rate period are simulated. A third assumption is that the viscoelastic response during the build-up of capillary forces caused by drying is negligible. Disregarding the viscoelastic response during build-up of capillary forces allows the CRP portion of deformation to be modeled with a static–equilibrium step. Ignoring the viscoelastic response of the material can reduce computational time. For all steps the ABAQUS option of non-linear geometry (NLGEOM) is selected, requiring the equilibrium equations to be solved on the continually deforming shape, rather than computing the forces and a given displacement based on the original shape. The first falling rate period utilizes a viscoelastic step (VISCO) to incorporate the viscoelastic response in order to capture the diminishing stress in elements due to relaxation. The VISCO step utilizes the user-defined load function DLOAD to control the varying forces on the membrane cell cavities during drying. A third step utilizes VISCO to allow the structure to relax and rebound after the end of the FFRP has ended.

3.3 MODEL RESULTS AND DISCUSSION

3.3.1 Deformation Results

The ABAQUS simulations predicted no significant permanent deformation. Rather, all of the deformation that occurred was elastic, as seen in Figure 3.8 below. This elastic deformation dissipated with the removal of the applied stresses from the capillary forces. The ABAQUS model could not predict stresses above the yield stress, thus the elastic region of the stress–strain relationship controlled the entire deformation. The original load placed on the membranes during the CRP portion of the simulation is the capillary force of the largest pore opening on the surface. For the case of EVAL44 with cell sizes of 0.35 micrometers and water as an extractant, the capillary pressure varies from less than 1 MPa to 2 MPa, and stresses of approximately the same magnitudes are generated. While these forces may produce a volume shrinkage of approximately 30%, once removed the membrane elastically rebounds to its initial configuration.

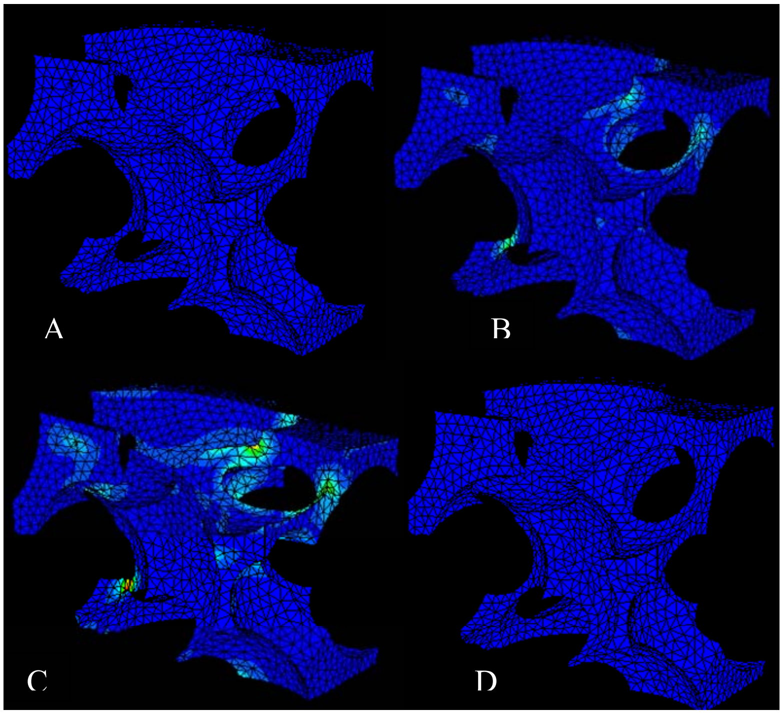

Figure 3.8: Stress is developed as the structure collapses under capillary force, but only results in elastic deformation, allowing the structure to return to its original configuration after drying is complete. (A) is the initial state, (B) and (C) show developing stress in the structure, and (D) is the final state of the structure after returning elastically to its original configuration.

The ABAQUS simulations were run on a Dell Workstation with two 3.2 GHz duo-core processors and 4 gigabytes of RAM. A full simulation can take upwards of 48 hours before completion or reaching a point where the solution routine will no longer converge.

3.3.2 Potential Forces and Phenomena in the System

3.3.2.1 Capillary Forces

Attempts to model the deformation of cellular microporous membranes were initially based upon capillary forces being the dominant mechanism as indicated by Matsuyama *et al.*[14]. These modeling attempts predicted no permanent deformation of the geometries as the yield stress reported in Table 3.1 for the polymers was never exceeded.

In order to examine the effectiveness of the ABAQUS simulations, a simplified approach to deformation of the microporous cellular geometries was implemented. The non-linear hyperelastic behavior of the polymers was neglected and only the linear elastic response (characterized by Young's modulus) and yield stress was considered. The geometry of the samples was reduced to (i) a hollow cylinder and (ii) a hollow sphere.

Taking the simplest route of modeling the membrane as a cylinder through a polymer plate (similar to an ideal track-etch membrane) leads to a simplified expression of the Young – LaPlace equation:

$$P_c = \gamma * \cos\beta / R \qquad (3.6)$$

where R is the radius of the cell. Assuming that the fluid is completely wetting ($\cos\beta = 1$), using the large surface tension of water (72.5 mN/m), and P_c is 28 MPa (the minimum yield stress required for permanent deformation for iPP, which is less than the 59 MPa required for EVAL44) results in a required radius of 2.5 nm to achieve permanent collapse. The required radius is two orders of magnitude less than the smallest cell size of the membranes (350 nm) being modeled in the current study. Using the 10% rule of thumb for pore size relative to cell size [31], the required radius is an order of magnitude less than the pore size of the membranes (35 nm). It should be noted that in these particular membranes, the pores do appear to be larger than what is predicted by the 10% rule of thumb.

Assuming the membrane can be modeled as a hollow sphere adds only a coefficient of 2 to the right hand side of Equation 3.6, resulting in a required radius for deformation of 5 nm, which obviously does not correspond to the cell size of the studied membranes. The hollow sphere was then modeled as having a spherical meniscus contacting the walls at a given contact angle as seen below in Figure 3.9. Capillary pressures were calculated with Equation 3.4, with *dS* and *dV* coming from Monte Carlo routines run in Matlab. With a small contact angle (5 degrees) and a cell radius of 0.6 μm, capillary pressures can reach up to 18 MPa, which is still smaller than the required 28 MPa of the yield stress for iPP and 59 MPa for EVAL44. However, this is only for the very bottom of the cell. If we include a pore of average size, this portion of the surface area of the cell is eliminated and the maximum capillary pressure achieved is around 5 MPa.

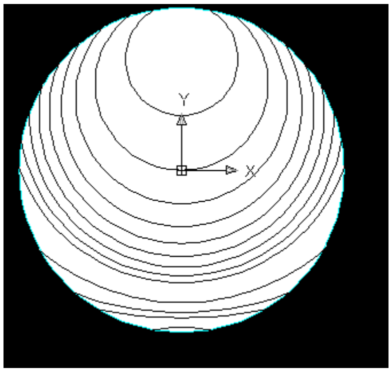

Figure 3.9: The shape of a meniscus in a hollow sphere for a fluid with a contact angle of 20°.

3.3.2.2 Plasticization

The effect of extractants as plasticizers on the membranes was also examined. Extractants typically have low surface tensions and do not serve as swelling agents or solvents for the polymers at room temperature. No measurable change in material volumes was observed during the extraction process in experiments, which indicates no swelling was occurring. The lack of swelling of TIPS systems during the extraction process has also been noted in literature [14]. In the case of EVAL44, it has been known to absorb up to 5 wt-% water in saturation conditions [32]. Using this as a worst case scenario results in a slight depression of the glass transition temperature from 55°C to 50.8°C using the simple plasticization model given in Equation 3.7:

$$T_g = \left(\frac{wt\%\,polymer}{T_{g,polymer}} + \frac{wt\%\,plasticizer}{T_{g,plasticizer}} \right)^{-1} \qquad (3.7)$$

The slight depression of the glass transition temperature should have negligible impact on drying at 25°C. Literature supports the conclusion that annealing below the glass transition temperature of EVAL has little effect on the morphology [33].

3.3.2.3 Other forces

Other short range inter-molecular forces and body forces have been considered. Van der Waal's forces can exert enormous forces on a surface, but only act in the tens of nanometers range, which is well below the characteristic distance for the membranes observed. To investigate a possible effect of gravity forces, the membranes were dried parallel to the ground. From SEM images, an example of which is given in Figure 3.7b below, there is no compression of one side of the membrane that would indicate that the gravity forces are not deforming the cellular morphologies. It is unreasonable to expect that electric, magnetic, or thermal based stresses are occurring within the samples as well.

3.3.2.4 Effect of neighboring cells

As the cells of the membrane do not exist in isolation, but are surrounded by other cells, a single unit cell in a hexagonal-closest pack morphology was simulated in ABAQUS using the 5 MPa force determined in section 3.3.2.1. This simulation resulted in no permanent deformation of the sample.

3.3.2.5 Drying rate models in drying simulations

Thus far drying rate has been ignored as a primary variable in the simplified modeling and to a large extent in the complex geometries used in ABAQUS (a few simulations employed a rudimentary drying rate but had convergence issues or showed no permanent deformation). If viscoelastic properties were included, it would be reasonable to expect the interior of the membranes to have smaller cells and a noticeable gradient to the surface because whatever forces are causing the deformation would have longer to act. However, only in one condition has this been experimentally seen; EVAL−glycerol in a 40-60 wt% mixture extruded at 170°F with water extraction as seen below in Figure 3.10a. All other membranes have been isotropic throughout, with a possible exception to the outermost layer of cells on the surface, as seen in Figure 3.10b.

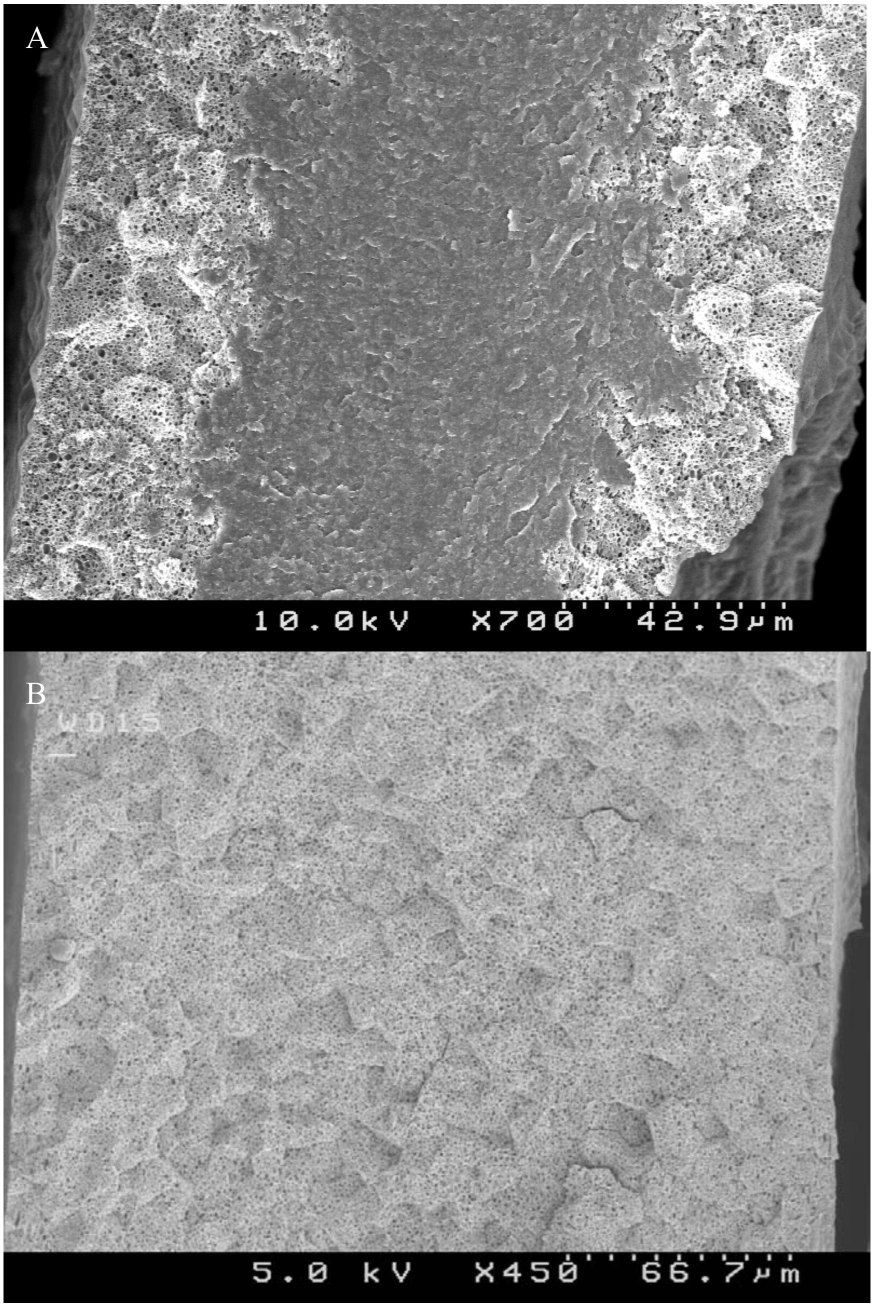

Figure 3.10: In figure 10a (top) there is a noticeable size difference between cells in the interior and exterior of the membrane that is not observed with other extractants, like cyclohexane pictured in 10b (bottom).

3.4 EXPERIMENTAL MATERIALS AND METHODS

3.4.1 Materials

The primary TIPS system used in the drying experiments reported here is poly(ethylene co-vinyl alcohol) (EVAL) – glycerol. EVAL44 (44 mol% ethylene) was selected because of the large miscibility gap allowing many different compositions and commercial interest in the polymer as shown below in Figure 3.11. The EVAL44 – glycerol films were extruded as flat sheets onto a textured temperature controlled wheel and provided by 3M. EVAL pellets were obtained from EVALCA, with the grade for 44 mole-% ethylene being E151A. Glycerol and the extractants were obtained from Fisher. All compounds were used as received without further purification. In figures and text below, short hand notation will be used, such as 50–50, 150°F, to describe a membrane where a solution of 50 wt% EVAL44 and a 50 wt% glycerol was extruded onto a temperature controlled textured wheel at 150°F.

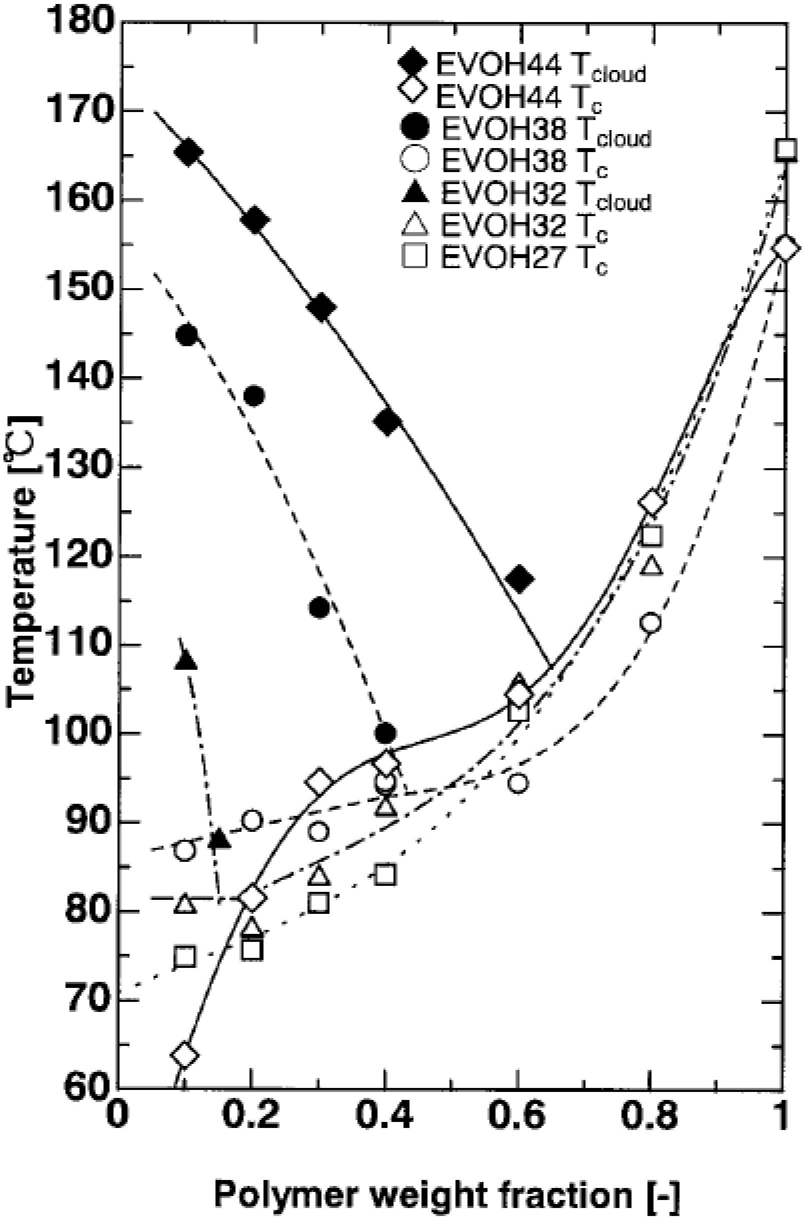

Figure 3.11: EVAL – glycerol phase diagram from Shang *et al.* [34]

3.4.2 Physical Property Determination

EVAL and iPP physical properties were determined using uni-axial elongation experiments. The pellets of the polymer were melted and pressed into films with an irregular cross-section. These films were then rolled on a heated 2AY-84 Brabender prep (two-roll) mill in order to thin the films and provide an even thickness between 180 – 300 μm.

The produced films were then used to gather the physical properties the polymer by using a T.M. Long bi-axial stretching device donated by the 3M Company. The stress–strain behavior used in the modeling was determined by stretching dense films at room temperature and at a rate of 1 cm/s in the direction the films were extruded. Stress was calculated by monitoring the force on the films with a load cell while the film elongation was controlled via Labview software. Viscoelastic properties were determined using small strain relaxation tests at various temperatures ranging from 80°C to 170°C. The results from these property determinations were given in Table 3.1 above. A more complete discussion about the T.M. Long device can be found in section 4.2.2.

3.4.3 Drying Experimental Procedure

The membranes were cut into 2”x2” samples and extracted in six extractants: pentane, cyclohexane, acetone, isopropyl alcohol, methanol, and water. The samples were dried at room temperature by hanging them perpendicular to the ground except where noted above for investigating gravity effects. Additional samples were restrained by clamping them into aluminum frames. All non-restrained samples were extracted and dried in duplicate or triplicate.

Cell size was determined by freeze-fracturing membranes in liquid nitrogen and imaging in a Hitachi S-4500 SEM after being sputter-coated with gold. The images were analyzed with ImageJ software to determine the area of each cell, and an effective diameter was calculated assuming the area is that of a circle.

Contact angles of the extractants on dense polymer films, prepared as described above, were measured using a Ramé-Hart 100 goniometer. Once calibrated, a droplet of the extractant was placed on the film. A camera was used to image the droplet, Figure 3.12 is a typical picture, and software on the controlling computer calculated the contact angles on the left and right side of the droplet. The contact angle used is the average of the two calculated angles. The contact angles are tabulated in Appendix C with other supplementary data from this chapter.

Figure 3.12: Acetone on an EVAL44 film.

3.5 EXPERIMENTAL RESULTS AND DISCUSSION

Cell size analysis of the EVAL44 – glycerol films yields no correlation with effective surface tension, refractive index (an indicator of the Hamaker constant), Hildebrand solubility parameter, or Hansen solubility parameters as shown in Figures 3.13-3.15. The data is reproducible without excessive scatter. The results for surface tension and refractive index are contradictory to those found by Matsuyama *et al.*, but support their evidence of no dependence on solubility parameters. Additional parameters were investigated hoping to find some trend that would point to a governing force, including: boiling point, dielectric constant, cohesive energy density, diffusion coefficients in air, heat of vaporization, and non-dimensional groupings of extractant properties. As these parameters yielded no conclusive results and are not pertinent to the major points of discussion here, they are presented in Appendix C.

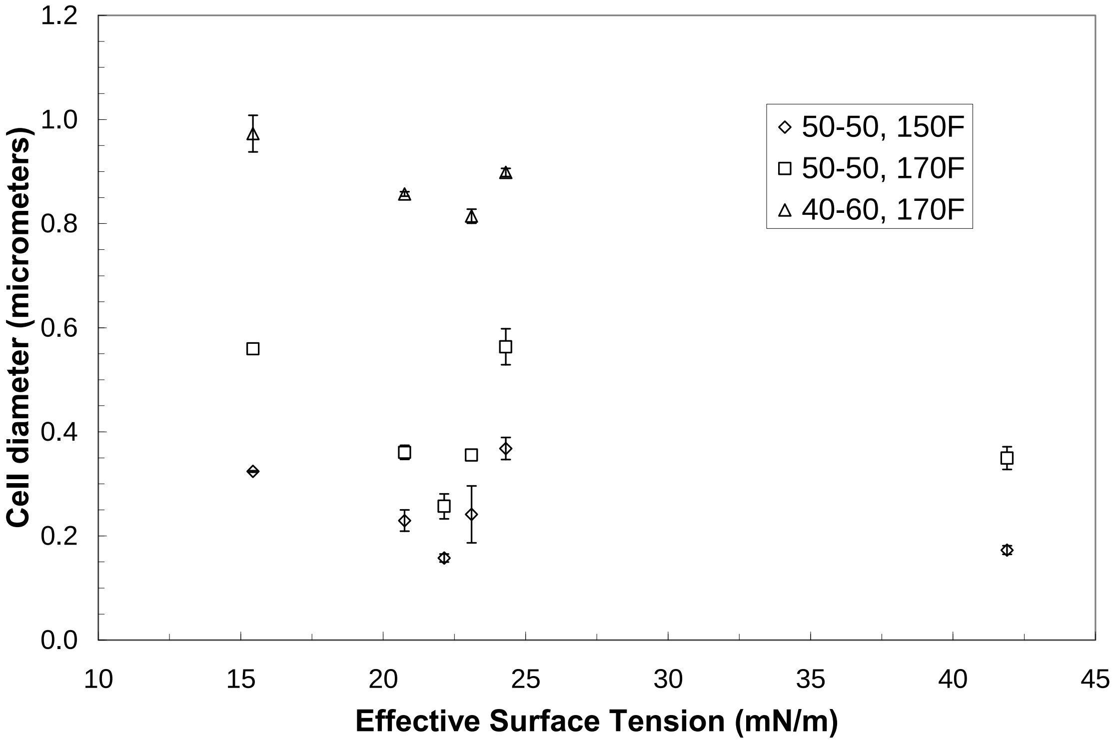

Figure 3.13: EVAL44–glycerol membranes formed at different temperatures and compositions exhibit no correlation with surface tension, although the same pattern holds for all three starting cell sizes. Values for EVAL 40-60, 170°F extracted and dried with methanol and water are not reported as the membranes are not isotropic and have no meaningful average cell size as seen above in Figure 3.10a.

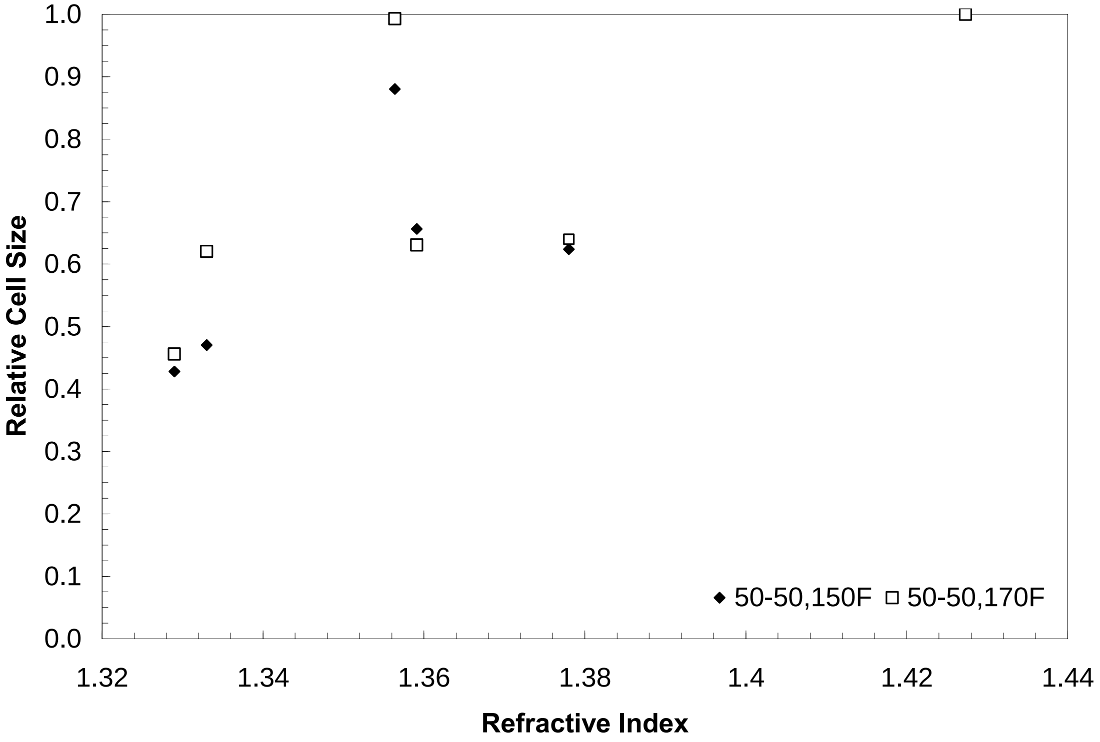

Figure 3.14: The shrinkage of EVAL44 – glycerol membranes show no definitive trend with the index of refraction of the extractant.

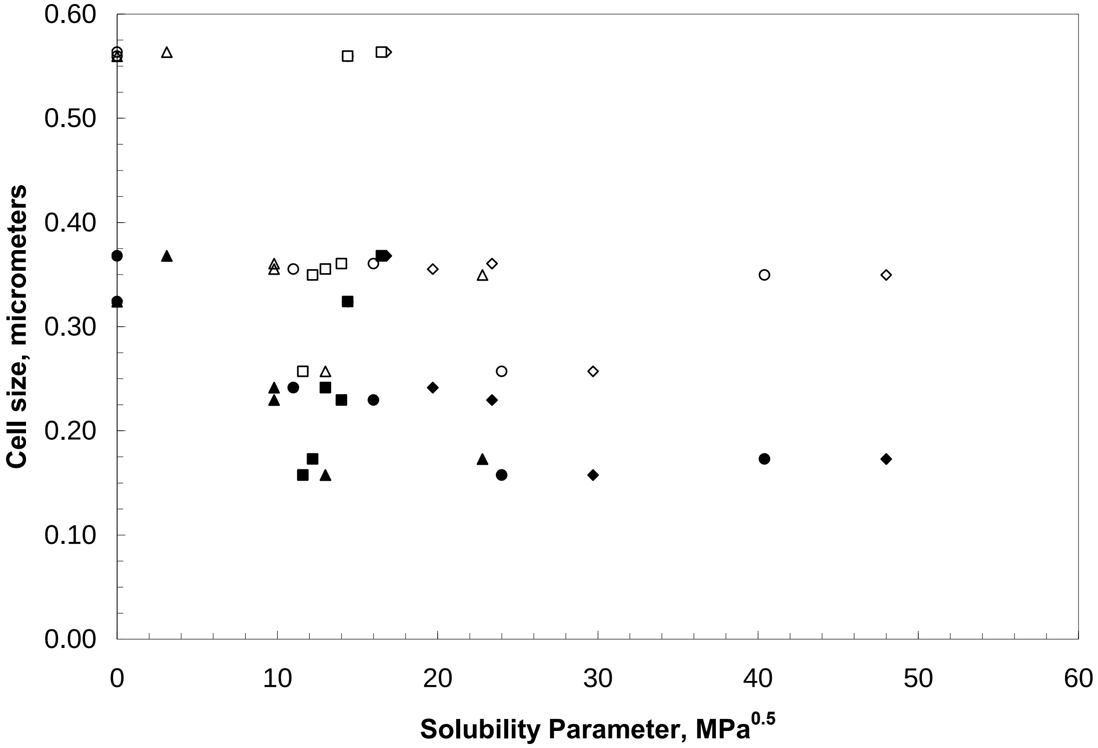

Figure 3.15: The shrinkage of EVAL44 – glycerol membranes show no definitive trends with the Hildebrand (diamond), dispersive (square), polar (triangle), or hydrogen-bonding (X) solubility parameters. EVAL 50-50, 150°F membranes are represented by the filled markers and EVAL 50-50, 170°F membranes are represented by the open markers.

The results for each membrane in Figure 3.13 follow the same general trend for each extractant, regardless of cell size. If capillary forces were the dominant mechanism, it would be expected that the 40-60, 170°F membranes would have experienced less collapse than the other two due to the inverse relationship between capillary forces and cell size.

To further investigate the phenomena occurring during drying, more extractants were chosen to be used with 50–50, 150°F membranes. Longer chain alkanes, 2-ketones, and primary alcohols were used and did not show any further clarification in the dominant mechanism or the influence of capillary forces, as shown below in Figure 3.16. Appendix C has extraneous plots of cell size versus extractant parameters that do not show any predictive capability. It should be noted that generic trends, such as ketones caused more shrinkage than alkanes, can be drawn from some graphs in Appendix C. However, within an extractant group, there is little predictive capability of shrinkage.

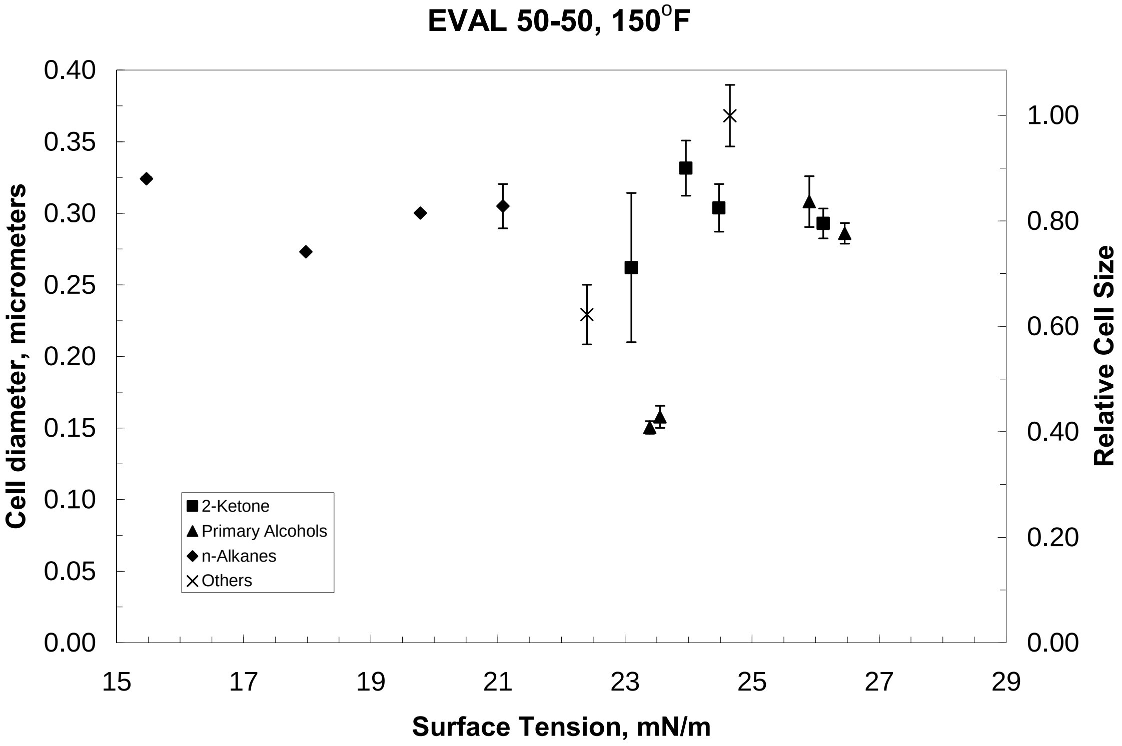

Figure 3.16: EVAL44 50-50 wt%, 150°F membranes show no correlation between cell diameter and surface tension.

While the experimental data does not show any single dominant collapsing mechanism, it is possible to extract an additional heuristic for use during drying. As indicated in the introduction, the most common heuristics for selecting an extractant are:

1. The extractant is not a solvent.
2. The extractant is not a swelling agent.

3. The extractant has a low surface tension.
4. The extractant is economical.

The first three heuristics are required in order for significant collapse of the structure to be avoided, and the fourth heuristic is necessary for commercial production. Applying these heuristics might lead one to select methanol, surface tension of 23.55 mN/m, as an appropriate extractant for EVAL44. However, Figure 3.16 clearly demonstrates that methanol is the worst possible choice out of the plotted extractants (water is not plotted but is comparable in cell size) because of the large degree of collapse of the structure. Research in the drying of reverse osmosis membranes by Vos and Burris yielded a similar finding [9]. In their work they predicted that an aqueous solution with a surface tension of 19 mN/m, FC-170 obtained from 3M, would provide a dried membrane with better performance than that of a 60 wt% glycerol aqueous solution with a surface tension of 69 mN/m. The permeance of the FC-170 dried membrane was approximately 36% of the glycerol membrane. The FC-170 membrane also had a salt rejection of 69% as opposed to 94% for the glycerol [9].

In light of the conclusions from MF and RO research, it is then proposed to add a fifth heuristic- an extractant is to be chosen to be more alkane-like, even if it has a higher surface tension than a small alcohol or ketone. Being more alkane-like will reduce the interaction with a polar polymer like EVAL44, yet still wet the nascent membrane. Using the five heuristics it should be possible to select an extractant that will minimize collapse of the structure without extensive lab comparisons.

3.6 CONCLUSION

Cell shrinkage was shown to occur in EVAL44 – glycerol membranes dried with a variety of extractants, with the smallest average cell size 45% of the non-collapsed average cell size. Figures 3.13-3.16 provide strong evidence that shrinkage is not dominated by capillary forces or some interaction between the extractant and the solid polymer matrix. There are no clear trends resulting from the experiments that will provide predictive capabilities, although the pattern of shrinkage in EVAL44 with the six original extractants holds regardless of starting cell size.

The strong correlation found by Matsuyama *et al.* may be a result of looking at a narrow range of extractants. With the exception of trichloroethane, MEK, and 2-butanone, the solvents are non-polar hydrocarbons within a small range of surface tension values. It is reasonable to hypothesize that due to the similarity between the extractants that several trends would hold true. It is unfortunate that no repeatability data is given by Matsuyama *et al.* to see how much each data point varies from the reported trend. It should also be noted that the membranes used by Matsuyama *et al*. were formed by S–L TIPS and do not display the same cellular morphologies of the membranes experimentally dried in this study.

It is worthwhile to note that the simulations, assuming the determined material properties of the bulk polymer are accurate and appropriate for the cellular structures, indicate that capillary forces alone due not have the capability to deform the cellular membranes, which supports the lack of cell size dependence on surface tension in Figures 3.13 and 3.16. Capillary forces may be the dominant mechanism for shrinkage in the UF range, as the polymers typically used for UF membranes formed via NIPS, like the polyimide used at Twente [8] or PES, often have yield stresses and Young's moduli an order of magnitude weaker than the polymers considered here. Also, as the pores in UF are on the order of tens of nanometers, the capillary forces generated are much closer to what the simplified modeling in this chapter suggests is necessary for capillary forces to govern deformation. The irreproducibility noticed by Beerlage [8] and McDonogh [35] in UF drying may be a result of uneven geometrical and numerical distributions of macrovoids formed in the NIPS process. These hypotheses are difficult to confirm due to a lack of reported data for their systems. The work of Vos and Burris [9] further corroborate the complex nature of drying membranes, as the shrinkage noticed in collapse of cellulose acetate RO membranes did not correspond directly to surface tension. In view of the results of the works detailing drying across three separate sizes of membranes, it is proposed to add a heuristic in extractant choice – choose an extractant that is more alkane-like, even at the expense of increasing surface tension.

3.7 REFERENCES

1 A.J. Castro, *Methods for making microporous products*, US Patent 4,247,498, 1981.

2 W.C. Hiatt, G.H. Vitzthum, K.B. Wagener, K. Gerlach, and C. Josefiak, *Microporous membranes via upper critical temperature phase separation*, in: D.R. Lloyd (Ed.), Materials Science of Synthetic Membranes, ACS Symposium Series, #269, ACS Press, Washington, DC, 1985, pp. 229-244.

3 G.T. Caneba and D.S. Soong, *Polymer membrane formation through the thermal-inversion process. 1. Experimental study of membrane structure formation*, Macromolecules, 18 (1985) 2538-2545.

4 D.R. Lloyd, K.E. Kinzer, and H.S. Tseng, *Microporous membrane formation via thermally-induced phase separation. I. Solid-liquid phase separation*, Journal of Membrane Science, 52 (1990) 239-261.

5 D.R. Lloyd, S.S. Kim, and K.E. Kinzer, *Microporous membrane formation via thermally-induced phase separation. II. Liquid-liquid phase separation*, Journal of Membrane Science, 64 (1991) 1-11.

6 P. Manos, *Membrane Drying Process*, US Patent 4080743, 1978.

7 W. Admassu, *Process for drying water - wet polycarbonate membranes*, US Patent 4843733, 1989.

8 M.A.M. Beerlage, *Polyimide ultrafiltration membranes for non-aqueous systems*, Dissertation, University of Twente, 1994.

9 K.D. Vos and F.O. Burris, *Drying cellulose acetate reverse osmosis membranes*, Industrial and Engineering Chemistry Product Research and Development, 8 (1969) 84-89.

10 S. Loeb and S. Sourirajan, *Sea water demineralization by means of an osmotic membrane*, Advan. Chem. Ser. (ACS), 38 (1963) 117.

11 S. Sourirajan, *Reverse Osmosis*, Academic Press, New York, 1970.

12 R.E. Kesting, *Synthetic polymeric membranes: a structural perspective*, 2nd ed, John Wiley and Sons, New York, 1985.
13 S. Sourirajan and T. Matsurra, *Reverse osmosis/ultrafiltration process principles*, National Research Council Canada, Ottawa, Canada, 1985.
14 H. Matsuyama, M.-M. Kim, and D.R. Lloyd, *Effect of extraction and drying on the structure of microporous polyethylene membranes prepared via TIPS*, Journal of Membrane Science, 204 (2002) 413-418.
15 J. Sweeney, P. Caton-Rose, P.D. Coates, *The modeling of large deformations of pre-oriented polyethylene*, Polymer, 43 (2001) 899-907.
16 L.S. Worrel, *Modification of Track-Etched Membrane Structure and Performance via Uniaxial Stretching*, Dissertation, The University of Texas at Austin, 2005.
17 J.A. Morehouse, D.R. Lloyd, B.D. Freeman, D.F. Lawler, K.M. Liechti, and E.B. Becker, *Modeling the stretching of microporous membranes*, Journal of Membrane Science, 283 (2006) 430-439.
18 J.D. Wu and K.M. Liechti, *Multiaxial and Time Dependent Behavior of a Filled Rubber*, Mechanics of Time-Dependent Materials (2000) 293-331.
19 K. Hibbitt, and Sorensen, *ABAQUS Theory Manual*, 1998, pp. 4.6.1-1 - 4.7.2-10.
20 M.L. Williams, R.F. Landel, and J.D. Ferry, *The temperature dependence of relaxation mechanisms in amorphous polymers and other glass-forming liquids*, Journal of the American Chemical Society, 77 (1955) 3701-07.
21 EVALCA, *EVAL E151 Data Sheet*, (2004).
22 M. Montoya, M.J. Abad, L. Barral, and C. Bernal, *Mechanical and fracture behavior of polypropylene/poly(ethylene-co-vinyl alcohol) blends compatibilized with ionomer* Na^+, Europeapn Polymer Journal, 42 (2006) 265-273.
23 M. Prat, *Recent advances in pore-scale models for drying of porous media*, Chemical Engineering Journal, 86 (2002) 153-164.
24 J.B. Laurindo and M. Prat, *Numerical and experimental network study of evaporation in capillary porous media. Drying rates*, Chemical and Engineering Science, 53 (1998) 2257-2269.
25 A.G. Yiotis, A.G. Boudouvis, A.K. Stubos, I.N. Tsimpanogiannis, and Y.C. Yortsos, *Effect of liquid films on the drying of porous media*, AIChE Journal, 50 (2004) 2721-2737.
26 A.G. Yiotis, A.K. Stubos, A.G. Boudouvis, and Y.C. Yortsos, *A 2-D pore-network model of the drying of single-component liquids in porous media*, Advances in Water Resources, 24 (2001) 439-460.
27 S. Whitaker, *The method of volume averaging*, 13, Kluwer academic publishers, Dordrecht, 1999. pages 219.
28 S. Whitaker, *Coupled transport in multiphase systems: a theory of drying*), Advances in heat transfer, 31, Academic Press, San Diego, 1998, pp. 1-158.
29 C.J. Brinker and G.W. Scherer, *Sol-gel science: the physics and chemistry of sol-gel processing*, Academic Press, Boston, 1990. pages 908.
30 R.H. Perry, D.W. Green, and J.O. Maloney, (Eds.), Perry's Chemical Engineering Handbook, 6th ed., McGraw-Hill, New York, 1984.
31 K.S. McGuire, *Membrane formation via liquid-liquid thermally induced phase separation*, Dissertation, The University of Texas at Austin, 1995.

32 EVALCA, *Technical Bulletin No. 100, Moisture absorption and drying of EVAL resins*, (2000) 4.

33 H. Yoshida, K. Tomizawa, and Y. Kobayashi, *Effect of annealing at temperatures around glass transition temperature on molecular orientation and shrinkage of ethylene-vinyl alcohol copolymers*, Journal of Applied Polymer Science, 24 (1979) 2277-2287.

34 M. Shang, H. Matsuyama, T. Maki, M. Teramoto, and D.R. Lloyd, *Preparation and characterization of poly(ethylene-co-vinyl alcohol) membranes via thermally induced liquid-liquid phase separation.*, Journal of Applied Polymer Science, 87 (2003) 853-860.

35 R.M. McDonogh, *unpublished results, cited by Beerlage*.

Chapter 4: Modeling uni-axial elongation of track-etch membranes [2]

4.1 INTRODUCTION

Microfiltration and ultrafiltration are used extensively in water treatment facilities and bioseparations [1]. A membrane's effectiveness in filtering depends on fouling, flux, and selectivity. These performance characteristics are heavily dependent on the membrane morphology. This chapter details modeling of an additional processing step that can be used to control membrane morphology along with the previous processing steps of matrix solidification and membrane drying.

Recent studies have shown that pore aspect ratio (defined as the ratio of major axis / minor axis) affects the fouling of membranes by changing cake growth patterns [2]. The right morphology and pore geometry could significantly reduce flux decline without sacrificing selectivity. Research in our laboratory has focused on systematically increasing the aspect ratio of pores by uni-axially stretching membranes. Worrel *et al.* [3] reported increased flux and decreased flux decline for stretched track-etched (TE) poly(ethylene teraphthalate) (PET) membranes. Morehouse, *et al.* [4] found similar flux performance benefits with phase inversion and phase separation poly(vinylidene fluoride) membranes. The focus of the research presented here is to model the changes in pore major and minor axes in TE membranes resulting from membrane elongation. Elongation is defined as percent change in length as shown in Equation 4.1:

$$\varepsilon = \frac{L_f - L_o}{L_o} \times 100 \quad \% \tag{4.1}$$

---

[2] The content of this chapter has been published as "Modeling of uni-axial stretching of track-etch membranes," Journal of Membrane Science, 305 (2007) 196-202.

where ε is elongation, L_f is the final length of the sample after stretching, and L_o is the initial length of the sample.

Stretching of microporous membranes to change the morphology has been reported in patent literature [5-15]. However, that literature does not state how pore size or pore size distributions change with stretching or provide insight into changes in membrane performance. Research in our laboratory attempts to address these issues.

TE membranes are expensive and difficult to make and thus are only made in specific pore sizes. Stretching could allow one to tailor a TE membrane to specific filtration needs.

The TE membranes reported here were kindly supplied by Whatman Corporation. These membranes are made by irradiating thin PET films with ion beams. The perforated film is then immersed in an alkali solution bath, which etches away the broken polymer chain ends. Pore size is controlled by the time the film spends in the etching bath. Longer residence times in the etching bath produce larger pores. This method of producing pores creates a narrow pore size distribution, making TE membranes ideal as size-selective separators and well suited to examining the effects of uni-axial stretching. Quantitative image analysis of TE membranes reveals a narrow pore size distribution; however, there is a wide range of angles that pores pass through the membrane. Image analysis also shows that overlapping pores occur, thereby causing some variation in surface pore size and producing some irregularly-shaped pore openings. While published reports indicate TE membranes can be made with pores of different shapes [16], the research presented here focuses on cylindrical pores as produced commercially by Whatman Corp.

Stretching TE membranes causes the pore major axis to elongate while the minor axis decreases slightly. Modeling this response can be useful in predicting final pore aspect ratio and subsequent sieving capability.

4.1.1 Void Growth Models

There are several mathematical models for predicting the change in shape of a void in elastic [17], plastic [18-23], elastic–plastic [24], and linear viscoelastic materials [25-29]. Hashin [25] studied the behavior of linearly viscoelastic heterogeneous material by employing the correspondence principle. Although his study is not specific to voids, he mentions that it can be extended to that case. Budiansky *et al*. [26] studied void growth in viscous solids. Mohan and Brust [27] extended this study to determine the effects of elasticity on void evolution in viscous solids, specifically metals that exhibit creep at high temperatures. Polymers exhibit creep behavior, which is significant in modeling the stretching process, but they also exhibit viscoelasticity, which metals do not. Li and Weng [29] studied the void growth of aligned spheroidal voids in linear viscoelastic materials. Their model of viscoelasticity was arrived at through a Laplace transform of the Eshelby-Moru-Tananka concept of elasticity. Li and Weng [28] extended their study to include composite materials in which inclusions are elastic but the matrix is viscoelastic or viscoplastic, but the case of voids was not discussed. Similarly, Wang and Weng [30] modeled self-similar void growth in linear viscoelastic material at moderate strains. They showed that the condition of self-similar growth depends on the viscoelastic model used. Clements [31] built on the work of Eshelby [17] and Weng [28-30] by finding an accurate analytical theory for viscoelastic deformation of soft polymers (above the glass transition temperature), which is an improvement on Weng's numerical solution. Clements' work showed that uni-axial deformation of aligned ellipsoidal voids rapidly increases aspect ratio, and more slowly increases void concentration. His work acknowledged the importance of non-linearity at high strains but did not account for these nonlinearities and did not predict deformations for elongations above 80%. Clements' work is also limited by not including a distribution of void sizes and by tracking the change of aspect ratio, rather than directly monitoring the changes in the major and minor axes. Steenbrink, *et al*. [32] studied void growth in a finite element unit cell model for a single sphere or cylinder in a visco-plastic material. Smit *et al*. [33] sought to stabilize the post yield response of polymers by studying the effects of both voids and inclusions. They found that the presence of both voids and inclusions causes the stress to spread out over the material and is successful in stabilizing the post-yield response. Worrel [34] used finite element methods to model the uni-axial deformation of perpendicular cylindrical pores, but was unable to account accurately for pore interactions. Morehouse *et al.* [4, 35] recently modeled phase inversion membranes with an idealized finite element beam model. The change in aspect ratio due to uni-axial stretching in the machine direction was modeled for elongations up to 80%. These models demonstrate that under uni-axial tension, circular pores change shape to elliptical, but they do not predict pore interaction for polymer membranes. The research reported here includes effects of pore interactions in TE polymer membranes in order to predict the change in pore geometry caused by uni-axial elongation. The membranes investigated in this research are those used by Worrel in her experimental work [3, 34].

4.2 MATERIALS AND METHODS

4.2.1 Materials

TE membranes made from PET were donated by Whatman Corporation in the form of 21.6 cm by 27.9 cm sheets. The membranes were reported by the manufacturer to be hydrophilic and had nominal pore sizes of 0.6, 2, and 10 µm and thicknesses varying from 13 µm to 23 µm. Measurements of pore sizes were made from SEM surface pictures and revealed average pore sizes of 0.61, 1.83, and 10.50 µm. Physical characteristics of the TE membranes are given in Table 4.1. Measurements of the angles from SEM cross-section images revealed a range from –41.7° to 56.7° and an average angle of 3.8° relative to perpendicular. Dense Mylar films of 23 µm thickness, made by DuPont and from which the membranes were made, were used to obtain physical material properties needed for modeling.

Table 4.1: Physical characteristics of the PET TE membranes.

Nominal reported pore size	Average pore size (µm)	Pore density (pores/cm^2)	Thickness (µm)
0.6 µm	0.61	3.91×10^7	22
2 µm	1.83	2.67×10^6	21
10 µm	10.50	1.37×10^5	13

4.2.2 Experimental Procedures

A T.M. Long stretching device (supported by Inventure Labs, www.inventurelabs.com) donated by the 3M Company was used to stretch the Mylar films at elevated temperatures to obtain the physical properties (stress–strain relationship and relaxation due to viscoelasticity). An electric stepper motor provided linear control in the stretching direction with a minimum and maximum stretching velocity of 0.05 and 6.0 cm/s. The stretching device was heated by two electric heating plates that have a maximum operating temperature of 200°C. A pneumatic gripping system pressurized to 300 – 500 psig held the membrane coupon in the stretching direction; the transverse direction is not restrained. The coupons were 12.7 cm long in the direction of stretch and 7.5 cm in the transverse direction. The direction of stretch was in the machine direction, which can be determined from the angles of the pores. The edges of the coupons were mounted on a rigid metal support beam 0.5 cm in width and 10 cm in length using poly(propylene) tape (3M Scotch 3750). The beam provided stability in mounting and ensured that the coupon was flat and even when pulled taut. The device was heated to the desired stretching temperature of 160°C and held for 30 minutes to ensure the desired temperature had been obtained. After elongation of the coupon at a rate of 1cm/s, it was annealed for 15 minutes at the elongation temperature before air cooling under the remaining tension. The sample was removed when cool and measured with a ruler to 0.5 mm to determine the actual strain achieved. Samples from the center of each stretched membrane were cut out, sputter-coated with gold, and imaged in a Hitachi S4500 SEM. The surface images were then loaded into ImagePro software to measure the major and minor axes.

The stress–strain relationship used in the modeling was determined by stretching the Mylar films at 160°C and at a rate of 1 cm/s in the direction the films were extruded. Stress was calculated by monitoring the force with a load cell while the film was stretched via Labview software. Viscoelastic properties were determined using small strain relaxation tests at various temperatures ranging from 80°C to 170°C.

Non-stretched pore characteristics were measured from SEM pictures to be used in constructing models and as a control. Surface images for major and minor axes sizes of non-stretched membranes were obtained as described above. Non-stretched 2 μm membranes were freeze fractured with liquid nitrogen to obtain a cross-section that was imaged in an SEM. The pore angle distribution was measured from the cross-sections using ImagePro software, which was also used to measure the major and minor axes on the surface images. An example of the 2 μm SEM images is shown in Figure 4.1.

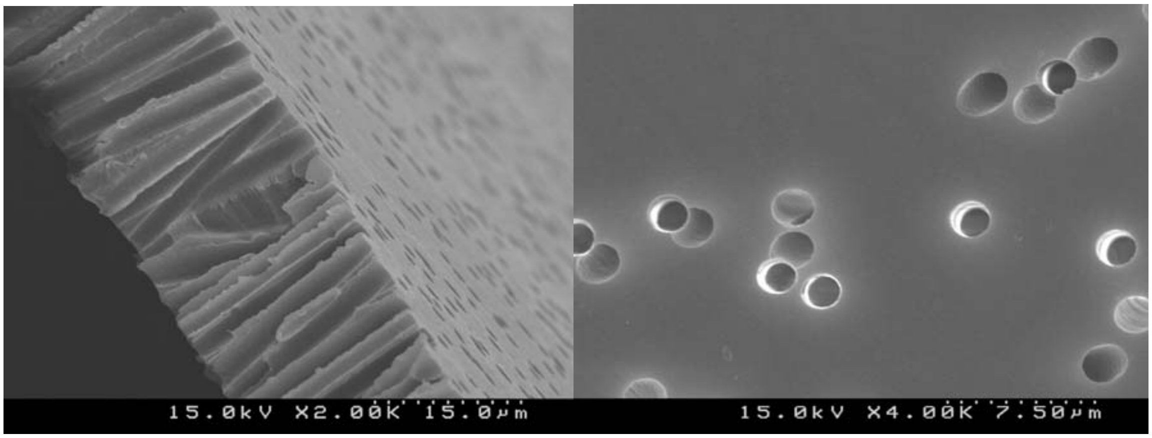

Figure 4.1: Cross-sectional and top view of 2 μm TE PET

4.2.3 Modeling

A 3D model of the 2 μm PET membrane was developed in AutoCAD using actual measured values of pore density, minor axis length, pore angle, and membrane thickness. The pore locations were chosen by randomly generating *x* and *y* coordinates within a specified surface area. Cylinders traversing the membrane were generated at these locations and their diameters were chosen by selecting from a large set of measured minor axes whose distribution is shown in Figure 4.2a. The cylinder was tilted at an angle chosen from the distribution of the angles measured, which is shown in Figure 4.2b. Pore angles and the membrane stretch occurred in the same direction (the direction of extrusion) in both the model and the experiment. The volume of the angled cylinder is removed from the modeled film to yield the model membrane. For each pore size, a minimum of three model films were created from the respective distributions. The objects developed in AutoCAD were then imported into ABAQUS CAE.

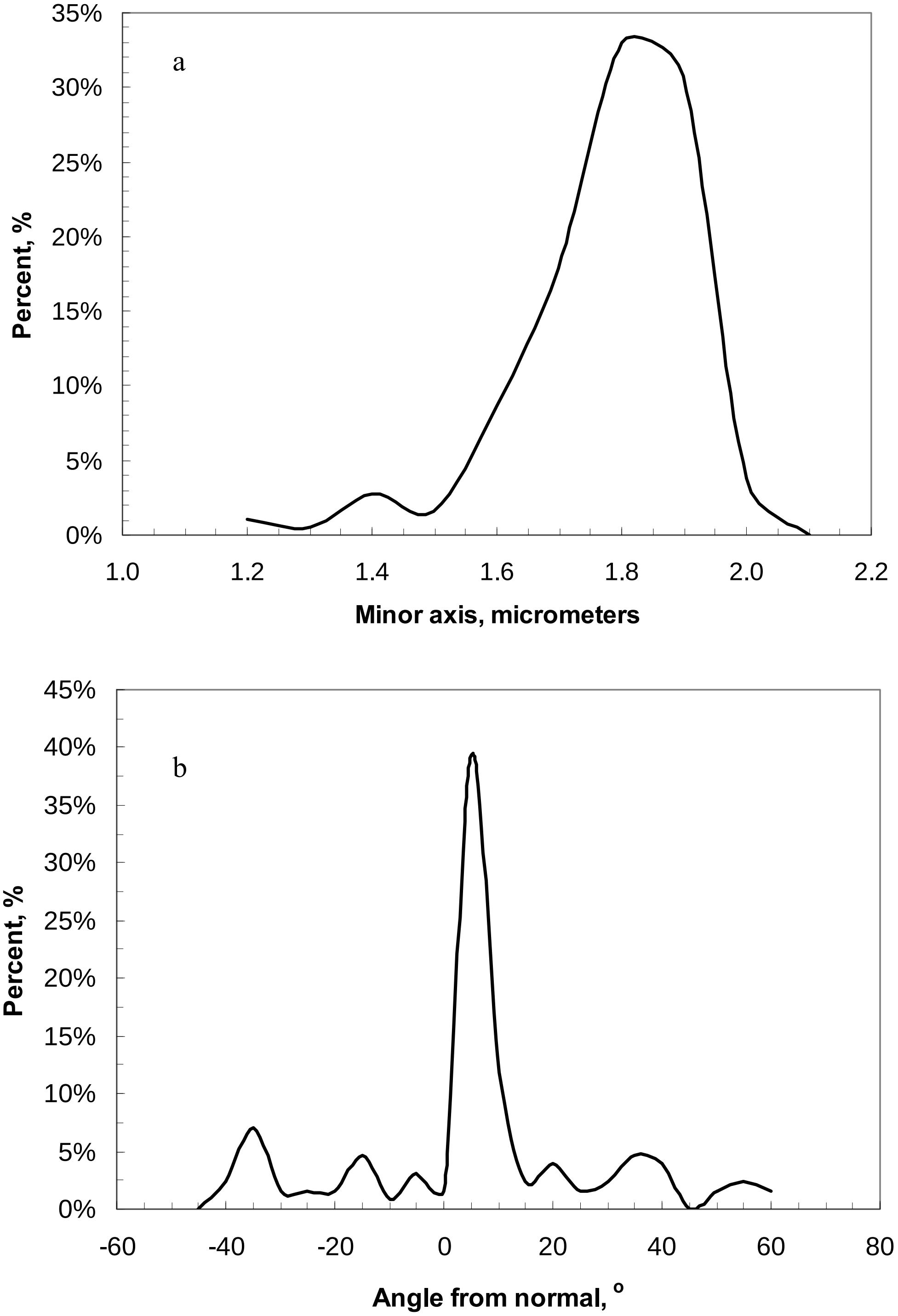

Figure 4.2: The experimentally measured minor axis (a) and angle from normal (b) distributions for the pores of the 2 μm PET membranes.

ABAQUS has the ability to use implicit or explicit solution procedures, along with static, dynamic, and non-linear analysis, allowing it to model a variety of structural mechanics problems. ABAQUS also has many material models that have proven successful in modeling the behaviors of glassy and rubbery polymers [34-37]. In this case, PET was modeled with the Marlow model or the Neo-Hookean hyperelastic models fit to the experimentally determined stress–strain curve in Figure 4.3. The equations for the Neo-Hookean hyperelastic model and the Prony series model of relaxation due to viscoelasticity are given in Chapter 3 as Equation 3.1 and 3.2, respectively. The coefficients of the material properties are given in Table 4.2.

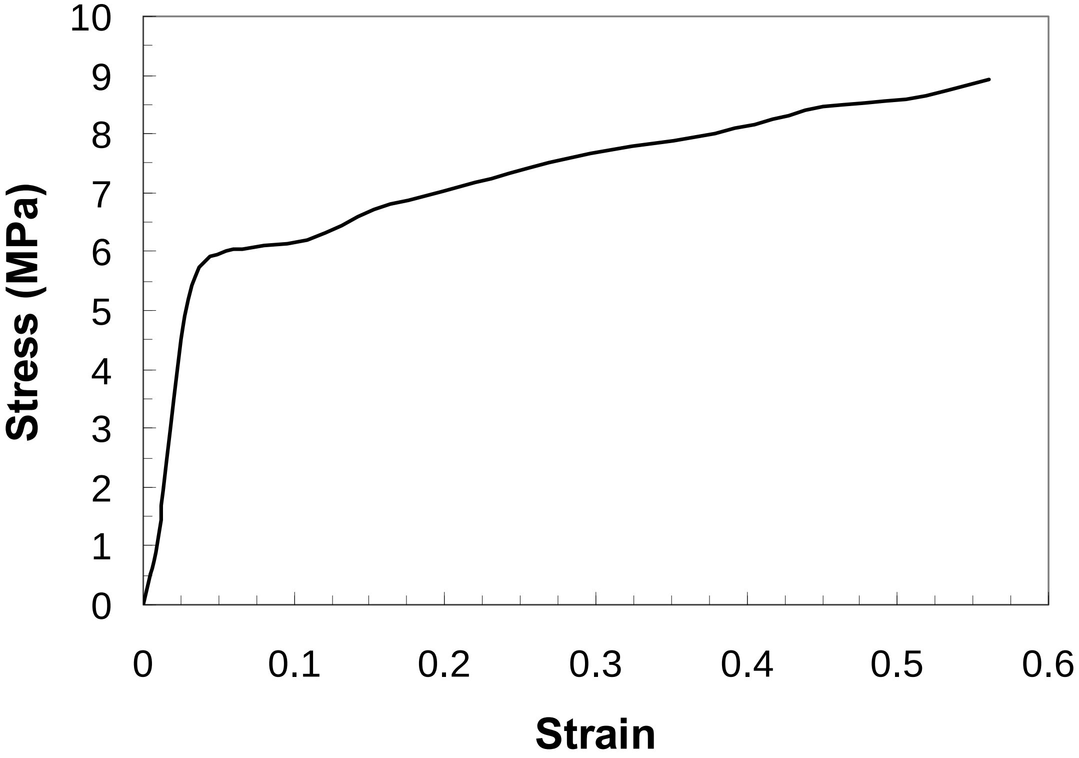

Figure 4.3: The experimentally determined stress–strain response curve of the dense PET film.

Table 4.2: Material properties of PET

Neo-Hookean Model (for 160°C)	
D_1	C_{10}
0.00	5.5053
Prony Series	
τ_i	p_i
1.0×10^{-5}	0.0402
1.0×10^{-4}	0.0468
1.0×10^{-3}	0.0572
1.0×10^{-2}	0.1805
1.0×10^{-1}	0.0487
1.0×10^{0}	0.0988
1.0×10^{1}	0.0205
1.0×10^{2}	0.1394
1.0×10^{3}	0.0000
1.0×10^{4}	0.1283
1.0×10^{5}	0.0470
1.0×10^{6}	0.1005

The 3D structure imported from AutoCAD was meshed independently with continuum 10 node modified quadratic tetrahedrals with hybrid linear pressure control (C3D10MH) elements. A discussion of this mesh type can be found in section 3.2.2.

The elongation of TE membranes was simulated as four distinct steps: stretching the membrane to a defined strain, annealing the membrane at the temperature of stretching, cooling the membrane, and releasing the restraining boundary conditions once the membrane is cooled. The computer code to model the elongation is listed in Appendix B.

The stretching step was simulated in ABAQUS by first stretching the membrane at 160°C with non-linear static analysis (ABAQUS STANDARD) where the equilibrium equations are solved on the deformed geometry. The subsequent simulation steps were modeled using transient–static solution methods with time-dependent material responses.

The second modeling step consisted of annealing the elongated model membrane for 15 minutes at 160°C, where stress redistribution and dissipation occurred.

After annealing, the model was cooled to 35°C by specifying utilizing temperature boundary conditions. Once at 35°C, the restraining boundary conditions were released and the membrane was allowed to rebound. Five minutes were allocated to allow the membrane to rebound fully, although the final shape was normally achieved within seconds of removal of the restraining boundary condition.

Displacement control was utilized to apply the strain, with one side of the membrane in the stretching direction held encastre, where all six degrees of freedom are restricted. The stretching step utilized hyperelastic properties to calculate stresses and displacements while the annealing and release steps used the viscoelastic properties to calculate relaxation and rebound. These conditions were similar to the experimental stretching conditions mentioned in the experimental procedures section. Worrel [34] concluded that the thickness of the dense films and TE membranes did not significantly change over the range of conditions studied and the behavior of Mylar films was strain rate independent over strain rates up to 6 cm/s, allowing for the elongation to be modeled with a static analysis.

Additionally, 2D constructs were created from the top and bottom faces of the 3D models and stretched using the same physical properties, stretching conditions, and solution routines. These models were implemented in the same way as the 3D models, except CPS8R (continuum, plane stress, 8 node, reduced integration) elements were used to mesh the structure. The 2D models were scaled up to contain 64 pores, as seen in Figure 4.4, since this size has been shown to be a good computational unit cell to model composite behavior [38]. A minimum of two different models for each pore size (0.6, 2, and 10 μm) were created for the simulations.

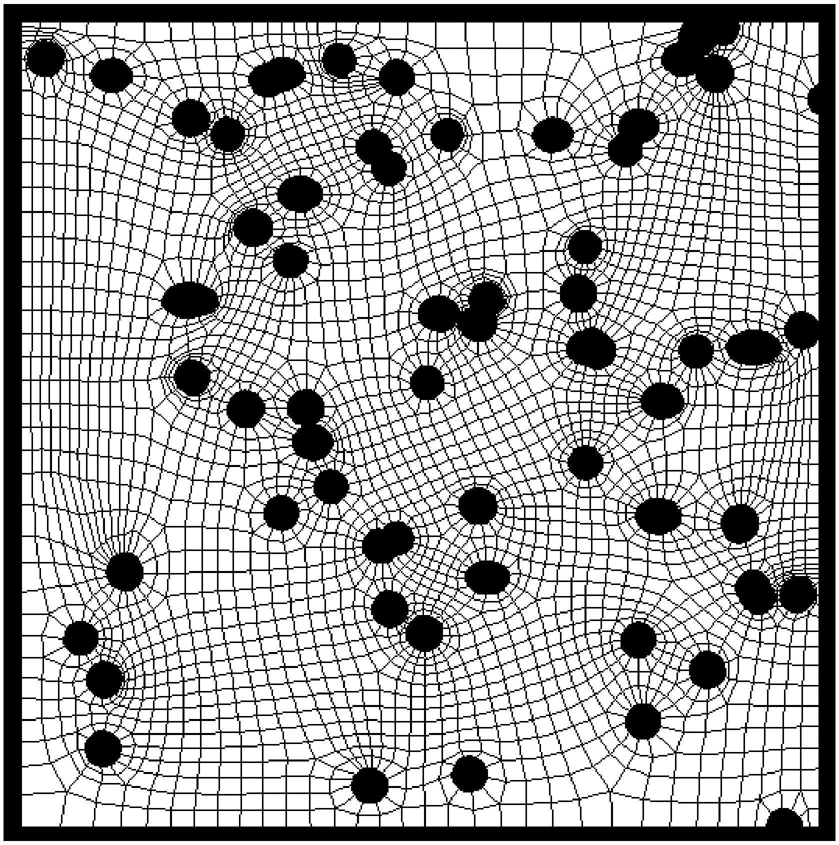

Figure 4.4: A sample 2D model of the TE membranes containing 64 pores.

Elongations up to 45% were modeled in ABAQUS, and the final pore dimensions were measured and averaged. These results were compared to the experimental measurements to determine the accuracy of the model.

When measuring the pore sizes in the models and the SEM images, overlapping pores were not considered because major and minor axes are not defined for such irregular shapes. Pores near the edge of the membrane held encastre were not considered because of the distortion caused by necking. This made the measurements consistent with the SEM images, which were taken from the middle of the membrane where little necking occurred.

4.3 RESULTS AND DISCUSSION

The porous membrane material is modeled based upon properties of the dense polymer film. The Marlow model of hyperelasticity is stable at all strains studied and generates a stress–strain response indistinguishable from PET dense film experimental data. The Neo-Hookean model is also stable at all strains studied and is a simplified hyperelastic model. The Neo-Hookean model resulted in a different stress distribution in the porous films prior to annealing; however, the difference in pore sizes for the same simulated membrane predicted by the Marlow and the Neo-Hookean models was less than 5%. In all of the stretches, the local strains in the porous membranes did not exceed the maximum dense film strain used to generate the material parameters.

The deformation of a simulated material can be dependant on the mesh size used if the mesh size is too small. A mesh with a seed size of 2.5 was found to be sufficient for the modeling of the 2 and 10 µm membranes, while the membranes with a nominal reported diameter of 0.6 µm used a seed size of 0.65. Figure 4.4 shows a mesh resulting from a 2.5 seed size for a 10 µm membrane. Figure 4.5 shows that the geometry of the deformed pores is rather insensitive to the mesh density for the range studied. No significant information was gained by using a tighter mesh, and while loose meshes are computationally quicker the stress distribution in the sample is more uneven. The bulk stress within the membrane correlated well to experimental results during the uni-axial elongation step, but the stresses decreased during the annealing step much faster in the simulation than experimentally. This has little impact on the geometry of the pores due to the long duration of annealing and as the rebound of the film, approximately 3%, is comparable in simulation and experimentally. The small amount of rebound and long experimental annealing time could allow for ignoring the viscoelastic responses associated with these steps, but are included to demonstrate the general applicability and usefulness of the simulation method.

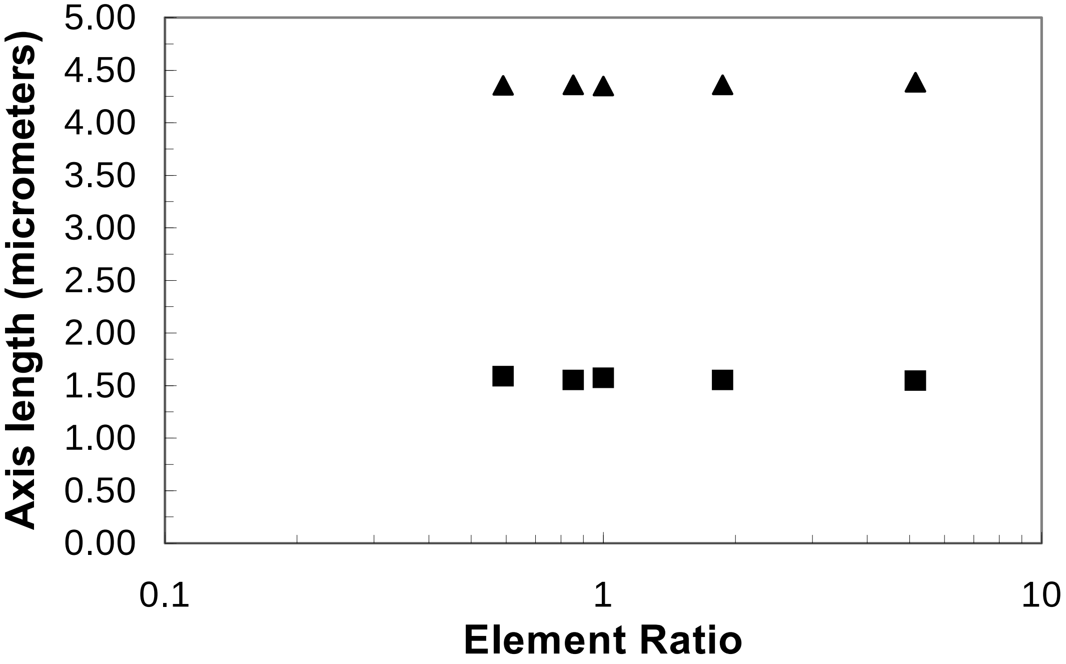

Figure 4.5: The sensitivity of the major and minor axes with regard to the number of elements used in the finite element mesh.

Figure 4.6 compares the results from the 8-pore 3D and 2D models. The two data sets are almost indistinguishable. Pore sizes were compared at 50% stretch and the difference between the 3D and 2D measurements was found to differ by no more than 6%. Upwards of 48 hours on a workstation equipped with 4 GB of RAM and two 3.2 GHz processors were required for ABAQUS to calculate results for one 8-pore 3D model, whereas only 5–10 minutes were needed for each 64-pore 2D model. Consequently, the 2D model was preferable to the 3D model because it yielded nearly equivalent results with much less computation time.

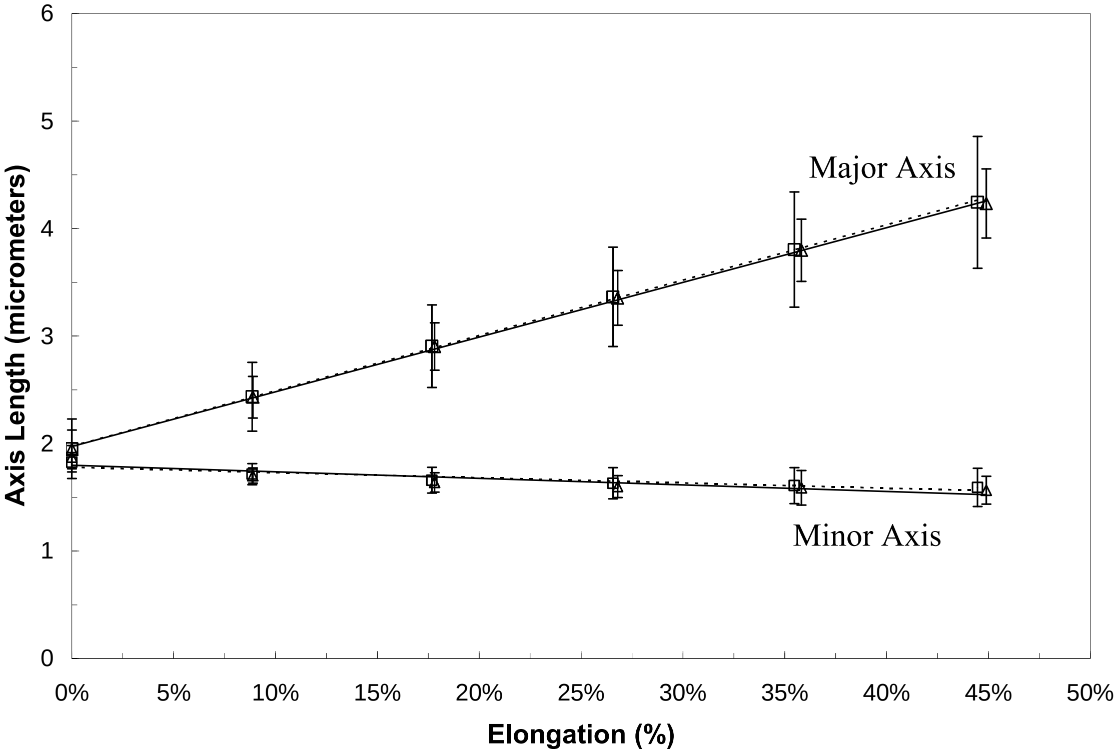

Figure 4.6: Comparison of 3D and 2D results for 8-pore 2 μm model: (□,--) 2D Model; (Δ, −) 3D Model

Figures 4.7 to 4.9 compare the experimental and model results for membranes with a nominal reported pore size of 2, 10, and 0.6 μm, respectively. The data shows fairly strong linear correlation between elongation and major axis length. The minor axis shows a negative linear correlation with elongation, but it is not as strong as that for the major axis. The fit of the 0.6 μm model was not quite as good as the 2 μm and 10 μm models because 0.6 μm membranes have higher porosity and pore density, making the pore interactions more pronounced and harder to predict in 2D. Generally, as the porosity and pore density decrease (pore size increases), the membrane bulk properties more closely resemble the Mylar film, so ABAQUS is better able to predict the deformations. This is why the 10 μm model had the best fit whereas the 0.6 μm model had the poorest fit.

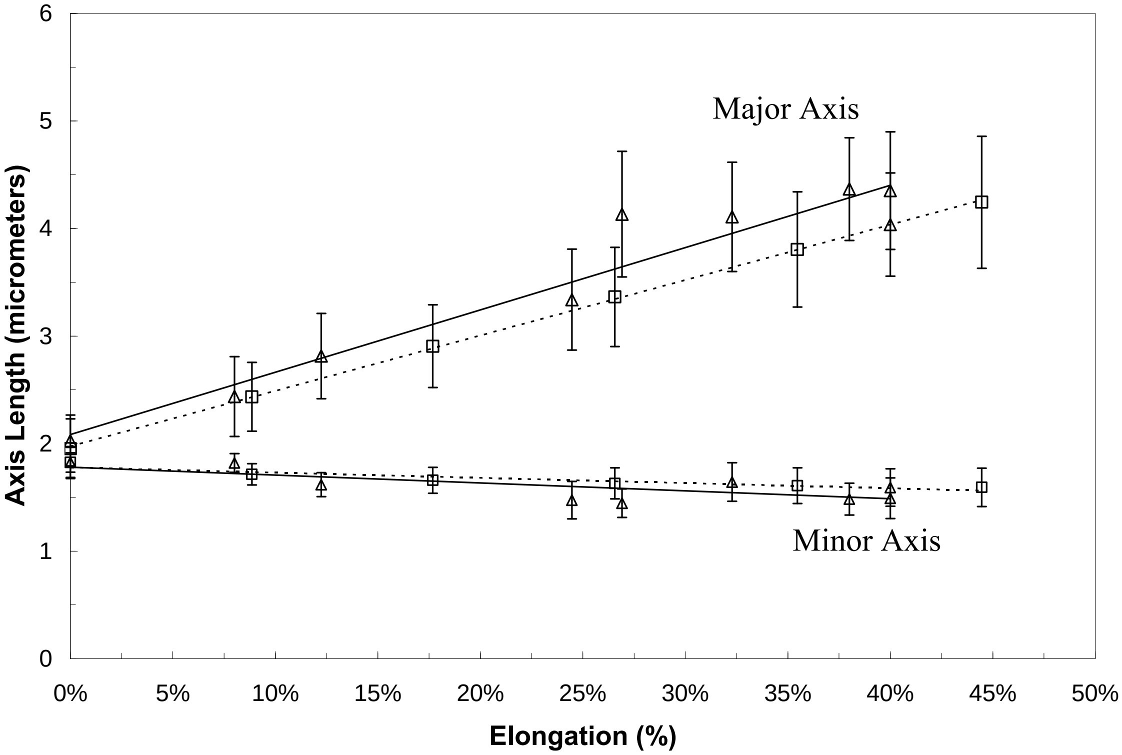

Figure 4.7: Comparison of 2D model and experimental results for the membrane with a nominal reported pore diameter of 2 μm: (□,--) 2D Model; (Δ, −) Experimental

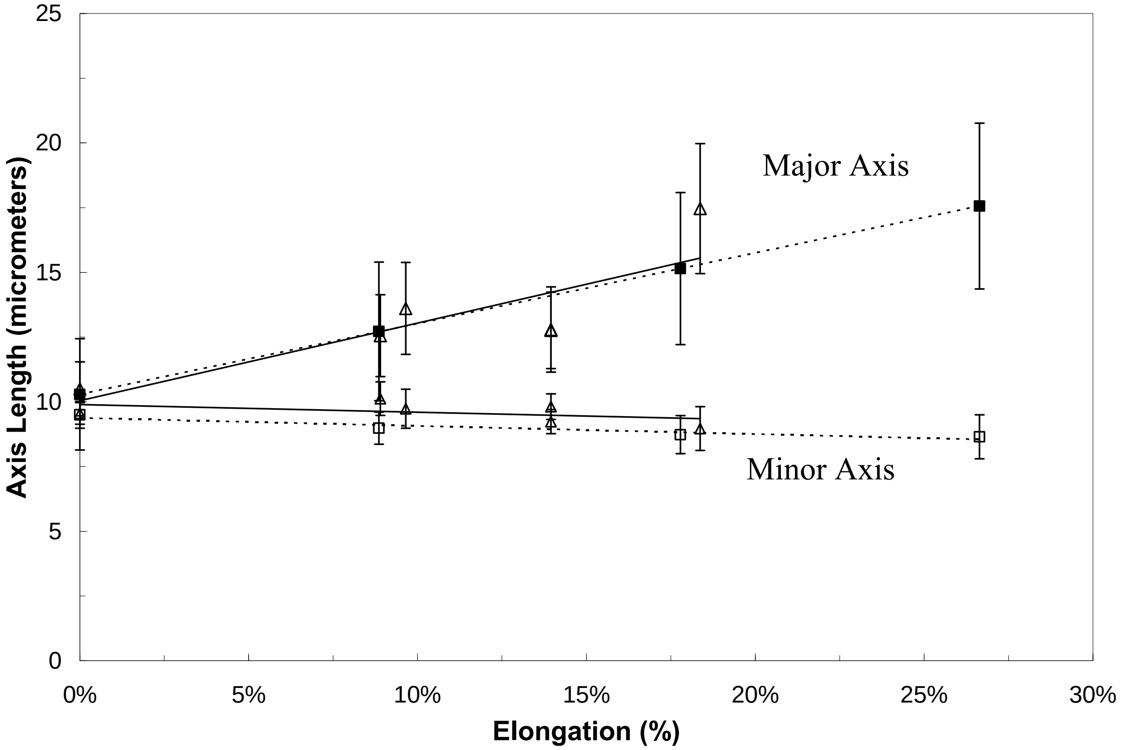

Figure 4.8: Comparison of 2D model and experimental results for the membrane with a nominal reported pore diameter of 10 µm: (□, --) 2D Model; (Δ, −) Experimental

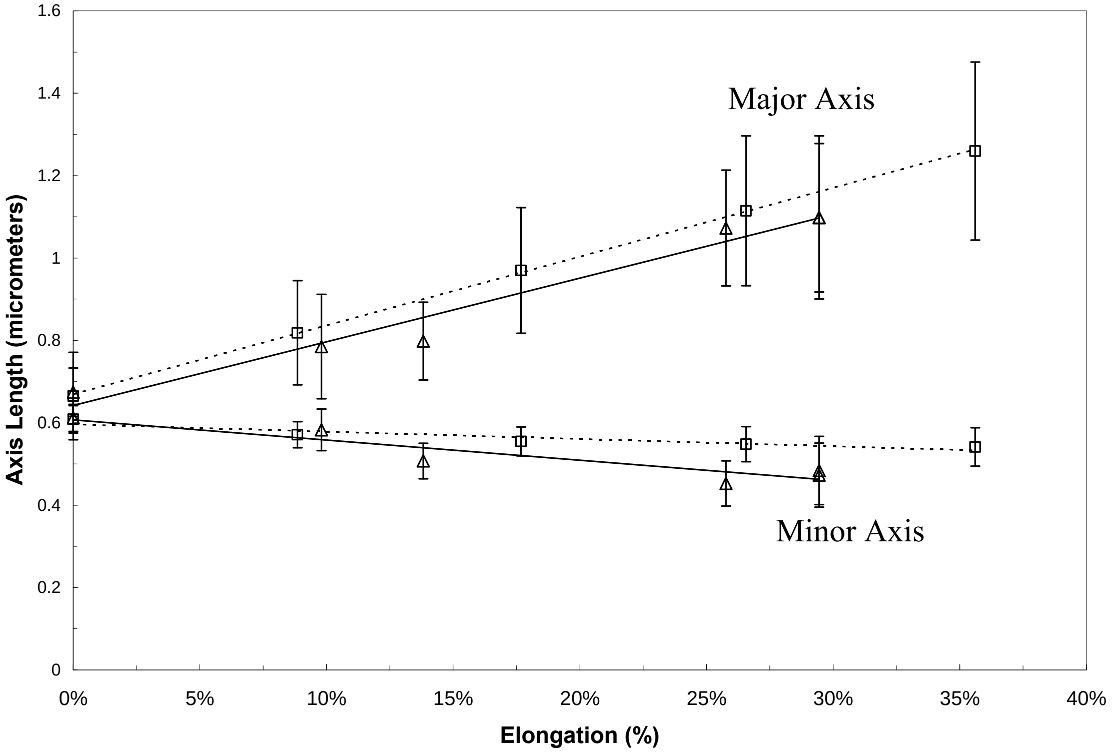

Figure 4.9: Comparison of 2D model and experimental results for the membrane with a nominal reported pore diameter of 0.6 μm: (□, --) 2D Model; (Δ, −) Experimental

Although there were minor discrepancies between the model and experimental results, the model fits well enough to be used as a predictive tool. Most of the differences between the model and experimental results were merely translations of the trendlines; however, it is apparent that the *change* in axis length with elongation, as indicated by the slope, is very similar. The means to predict the change in axis lengths leads to the ability to predict the separation capability of the new membranes through methods similar to that of Starov *et al.* [39], as presented in Chapter 5.

4.4 CONCLUSION

Finite element modeling adequately predicts morphological changes to the pore structure of TE membranes caused by uni-axial stretching. While only shown for PET membranes, these same techniques should also describe morphological changes in other polymer TE membranes capable of deformation. 3D modeling provides results, including interior morphological changes, but only after long computation times. 2D modeling provides accurate predictions of surface morphology changes after a few minutes. This tradeoff is acceptable as the majority of the separation occurs on the surface of the TE membranes. The modeling of the separation using uni-axially elongated membranes in a dead-end microfiltration is presented in Chapter 5.

4.5 REFERENCES

1 K.K. Sirkar and W.S. Ho, (Eds.), Membrane Handbook, 1st ed., van Nostrand Reinhold, New York, 1992.

2 M. Chandler and A. Zydney, *Effects of membrane pore geometry on fouling behavior during yeast cell microfiltration*, Journal of Membrane Science, 285 (2006) 334-342.

3 L.S. Worrel, L.A. Shimko, J.A. Morehouse, D. R. Lloyd, B.D. Freeman, and D.F. Lawler, *Enhancement of Track-etched Membrane Performance via Stretching*, Separation and Purifications Technology, 53 (2007) 71-80.

4 J. Morehouse, *The effect of uni-axial stretching on microporous phase-separation membrane structure and performance*, Dissertation, University of Texas at Austin, 2006.

5 G.H. Shipman, *Microporous sheet material method of making and articles made therewith*, US Patent 4,539,256, 1985.

6 K.E. Kinzer, *Oriented microporous films*, US Patent 4,867,881, 1989.

7 K.E. Kinzer, *Method for preparing oriented microporous film*, US Patent 5,238,619, 1993.

8 J.S. Mrozinski, *Microporous materials incorporating a nucleating agent and methods for making same*, US Patent 4,726,989, 1988.

9 J.S. Mrozinski, *Multi-layer laminates of microporous film*, US Patent 4,863,792, 1989.

10 J.S. Mrozinski, *Method for preparing microporous polyolefin shaped articles*, US Patent 5,238,623, 1993.

11 P.W. Clinnton, *Microporous materials of ethylene-vinyl alcohol copolymer and method of making same*, US Patent 5,962,544, 1997.
12 S.B. McCray, D.T. Friesen, D.R. Sidwell, D.K. Lyon, and D. Sakashita, *Ethylene-vinyl alcohol hollow fiber membranes*, USA Patent 6,793,820, 2001.
13 K. Takita, K. Kono, T. Takashima, and K. Okamoto, *The preparation method for microporous polyolefin membrane*, Japan Patent 364,334, 1991.
14 K. Takita, K. Kono, T. Takashima, and K. Okamoto, *Microporous polyolefin membrane and method of producing same*, US Patent 5,051,183, 1991.
15 P. Jacoby, C.W. Bauer, S.R. Clingman, and W.T. Tall, *Oriented polymeric microporous films*, USA Patent 5,317,035, 1992.
16 P. Apel, *Track etching technique in membrane technology*, Radiation Measurements, 34 (2001) 559-566.
17 J.D. Eshelby, *The determination of the elastic field of an ellipsoidal inclusion, and related problems*, Proceedings of the Royal Society (London), A241 (1957) 376-396.
18 F.A. McClintock, *A Criterion for Ductile Fracture by the Growth of Holes*, Journal of Applied Mechanics (1968) 363-371.
19 J.R. Rice, D.M. Tracey, *On the ductile enlargement of voids in triaxial stress fields*, Journal of the Mechanics and Physics of Science, 17 (1969) 201-217.
20 Tracey, *Strain-Hardening and Interaction Effects on the Growth of Voids in Ductile Fracture*, Engineering Fracture Mechanics, 3 (1971) 301-315.
21 A.L. Gurson, *Continuum theory of ductile rupture by void nucleation and growth: Part 1. Yield criteria and flow rules for porous media.*, Journal of Engineering Materials and Technology, Transactions of the ASME, 99 (1977) 2-15.
22 V. Tvergaard, *Influence of voids on shear band instabilities under plane strain conditions.*, International Journal of Fracture, 17 (1981) 389-407.
23 V. Tvergaard, *On localization in ductile materials containing spherical voids*, International Journal of Fracture, 18 (1982) 237-252.
24 A. Needleman, *Void growth in an elastic-plastic medium*, Transaction of Journal of Applied Mechanics (1972) 964-970.
25 Z. Hashin, *Viscoelastic Behavior of Heterogeneous Media*, Journal of Applied Mechanics, 32 (1965) 630-636.
26 B. Budiansky, J.W. Hutchinson, S. Slutsky, *Void Growth and Collapse in Viscous Solids*), Mechanics of Solids, Pergamon Press, Oxford, 1982, pp. 13-45.
27 R. Mohan and F.W. Brust, *On Void Growth in Elastic-Nonlinear Viscous Solids Under Creep and cyclic creep conditions*, Journal of Engineering Materials and Technology, 122 (2000) 283-293.
28 J. Li and G.J. Weng, *A unified approach from elasticity to viscoelasticity to viscoplasticity of particle reinforced solids*, International Journal of Plasticity, 14 (1998) 293-208.
29 J. Li and G.J. Weng, *Void growth in viscoelastic polymeric materials*, Mechanics of Plastics and Plastic Composites, ASME 1995, 68 (1995) 409-421.
30 Y.M. Wang and G.J. Weng, *Self-Similar and transient void growth in viscoelastic media at low concentrations*, International Journal of Fracture, 61 (1993) 1-16.

31 B.E. Clements, *Damage Evolution in Viscoelastic Polymers*, AIP Conference Proceedings, 505 (1999) 527-530.

32 A.C. Steenbrink, E. Van Der Giessen, P.D. Wu, *Studies of the Growth of voids in amorphous glassy polymers*, Journal of materials science, 33 (1998) 3163-3175.

33 R.J.M. Smit, W.A.M. Brekelmans, H.E.H. Meijer, *Predictive Modelling of the properties and toughness of polymeric materials: Part III: Macrostructural Deformation of rubber modified polymers*, Journal of materials science, 35 (2000) 2881-2892.

34 L.S. Worrel, *Modification of Track-Etched Membrane Structure and Performance via Uniaxial Stretching*, Dissertation, The University of Texas at Austin, 2005.

35 J.A. Morehouse, D.R. Lloyd, B.D. Freeman, D.F. Lawler, K.M. Liechti, and E.B. Becker, *Modeling the stretching of microporous membranes*, Journal of Membrane Science, 283 (2006) 430-439.

36 J. Sweeney, P. Caton-Rose, P.D. Coates, *The modeling of large deformations of pre-oriented polyethylene*, Polymer, 43 (2001) 899-907.

37 J.D. Wu and K.M. Liechti, *Multiaxial and Time Dependent Behavior of a Filled Rubber*, Mechanics of Time-Dependent Materials (2000) 293-331.

38 A. Gusev, *Representative volume element size for elastic composites: a numerical study*, J. Mech. Phys. Solids, 45 (1997) 1449-1459.

39 V.M. Starov, D.R. Lloyd, and A.M. Filippov, *Interaction of charged colloid particles with charged membranes*, Advances in Filtration and Separation Technology, 7 (1993) 446-450.

Chapter 5: Performance Effects of Pore Shape Change

5.1 INTRODUCTION

The previous chapter describes the modeling of a simple process of uni-axial elongation that can change the pore shape of track-etch (TE) membranes from circular to elliptical. The motivation behind attempting such a pore shape change is that recent studies have shown that changing the pore aspect ratio affects the fouling of a membrane by changing cake growth patterns [1]. Recent literature has also shown increased flux and decreased flux decline for stretched TE poly(ethylene teraphthalate) PET membranes [2] and some phase inversion membranes [3]. As the model developed in the previous chapter tracks the change in membrane morphology as a function of strain, it is now possible to develop simulations showing the effects of pore shape change on performance.

Various performance models of membranes have been developed including, but not limited to: pore blockage and cake formation with internal fouling in microfiltration [4], cake formation in ultrafiltration [5], and a sieve mechanism of microfiltration (MF) [6, 7]. The sieve mechanism of filtration was first introduced more than two decades ago [8] and has been continually advanced to include more difficult transport phenomena [9-11]. The sieve mechanism of filtration is of particular relevance for low concentrations of particulate matter such as high purity water for microelectronics [12] and lab scale filtrations, for which TE membranes are well suited. The sieve filtration model describes the process shown in Figure 5.1.

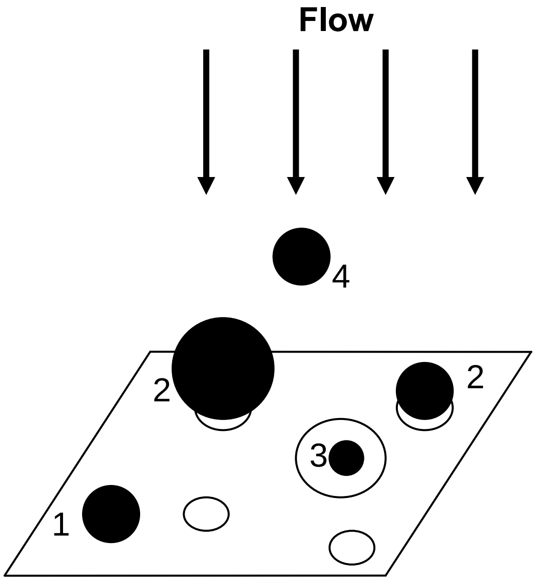

Figure 5.1: Schematic presentation of the MF sieving process: (1) particle adheres to the surface; (2) particle blocks a small pore; (3) a small particle passes through a large pore; (4) a particle approaching the surface that may or may not block a pore.

5.1.1 Basic Sieve Mechanism Model for Circular pores

The sieve mechanism for filtration is based on statistics and the assumption of dead end filtration using a microfiltration (MF) membrane. The assumption of a MF membrane, as opposed to an ultrafiltration membrane, allows for simplification of the transport process. Estimating the diffusion coefficient of a spherical particle on the order of one micron yields a result of around 10^{-9} cm^2/s. The actual diffusion coefficient will be less than that because of the decrease in the particle's hydrodynamic mobility near the surface [13-15]. For slow velocities and a Peclet number much greater than one, particle diffusion and concentration polarization can be neglected and are not considered in the sieving model. For simplicity, the basic model adapted here also does not include any electrodynamic attraction between the particles and the membrane. Additionally, neither model takes into account the excluded volume along the pore walls. The derivation below is based on previous studies conducted in our laboratory and elsewhere [7, 11].

With the above assumptions, the probability that an individual pore of diameter d will not be blocked at a given time is:

$$P\left(d,\bar{t}\right)=\left(1-\pi\beta\, l^2d^2 \big/ 4S\right)^{n\left(d,\bar{t}\right)} \tag{5.1}$$

where $\bar{t}$ is time, β is a parameter used to characterize the pore's influence, S is the surface area of the membrane, and $n(d,\bar{t})$ is the number of particles with a diameter greater than the pore. The use of β allows incorporation of area beyond the circumference of the pore. Particles in the vertical column above the additional area around the pore will be forced to move towards the pore entrance by the streamlines of the fluid flow, as seen in Figure 5.2. Calculating β is beyond the scope of the present work as it requires solving the hydrodynamic equation taking into account local interactions in the vicinity of the membrane pores. Additionally, calculating β is not necessary as a non-dimensionalization process described below eliminates β from the equations. $n(d,\bar{t})$ requires the concentration, c, of particles with diameter (D) larger than pore diameter d, which is given by:

$$c_d = c\int_{d}^{D_{\max}} f_p(D)dD \tag{5.2}$$

where $f_p(D)$ is the particle size distribution function. As diffusive flux is much less than convective flux, the flux of particles is related to the volume of fluid passed through the membrane. Utilizing the integral of fluid flux from the initial time to the current time over a section of the membrane surface yields an expression for $n(d,\bar{t})$:

$$n\left(d,\bar{t}\right)=cS\int_0^{\bar{t}} J(u)du\int_{d}^{D_{\max}} f_p(D)dD \tag{5.3}$$

Since the area of a single pore is much less than the surface area of the membrane ($\pi l^2 d^2/4 << S$) and the number of particles approaching the membrane surface, $n(d, \bar{t})$, is much greater than one, Equations 5.1 and 5.3 can be combined to form a simplified expression:

$$P\left(d,\bar{t}\right) = \exp\left[-\left(\pi\beta\, l^2 d^2 c/4\right)\int_0^{\bar{t}} J(u)du \int_d^{D_{\max}} f_p(D)dD\right] \qquad (5.4)$$

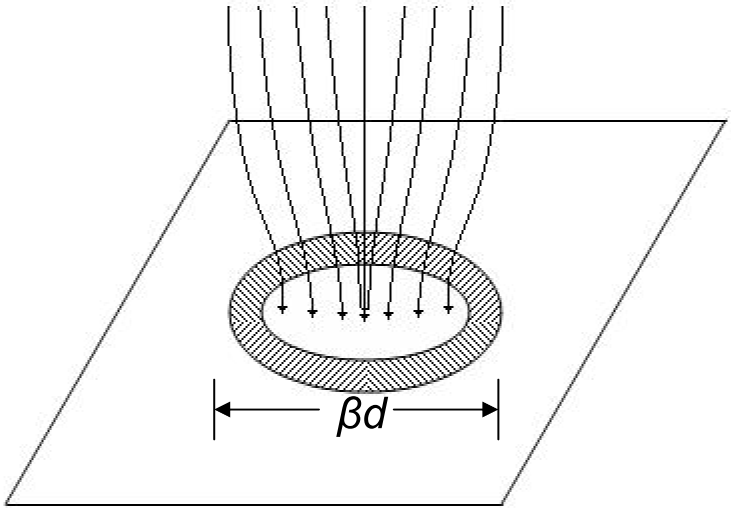

Figure 5.2: A graphical representation of β for a single circular pore. The hatched region increases the nominal pore area because of the streamlines of fluid flow.

Now that it can be determined whether a pore will be blocked at a given time, it is possible to investigate the flux decline over time for a given membrane. As a slow velocity in dead-end MF was assumed earlier, it is further assumed that the flow through a single pore is described by Poiseuille flow:

$$Q(d) = \frac{\pi\, l^4 d^4 \Delta p}{128\, \mu L} \qquad (5.5)$$

where Δp is the pressure drop across the membrane, μ is the fluid viscosity, and L is the length of the membrane pore (assumed to be the thickness of the membrane for TE membranes). Averaging the local flows to provide a volumetric flow for the entire membrane gives an initial flux at $\bar{t} = 0$ of:

$$J_0 = \frac{\pi N_m l^4 \Delta p}{128\,\mu L S A} \tag{5.6}$$

where N_m is the number of pores and A is defined as:

$$A = \left[\int_{d_{\min}}^{d_{\max}} x^4 f_m(x)\,dx\right]^{-1} \tag{5.7}$$

It follows that the flux through the membrane at time $\bar{t}$, taking into account pore blocking, is:

$$J\left(\bar{t}\right) = J_0 A \int_{d_{\min}}^{d_{\max}} x^4 f_m(x) P\left(x, \bar{t}\right) dx \tag{5.8a}$$

which is equivalent to:

$$J\left(\bar{t}\right) = J_0 A \int_{d_{\min}}^{d_{\max}} x^4 f_m(x) \exp\left[-\left(\frac{\pi\beta l^2 c}{4}\right) x^2 \int_{x}^{D_{\max}} f_p(D)\,dD \int_0^{\bar{t}} J(u)\,du\right] dx \tag{5.8b}$$

Equations 5.8a and 5.8b simplify for extreme cases, such as no pore blocking ($D_{max} < d_{min}$) to yield $J(\bar{t}) = J_0$, indicating the flux will always be the initial flux because there is no fouling. It can also be seen that for $D_{min} > d_{max}$ that $J(\bar{t})$ at long times will be zero, indicating that the membrane is completely fouled. As useful as the above equations prove to be, a number of parameters for the membrane and for the flow conditions must be known. It is possible to non-dimensionalize the equations to allow for solving a general case and merely shifting the flux-decline curve depending on variables such as pressure drop, particle concentration, etc. Using a dimensionless flux of $j = J/J_0$, and a dimensionless time where $t = \bar{t}\ (4/\beta\pi l^2 c J_0)$ allows Equation 5.8b to be rewritten:

$$j(t) = A \int_{d_{\min}}^{d_{\max}} x^4 f_m(x) \exp\left[-x^2 \int_0^{t} j(\zeta)\,d\zeta \int_{x}^{D_{\max}} f_p(D)\,dD\right] dx \tag{5.9}$$

Equation 5.9 can be solved analytically in the case of idealized TE membranes where all pores have the same diameter − $f_m(d)$ is a delta function. However, TE membranes do have distributions in the pore sizes as shown in Chapter 4. In this case, Equations 5.7 and 5.9 can be solved numerically in Matlab using Simpon's rule for integration.

5.2 MODELING METHODS

5.2.1 Modified Sieve Mechanism for Elliptical pores

The previous section outlined the basic form of sieve filtration that is adapted for elliptical pores in this section. The same assumptions apply, namely: spherical particles, particles are transported by convection, and Poiseuille flow occurs in the pores. In the case of elliptical pores, the minor axis determines whether a particle will pass through the membrane or will be retained on the surface. Additionally, a particle is not able to block completely a pore as there will always be some area for fluid to pass through, as seen in Figure 5.3.

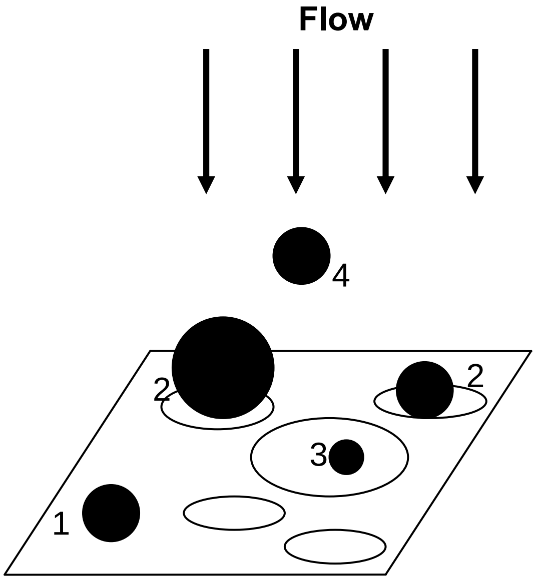

Figure 5.3: Schematic presentation of the MF sieving process: (1) particle adheres to the surface; (2) particle partially blocks a pore, allowing flow to continue through the pore; (3) a small particle passes through a large pore; (4) a particle approaching the surface that may or may not partially block a pore.

Starting as above to determine the probability that an elliptical pore is not blocked at a given time yields:

$$P\left(b,\bar{t}\right)=\left(1-\pi\beta l^{2}ab\big/S\right)^{n\left(b,\bar{t}\right)} \tag{5.10}$$

where *a* is half the length of the major axis and *b* is half the length of the minor axis. Figure 5.4 defines the geometry used to describe elliptical pores in this chapter.

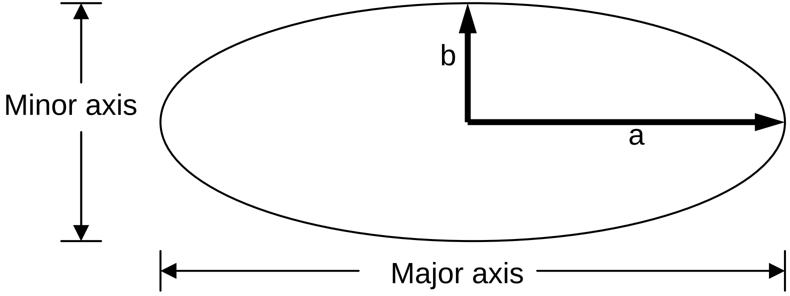

Figure 5.4: Definition of characteristic lengths of an elliptical pore.

The equation for the number of particles blocking the pore keeps the same form as in Equation 5.3. Once again making the assumptions that the pore area is small compared to the surface area of the membrane and that the number of particles capable of blocking pores is much greater than one results in:

$$P\left(b,\bar{t}\right)=\exp\left[-\left(\pi\beta l^{2}abc\right)\int_{0}^{\bar{t}}J\left(u\right)du\int_{2b}^{D_{\max}}f_{p}\left(D\right)dD\right] \tag{5.11}$$

It is possible to non-dimensionalize Equation 5.11 with the same definitions of non-dimensional flux and non-dimensional time used in the previous derivation to yield:

$$P\left(b,t\right)=\exp\left[-\left(4ab\right)\int_{0}^{t}j\left(u\right)du\int_{2b}^{D_{\max}}f_{p}\left(D\right)dD\right] \tag{5.12}$$

Poiseuille flow through an elliptical pore is described by [16, 17]:

$$Q\left(a,b\right)=-\frac{\pi\Delta p}{4\mu L}\left(\frac{a^{3}b^{3}}{a^{2}+b^{2}}\right) \tag{5.13}$$

Averaging over all of the elliptical pores results in:

$$J_{0}=\frac{N_{m}\pi\ l^{4}\Delta p}{4\mu LSA} \tag{5.14}$$

where A is defined as:

$$A=\left[\int_{a_{\min}}^{a_{\max}}\int_{b_{\min}}^{b_{\max}}\frac{a^{3}b^{3}}{a^{2}+b^{2}}f_{m}\left(a\right)f_{m}\left(b\right)dbda\right]^{-1} \tag{5.15}$$

Using Equations 5.14 and 5.15 to write an expression for flux decline over time yields

$$\begin{aligned}J\left(\bar{t}\right)=J_{0}A\int_{a_{\min}}^{a_{\max}}\int_{b_{\min}}^{b_{\max}}\frac{a^{3}b^{3}}{a^{2}+b^{2}}f_{m}\left(a\right)f_{m}\left(b\right)P\left(b,\bar{t}\right)dbda\ +\\ J_{o}A\int_{a_{\min}}^{a_{\max}}\int_{b_{\min}}^{b_{\max}}\frac{a^{3}b^{3}}{a^{2}+b^{2}}f_{m}\left(a\right)f_{m}\left(b\right)\left(1-P\left(b,\bar{t}\right)\right)\left(\int_{2b}^{D_{\max}}\phi\left(\frac{a}{b},\frac{D}{2b}\right)f_{p}\left(D\right)dD\right)dbda\end{aligned} \tag{5.16}$$

where *φ(a/b, D/2b)* is a function describing the fluid flow through a partially blocked pore. The development of this function is outlined below in section 5.2.4.

The integration of Equation 5.16 is non-trivial and the solution heavily depends on the choice of distributions for the major and minor axes. As such, a further simplification is needed if a usable tool is to be developed. In Chapter 4, a model to predict the change of major and minor axes at varying elongations was developed and compared to experimental results. It is seen graphically in Chapter 4 that: (1) the change in the length of the major axis is much greater than the change in the minor axis, and (2) the change in width of the major axis distribution is greater than the change in width of the minor axis distribution. As such, the change in *a* is dominant in flux calculations and *$f_m(b)$* can be considered as a delta function with *b* equivalent to the mean value. This allows for Equation 5.16 to reduce to:

$$J\left(\bar{t}\right) = J_0 A \int_{a_{\min}}^{a_{\max}} \frac{a^3 b^3}{a^2+b^2} f_m(a) P\left(b,\bar{t}\right) da + \\ J_0 A \int_{a_{\min}}^{a_{\max}} \frac{a^3 b^3}{a^2+b^2} f_m(a) \left(1 - P\left(b,\bar{t}\right)\right)\left(\int_{2b}^{D_{\max}} \phi\left(\frac{a}{b},\frac{D}{b}\right) f_p(D)\, dD\right) da \qquad (5.17)$$

with Equation 5.15 becoming:

$$A = \left[\int_{a_{\min}}^{a_{\max}} \frac{a^3 b^3}{a^2+b^2} f_m(a)\, da\right]^{-1} \qquad (5.18)$$

Equation 5.17 may then be non-dimensionalized using the previous definitions to yield:

$$j(t) = Ab^3 \int_{a_{\min}}^{a_{\max}} \frac{a^3}{a^2+b^2} f_m(a) \exp\left[-4ab\int_0^t j(u)\,du \int_{2b}^{D_{\max}} f_p(D)\, dD\right] da + \\ Ab^3 \int_{a_{\min}}^{a_{\max}} \frac{a^3}{a^2+b^2} f_m(a) \left(1 - \exp\left[-4ab\int_0^t j(u)\,du \int_{2b}^{D_{\max}} f_p(D)\, dD\right]\right)\left(\int_{2b}^{D_{\max}} \phi\left(\frac{a}{b},\frac{D}{b}\right) f_p(D)\, dD\right) da \qquad (5.19)$$

Equations 5.18 and 5.19 can be easily evaluated numerically for any given distribution type (*i.e., normal or log-normal)*, in Matlab with Simpson's rule for the integrations.

Since Equations 5.16−5.19 represent the averaging of the volumetric flow over all the pores, it is possible to construct a discrete model that evaluates the behavior of thousands of individual pores over time to provide approximate results. These approximations can serve as a validation method for the developed equations and the associated programs.

5.2.2 Discrete method for modeling circular pores

A model was developed to represent the blocking of individual pores over time and thereby to track the flux decline of the membrane. Approximately 20,000 individual circular pores were created in Matlab with a given distribution of pore diameters. A non-dimensionalized form of Equation 5.3 was used to determine whether a pore was open or blocked at a given time. The flux through the membrane was then calculated by summing the flow through each pore. Simpson's rule was used to evaluate the integral of the particle size distribution, as above in Equation 5.9.

5.2.3 Discrete method for modeling elliptical pores

The model described in the previous section was adapted for use with elliptical pores. The 20,000 individual pores were assigned unique major and minor axes lengths according to their distributions, given in section 5.3. Equation 5.12 was used to determine whether the pores were partially blocked or open at a given time. The development of flow through a partially blocked pore is described in the following section.

5.2.4 Flow through partially blocked elliptical pores

One of the unique and advantageous issues with dead-end MF with elliptical pores is that the pores cannot be completely blocked. There is always some remainder of area available for flow as shown in Figure 5.3 above. Flow around a spherical particle in a circular or elliptical channel is the subject of significant computerized fluid dynamics (CFD) work [18]. As one of the objectives of this work is to provide usable tools to the community that do not require significant expertise or computational resources to solve, a CFD approach to solve for flow around a spherical particle at the entrance to a elliptical pore was not attempted. Rather, an approximation was made by combining results from Stokes flow around a sphere and the steady-state velocity profile within the elliptical pore. Stokes flow around a sphere gives the velocity perpendicular to the membrane surface as:

$$u_z = u_r \cos\theta - u_\theta \sin\theta \tag{5.20}$$

where θ is an angle as shown in Figure 5.4, and u_r and u_θ are defined by [19]:

$$u_r = u_\infty\left(1 - \frac{3}{2}\left(\frac{R}{r}\right) + \frac{1}{2}\left(\frac{R}{r}\right)^3\right)\cos\theta \tag{5.21}$$

$$u_\theta = -u_\infty\left(1 - \frac{3}{4}\left(\frac{R}{r}\right) - \frac{1}{4}\left(\frac{R}{r}\right)^3\right)\sin\theta \tag{5.22}$$

The steady-state velocity profile within the elliptical pore is given by White [17] as:

$$u(y,z) = \frac{\Delta p}{2\mu}\left(\frac{a^2b^2}{a^2+b^2}\right)\left(1 - \frac{y^2}{a^2} - \frac{z^2}{b^2}\right) \tag{5.23}$$

Super-imposing the two results on a graph for a given *a/b* and *D/2b* ratio and a specific angle θ produces Figure 5.5. The intersection of the two curves is found easily, and the area underneath the curves is integrated to get the average velocity along the specific angle. It is worth noting that the two curves form a discontinuity at the intersection, but it is assumed this is an acceptable approximation for the parabolic-like shape that would result in experiments. The average velocity is found for angles between zero and ninety degrees, as symmetry makes any further determination repetitive. These velocities are then weighted according to the distance from the particle to the pore wall on the plane of intersection of the membrane surface. An average velocity is computed using the weightings and is multiplied by the area of the pore that is unblocked. The resulting partially blocked pore volumetric flowrate is then divided by the initial unblocked pore volumetric flowrate to yield a fraction that enters into Equations 5.16, 5.17 and 5.19 through *φ(a/b, D/2b)*. Table 5.1 shows the effect of the aspect ratio and the ratio of particle size to minor axis on flow through partially blocked pores. Figure 5.6 shows a graphical representation of the data in Table 5.1. In the discrete model, Table 5.1 is directly used to calculate the fraction of original flow that occurs through each partially blocked pore.

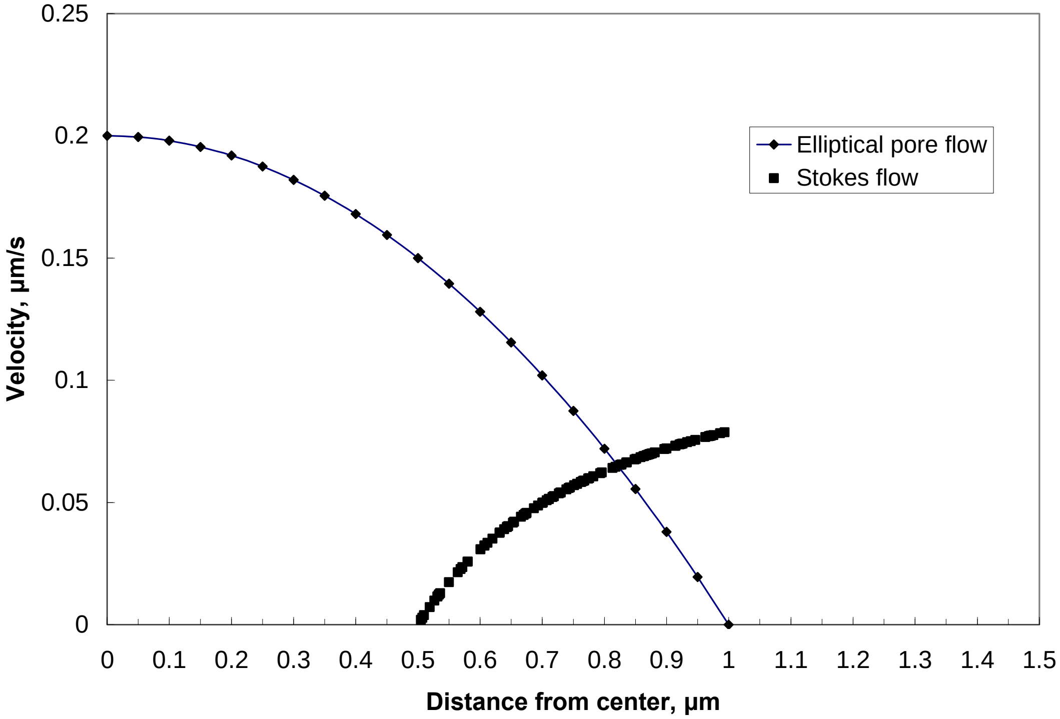

Figure 5.5: A comparison of the solution for velocity profile along the major axis ($\theta = 0$) for the elliptical pore and the velocity profile from Stoke's flow around a sphere. The conditions for this example are an aspect ratio of 2 and $D/2b = 1$.

Table 5.1: The blockage factor is the fraction of unfouled flux for a pore with a given aspect ratio and a given particle to minor axis ratio.

		D/2b Ratio															
		1.0	1.2	1.4	1.6	1.8	2.0	2.2	2.4	2.6	2.8	3.0	3.2	3.4	3.6	3.8	4.0
Aspect Ratio	1.0	0.000	0.000	0.000	0.000	0.000	0.000	0.000	0.000	0.000	0.000	0.000	0.000	0.000	0.000	0.000	0.000
	1.2	0.009	0.004	0.002	0.001	0.001	0.000	0.000	0.000	0.000	0.000	0.000	0.000	0.000	0.000	0.000	0.000
	1.4	0.027	0.014	0.007	0.004	0.003	0.002	0.001	0.001	0.000	0.000	0.000	0.000	0.000	0.000	0.000	0.000
	1.6	0.048	0.026	0.015	0.009	0.006	0.004	0.002	0.002	0.001	0.001	0.001	0.000	0.000	0.000	0.000	0.000
	1.8	0.068	0.039	0.024	0.015	0.010	0.006	0.004	0.003	0.002	0.002	0.001	0.001	0.001	0.001	0.000	0.000
	2.0	0.088	0.053	0.034	0.022	0.015	0.010	0.007	0.005	0.004	0.003	0.002	0.001	0.001	0.001	0.001	0.001
	2.2	0.107	0.067	0.044	0.029	0.020	0.014	0.010	0.007	0.005	0.004	0.003	0.002	0.002	0.001	0.001	0.001
	2.4	0.125	0.081	0.054	0.037	0.026	0.019	0.013	0.010	0.007	0.006	0.004	0.003	0.003	0.002	0.002	0.001
	2.6	0.141	0.093	0.064	0.045	0.032	0.024	0.017	0.013	0.010	0.007	0.006	0.004	0.004	0.003	0.002	0.002
	2.8	0.156	0.106	0.074	0.053	0.039	0.029	0.021	0.016	0.012	0.010	0.007	0.006	0.005	0.004	0.003	0.002
	3.0	0.170	0.117	0.084	0.061	0.045	0.034	0.026	0.020	0.015	0.012	0.009	0.007	0.006	0.005	0.004	0.003
	3.2	0.183	0.129	0.094	0.069	0.052	0.040	0.030	0.024	0.018	0.015	0.012	0.009	0.007	0.006	0.005	0.004
	3.4	0.195	0.139	0.103	0.077	0.059	0.045	0.035	0.028	0.022	0.017	0.014	0.011	0.009	0.007	0.006	0.005
	3.6	0.206	0.149	0.111	0.085	0.065	0.051	0.040	0.032	0.025	0.020	0.016	0.013	0.011	0.009	0.007	0.006
	3.8	0.216	0.159	0.120	0.092	0.072	0.056	0.045	0.036	0.029	0.023	0.019	0.015	0.013	0.011	0.009	0.007
	4.0	0.226	0.168	0.128	0.099	0.078	0.062	0.050	0.040	0.032	0.026	0.022	0.018	0.015	0.012	0.010	0.009
	4.2	0.236	0.176	0.136	0.106	0.084	0.068	0.054	0.044	0.036	0.030	0.024	0.020	0.017	0.014	0.012	0.010
	4.4	0.244	0.184	0.143	0.113	0.090	0.073	0.059	0.048	0.040	0.033	0.027	0.023	0.019	0.016	0.014	0.011
	4.6	0.253	0.192	0.150	0.120	0.096	0.078	0.064	0.053	0.044	0.036	0.030	0.025	0.021	0.018	0.015	0.013
	4.8	0.261	0.200	0.157	0.126	0.102	0.084	0.069	0.057	0.047	0.040	0.033	0.028	0.024	0.020	0.017	0.015
	5.0	0.268	0.207	0.164	0.132	0.108	0.089	0.074	0.061	0.051	0.043	0.036	0.031	0.026	0.022	0.019	0.016

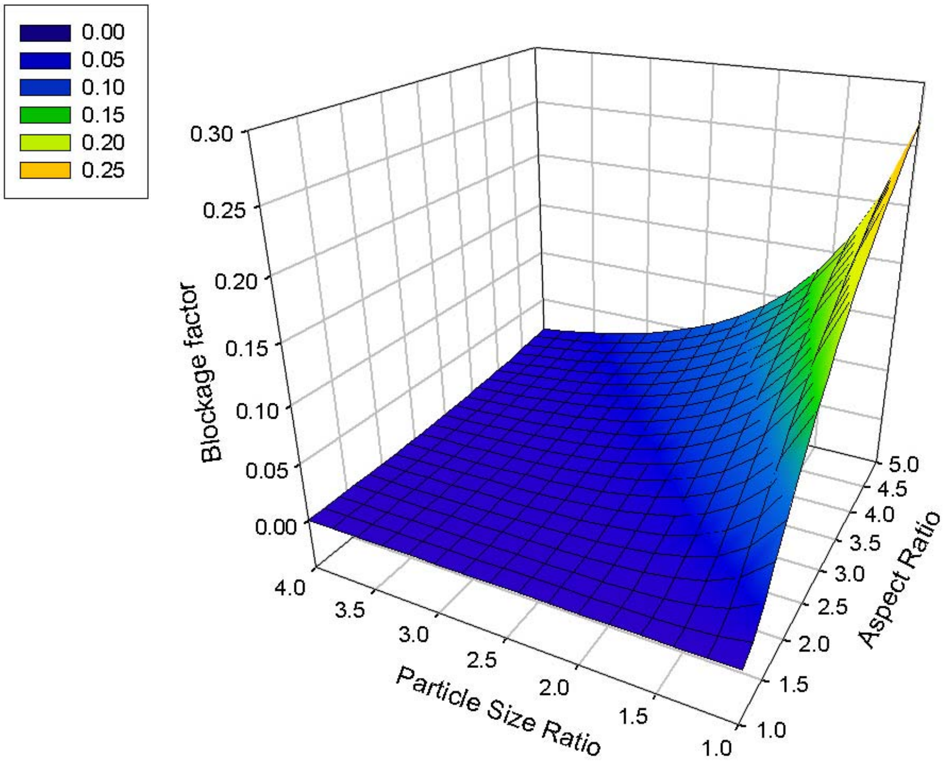

Figure 5.6: A graphical representation of the data in Table 5.1, showing the effect of aspect ratio and particle size ratio on flow through a partially blocked pore.

5.2.5 Distribution Determination

The distributions used to model the pore diameters, major axes, and minor axes were obtained from the modeling work in Chapter 4. These values were previously determined to correlate well to experimental data, and minimized some of the scatter reported previously [20]. Minimizing the effects of scatter are important as the reported lengths of the axes are compounded as the quantities are cubed. Table 5.2 contains the information regarding the membrane pore morphologies of the 0.6 μm PET TE membranes at a variety of strains from no strain to 36% strain. The normal particle distributions were arbitrarily chosen to highlight the performance differences of the membranes and are given in Table 5.3.

Table 5.2: Distribution parameters of the 0.6 μm membranes represented by normal distributions.

Percent Elongation	Major axis Mean	Major axis Standard Deviation	Minor axis Mean	Minor axis Standard Deviation
0.00	–	–	0.637	0.070
8.85	0.818	0.127	0.571	0.032
17.68	0.970	0.153	0.555	0.035
26.57	1.115	0.182	0.548	0.043
35.61	1.260	0.216	0.541	0.047

Table 5.3: Distribution parameters of particles represented by normal distributions.

Mean	Standard Deviation
0.652	0.0195
1.000	0.0500

5.3 RESULTS AND DISCUSSION

5.3.1 Circular pore results

The Matlab programs were used to compute the flux, volume of the permeate, and pore size distribution over time. Figure 5.7 below shows good correlation of the flux results between Equation 5.9 and the discrete model for the 0.6 μm membrane. Neither program requires much computational time, but Equation 5.9 is the fastest solution. As such, Equation 5.9 is used to produce all of the circular pore data in this chapter. Other results of the programs are given below to demonstrate the effect of pore elongation on performance.

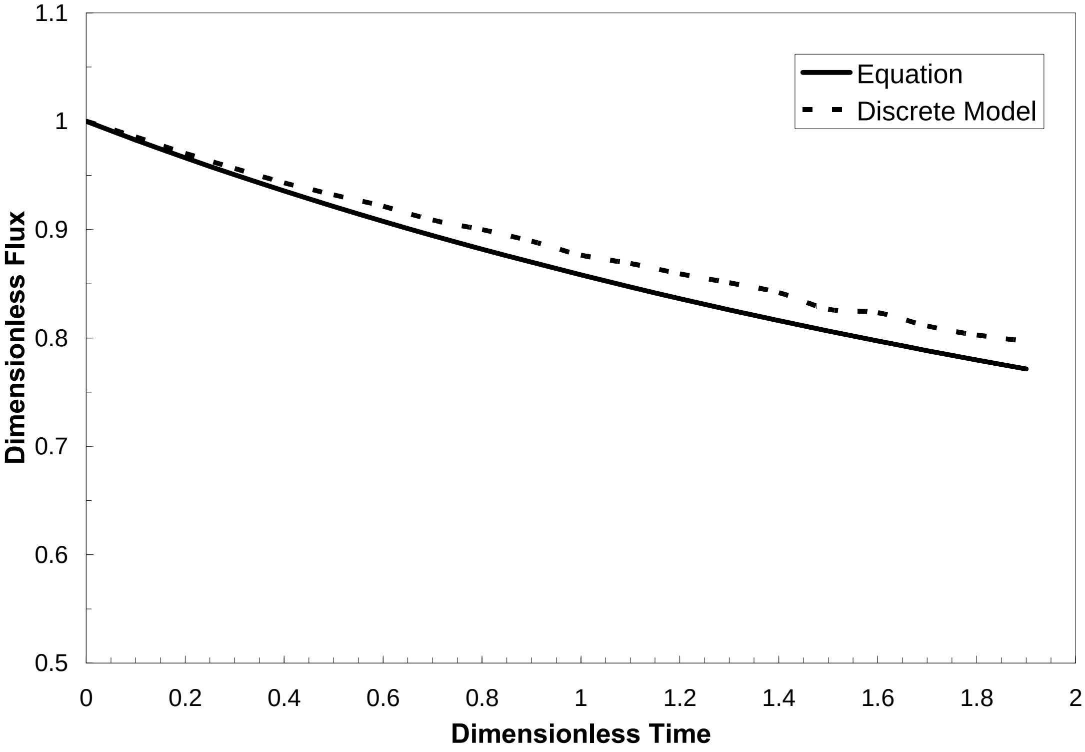

Figure 5.7: The difference between Equation 5.9 and the discrete model are slight over time scales of interest.

5.3.2 Elliptical pore results

The primary focus of this discussion are the results of the 0.6 μm membrane from Chapter 4 because it has the smallest entrance length according to Worrel [20]. The entrance length is important as the assumption has been made that fully developed Pouiselle flow occurs in the pores. If the entrance length is greater than the thickness of the membrane (approximately 13 micrometers) then Pouiselle flow will not be fully developed. The 0.6 μm membrane from Chapter 4 also has the lowest Reynolds number, 0.03 [20], making the Stokes flow assumption the most applicable of any of the membranes.

The particle size distributions and the distribution of the minor axes, which govern the sieving ability of the membrane, are given below in Figure 5.8. The particle distributions were chosen in order to elucidate the performance changes as a result of changing the pore morphology.

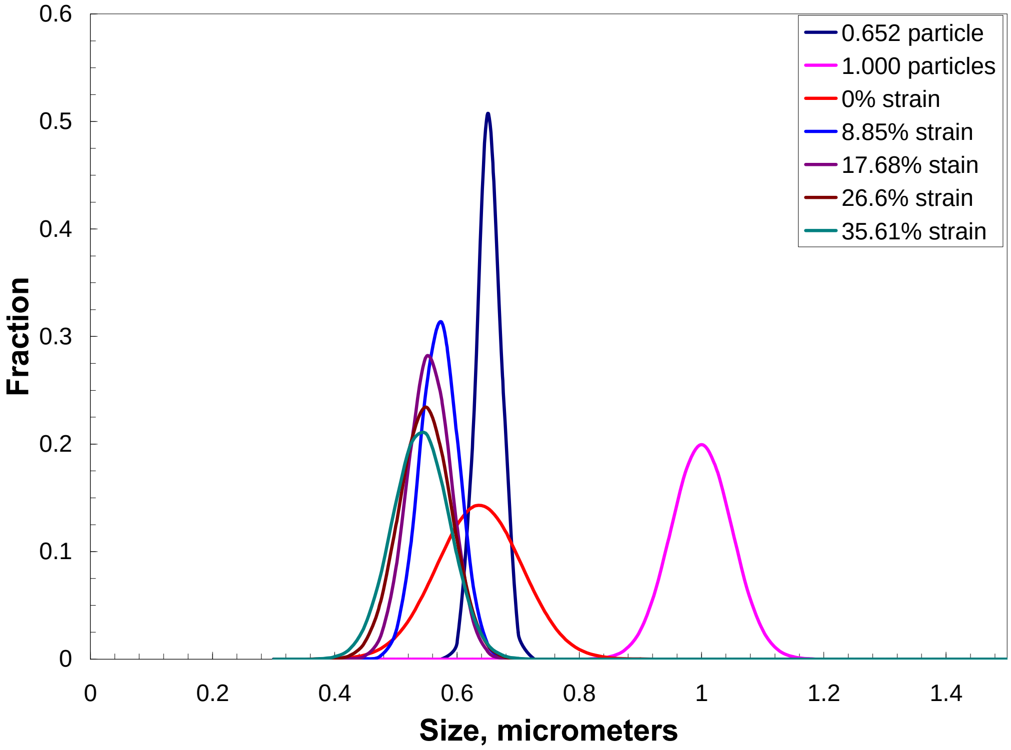

Figure 5.8: The particle distributions and distributions of minor axis used in the models for the 0.6 μm PET TE membrane.

Prior to presenting the results of the elliptical models, it is worth noting that a common basis must be chosen in order for meaningful comparisons of flux to be drawn. The results below are presented in terms of comparative flux, relative to the non-stretched circular pore membrane, and normalized time, which is relative to the dimensionless time of the non-stretched membrane. The presentation on a common basis allows the results to be directly compared, while maintaining a degree of flexibility as the viscosity of the fluid, thickness of the membrane, number of pores per given area, and pressure drop are not explicitly defined. Equations 5.6 and 5.14 can be combined to yield the following conversion factor:

$$\frac{J_{0,ellipse}}{J_{0,circle}} = 32 A_{circle} A_{ellipse}^{-1} \tag{5.25}$$

where A_{circle} is defined by Equation 5.7 and $A_{ellipse}$ is defined by Equation 5.18. The dimensionless time scale for each membrane is then adjusted by the comparative flux to obtain a common time scale, as the equation for dimensionless time contains a flux term in the denominator.

Using the relative dimensionless flux and relative dimensionless time allows comparison of the 0.6 μm membrane at various strains on a common basis as shown in Figure 5.9. The particle size used in Figure 5.9 is 0.652 μm with a standard deviation of 0.0195 μm as shown in Table 5.3, which corresponds to experimental data gathered by Worrel [20] and presented in Figure 5.10. The two figures share qualitative trends and in both cases, modification of the membrane morphology by elongation significantly improved initial flux. Additional comparison to experimental data is not possible due to the dearth of information and experimental results. However, Figure 5.9 highlights that elongation to higher strains continues to improve initial flux performance. The non-strained membrane surpasses the membranes with the smallest strains in terms of flux because the elongated membranes are rejecting all of the particles, leading to a faster flux decline. By contrast, 49% of the circular pores are larger than the mean diameter of the particles, which allows particles to pass through the membrane and not suffer flux decline.

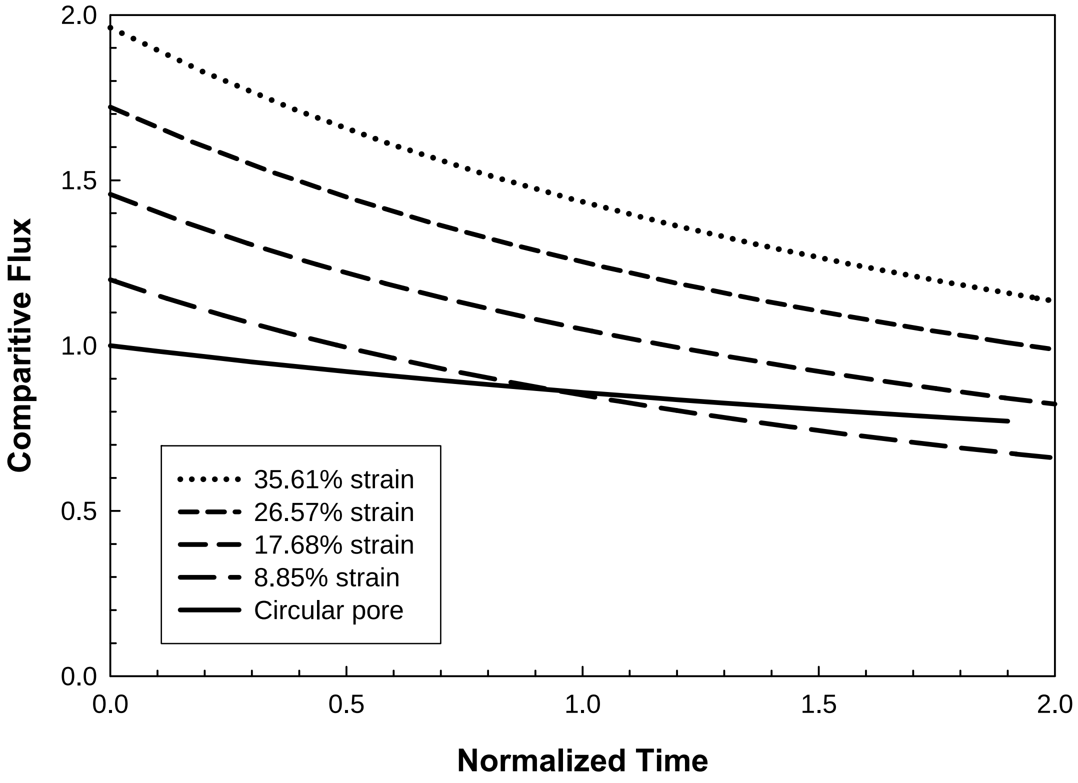

Figure 5.9: The effect of stretching on initial flux and flux decline is beneficial for a 0.6 micron PET membrane with 0.652 micron particles in the feed.

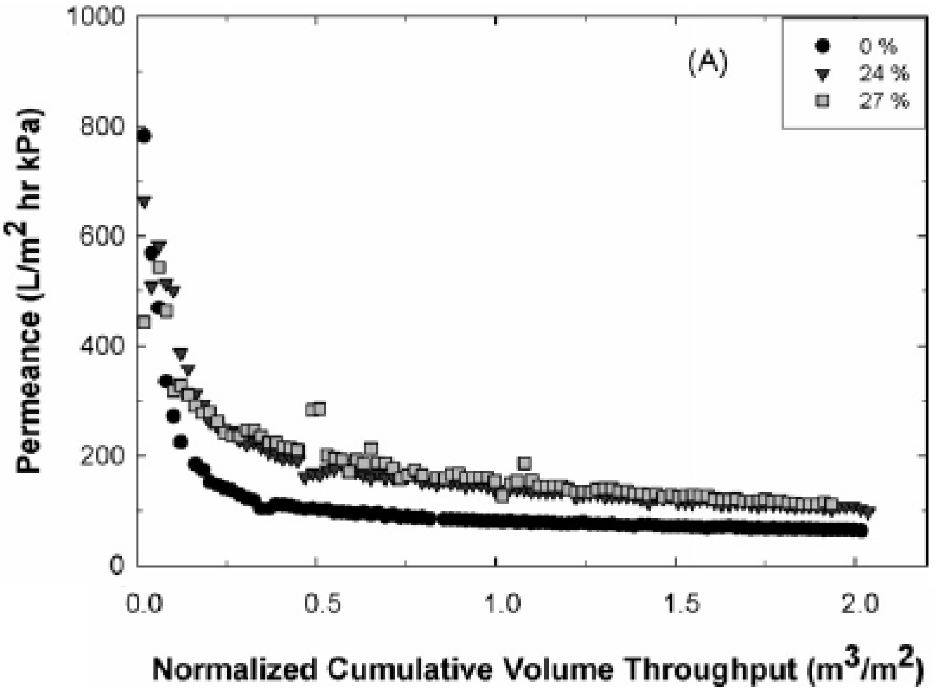

Figure 5.10: Experimental data corresponding to conditions in Figure 5.9. [20]

Figure 5.11 demonstrates that elongation has a more marked effect on filtrations with particle diameters larger than the minor axis and original diameter of the pore. In this case, flux decline of the non-stretched membrane and the elongated membrane are similar. The flux decline is approximately the same for all the membranes due to the relatively small amount of flux allowed through the partially blocked pores due to small aspect ratios. The effect of aspect ratio on flux decline would best be seen in membranes with large aspect ratios; however, the PET TE membranes aspect ratios at large strain only approach 3. Figure 5.12 presents the data in Figure 5.11 in terms of volume of permeate over time. It shows that the 35.61% strain TE membrane has filtered approximately 2.1 times as much liquid as the original non-stretched membrane.

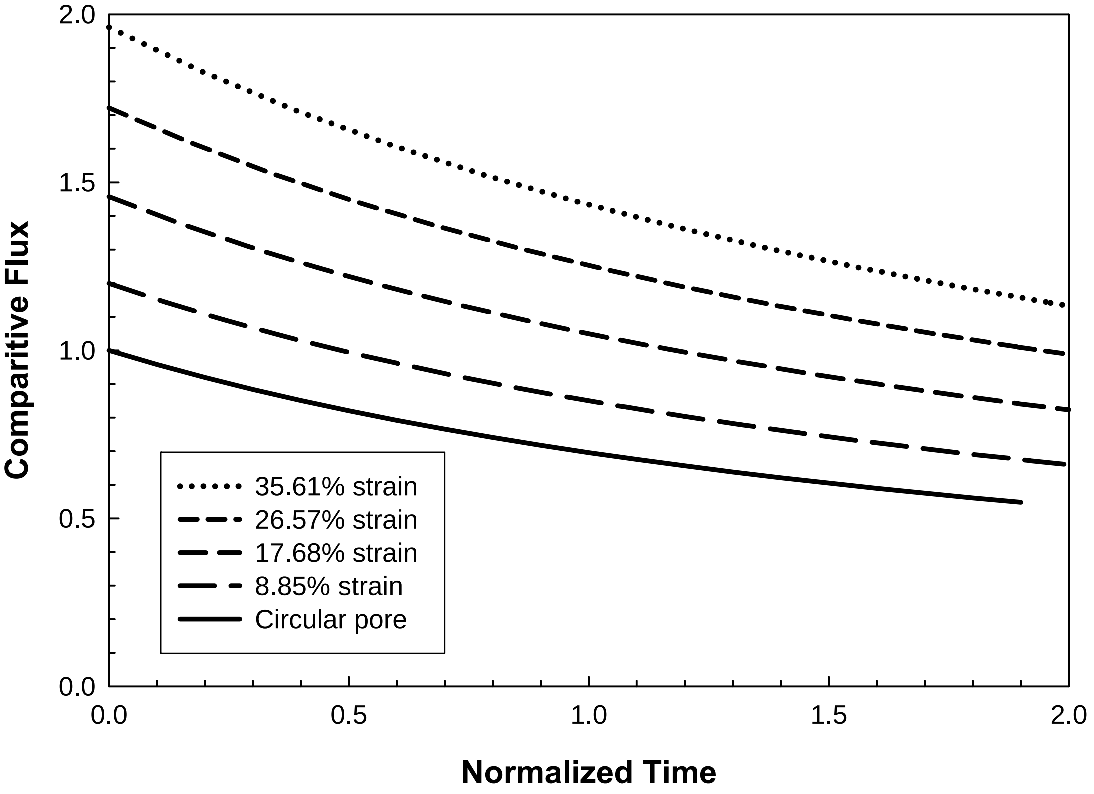

Figure 5.11: A 0.6 μm membrane at various strains fed particles with an average size of 1 μm and a standard deviation of 0.05 μm.

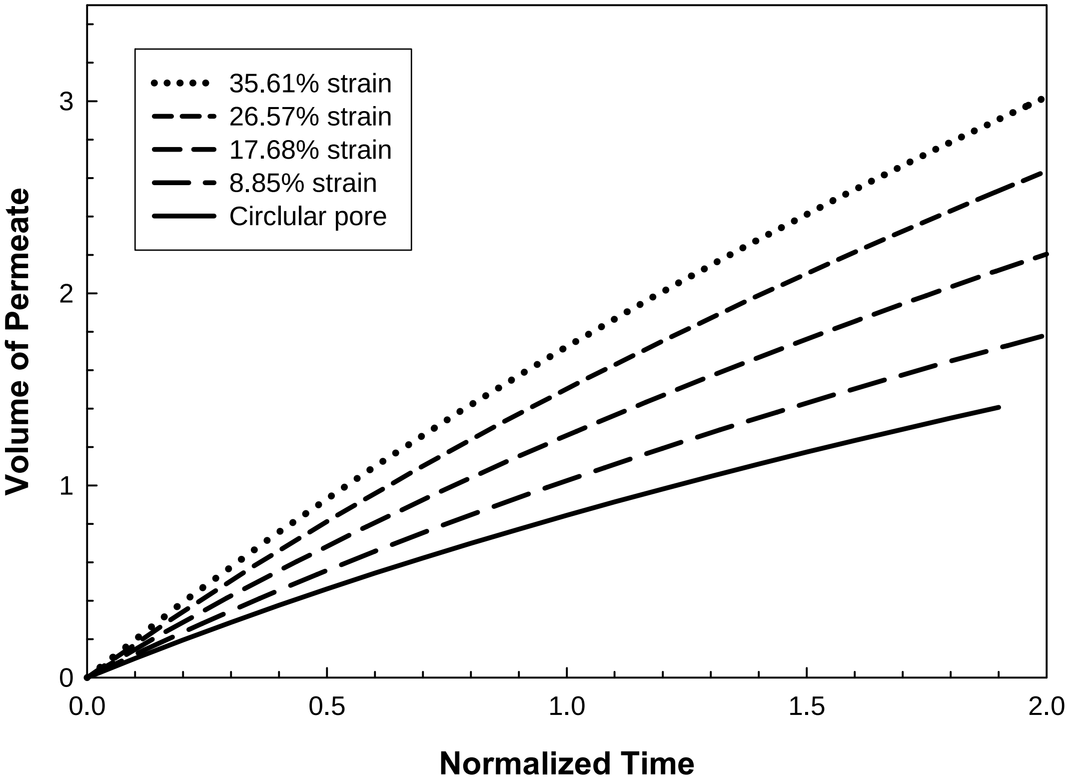

Figure 5.12: Volume of permeate generated over time shows a significant increase with elongation.

5.4 CONCLUSIONS

The sieve models developed herein are of use to applications that begin with relatively low concentrations of particles in the feedstock, such as water filtration for microelectronics and pharmaceuticals. The solution of equations for filtration with circular pores is preferable to the discrete method, as it is computationally faster and provides a unique repeatable result. However, for the elliptical pores, solution of Equation 5.16 is difficult, often resulting in terms of an infinite series depending on the distribution used for the axes. Reducing the complexity of the solution by making an assumption of the minor axis being adequately modeled by a delta function at the mean value leads to Equation 5.19, which compares well to a discrete model that includes a minor axis distribution.

The results show that elongation has a significant benefit to membrane performance as measured by flux and volume of permeate generated. In the examples for the 0.6 μm PET TE membrane fed with 1.0 μm particles, a 35.6% strain allowed for twice the throughput compared to the original membrane, while maintaining the same removal ability.

Ultimately, the models are handicapped by the lack of availability for validation. Previous papers detailing the sieve mechanism are incomplete in providing details necessary for replication of results. Additionally, the capabilities necessary for experimental comparisons are beyond that available in our labs. Future work on performance modeling of modified TE membranes should focus on the experimental options to determine the suitability of assumptions and techniques employed in the numerical methods.

5.6 REFERENCES

1 M. Chandler and A. Zydney, *Effects of membrane pore geometry on fouling behavior during yeast cell microfiltration*, Journal of Membrane Science, 285 (2006) 334-342.

2 L.S. Worrel, L.A. Shimko, J.A. Morehouse, D. R. Lloyd, B.D. Freeman, and D.F. Lawler, *Enhancement of Track-etched Membrane Performance via Stretching*, Separation and Purifications Technology, 53 (2007) 71-80.

3 J. Morehouse, *The effect of uni-axial stretching on microporous phase-separation membrane structure and performance*, Dissertation, University of Texas at Austin, 2006.

4 C. Duclos-Orsello, W. Li, and C. Ho, *A three mechanism model to describe fouling of microfiltration membranes*, Journal of Membrane Science, 280 (2006) 856-866.

5 M. Taniguchi, J. Kilduff, and G. Belfort, *Modes of natural organic fouling during ultrafiltration*, Enviromental Science and Technology, 37 (2003) 1676-1683.

6 A. Filippov, V.M. Starov, and S.V. Gleizer, *Mathematical modeling of the microfiltration process by means of a probabilistic-sieve mechanism*, Soviet journal of Water Chemistry and Technology, 12 (1990) 483-488.

7 A. Filippov, V.M. Starov, D.R. Lloyd, S. Chakravarti, and S. Glaser, *Sieve mechanism of microfiltration*, Journal of Membrane Science, 89 (1994) 199-213.

8 J.A. Howell, O. Velicangil, M.S. Le, and A.L. Herrera-Zeppelin, *Ultrafiltration of protein solutions*, Annals of the New York Academy of Sciences, 369 (1981) 355-366.

9 S. Kosvintsev, R. Holdich, I. Cumming, and V. Starov, *Modelling of dead-end microfiltration with pore blocking and cake formation*, Journal of Membrane Science, 208 (2002) 181-192.

10 S. Kosvintsev, I. Cumming, R. Holdich, D.R. Lloyd, and V. Starov, *Seive mechanism of microfiltration separation*, Colloids and Surfaces, 230 (2004) 167-182.

11 V. Starov, D.R. Lloyd, A. Filippov, and S. Glaser, *Sieve mechanism of microfiltration separation*, Separation Purification Technology, 26 (2002) 51-59.

12 F.N. Kemmer (Ed.), *The NALCO Water Handbook*, 2nd ed, McGraw-Hill, New York, 1987.

13 H. Brenner, *The slow motion of a sphere through a viscous fluid towards a plane surface*, Chem. Eng. Sci., 16 (1961) 242-251.

14 A.J. Goldmann, R.G. Cox, and H. Brenner, *Slow viscous motion of a sphere parallel to a plane wall. 1. Motion through a quiescent fluid*, Chem. Eng. Sci., 22 (1967) 637-652.

15 A.J. Goldmann, R.G. Cox, and H. Brenner, *Slow viscous motion of a sphere parallel to a plane wall. 2. Couette flow.*, Chem. Eng. Sci., 22 (1967) 653-660.

16 A.R. Berker, *Integration des equations du mouvement d'un fluid visqueux incompressible*, Encyclopedia of Physics, vol. 8, S. Flugge, Ed. Berlin: Springer (1963).

17 F.M. White, *Viscous Fluid Flow*, 2nd ed, McGraw-Hill, New York, 1991.

18 X.L. Luo, *Operator splitting algorithm for viscoelastic flow and numerical analysis for flow around a sphere in a tube*, J. Non-Newtonian Fluid Mech., 63 (1996) 121-140.

19 R.B. Bird, W.E. Stewart, and E.N. Lightfoot, *Transport Phenomena*, 2nd ed, John Wiley and Sons Inc., New York, 2002.

20 L.S. Worrel, *Modification of Track-Etched Membrane Structure and Performance via Uniaxial Stretching*, Dissertation, The University of Texas at Austin, 2005.

Chapter 6: Conclusions and Recommendations

6.1 CONCLUSIONS

The goal of this research, to describe and model the steps of liquid–liquid thermally induced phase separation (L−L TIPS) membrane production and the impact post-coarsening processes have on performance, was accomplished by systematically investigating the processes of: matrix solidification, drying of microporous materials, and uni-axial elongation of simplified track-etch (TE) geometries. The investigation into post-coarsening processes has identified key considerations in membrane formation and have provided the membrane science community with tools to model the development and changes to the microporous morphology. Conclusions from the work presented in the previous chapters are as follows:

6.1.1 Matrix Solidification

1. The simple deterministic approach for modeling matrix solidification using a series of material balances utilized in this research can provide accurate predictions of final cell size diameter and distribution for isotropic L–L TIPS membranes given information about the polymer-lean phase in the liquid–liquid region.
2. These material balances account for: movement of diluent and further merging events occurring during the quench to the crystallization curve; shrinkage due to densification caused by cooling beyond the crystallization curve; and swelling of the solidified polymer.
3. While requiring significant physical data, the run-time is short enough to be useful and is the first simulation to take into account the compositional change of the matrix

phase during non-isothermal quenching of an L–L TIPS system that has gone through droplet coarsening.

6.1.2 Drying of Microporous Membranes

1. Strong experimental evidence was presented showing that the experimentally observed shrinkage of microfiltration (MF) membranes is not dominated by capillary forces.
2. Simulations indicate that capillary forces alone due not have the capability to deform the isotractic polypropylene (iPP) or poly(ethylene co-vinyl alcohol) (EVAL44) cellular MF membranes, which supports the lack of cell size dependence on surface tension.
3. The experimental results showing capillary forces to be insufficient to explain the collapse of MF membranes are similar to those obtained by Vos and Burris [1] for reverse osmosis membranes.
4. It is proposed to add a heuristic to the customary rules in selection of an extractant; choose an extractant that is more alkane-like, even at the expense of increasing surface tension. Adding this heuristic should avoid selection of an extractant that would cause excessive collapse. This heuristic should be considered particularly when dealing with polar polymers.

6.1.3 Modeling uni-axial elongation of TE membranes

1. Finite element analysis adequately predicts morphological changes to the pore structure of TE membranes caused by uni-axial stretching. The simulations developed relate the initial pore size, membrane material properties, thermal history, and elongation to the final major and minor axes. The change to the major and minor

axis lengths gives an indication to the separation abilities of the modified membrane and can allow manufacturers to tailor make membranes for specific applications.

2. While only shown for poly(ethylene teraphthalate) membranes, these same techniques should also describe morphological changes in other polymer TE membranes capable of deformation.

6.1.4 Performance effects of pore shape change

1. New models based upon the sieve filtration mechanism [2-4] were developed to include elliptical pores, which correspond to the elongated pores caused by uni-axial elongation of TE membranes.
2. The model results show that elongation has a significant benefit to membrane performance as measured by flux and volume of permeate generated. In the examples for the 0.6 μm PET TE membrane fed with 1.0 μm particles, a 35.6% strain allowed for twice the throughput compared to the original membrane, while maintaining the same removal ability.

6.2 RECOMMENDATIONS FOR FUTURE WORK

The research described herein is broad in scope, encompassing several post-coarsening processes and modeling efforts. The conclusions listed above may serve as a basis for advances in membrane manufacturing and usage; however, additional work is still required to see the concepts detailed in this dissertation to full fruition. The work on drying of microporous membranes is an advancement on the work of others and provided an additional heuristic in extractant selection, but is not complete. A larger experimental data set may allow some quantification of the observed effects. The elongation of TE membranes was investigated as a stepping stone to examining the effect on cellular morphologies of L−L TIPS. Additional work in finite element analysis of the issue should straightforward to obtain the change in cell configuration, since finite elements have been shown to be successful for TE membranes in this work and elsewhere for phase inversion membranes [5]. Experimental validation of the modified sieving mechanism is required before more complex modeling of cake growth formation, which would correspond to longer filtration times, can be achieved.

Perhaps the most interesting future work is direct application of the concepts, programs, and conclusions of this dissertation to real-world problems. In the introduction, it was suggested that several applications could benefit from increased understanding of fundamentals of L−L TIPS membrane production. One of the applications was battery separators, where increased porosity can lead to increased capacity. Yet, other factors like the thickness of the membrane, strength, lack of a skin, and a shut-off capability must be maintained. Using the work of this dissertation, it would be recommended to use a blend of an ultra-high molecular weight polyethylene (PE) or iPP (greater than 2,000,000) and a low molecular weight PE or iPP (less than 30,000). The low molecular weight iPP will maintain the shut-off capability, while the ultra-high molecular weight will provide strength and a viscosity suitable for extrusion at 10 wt% polymer solutions or less. The low concentration of polymer allows for a large concentration of diluent which will form the void spaces of the resulting membrane. If the solution is co-extruded with a layer of diluent coating the outside, a skin layer should not be formed. By cooling quickly, spinodal decomposition can be induced which will result in a small distribution of cell sizes, which is also necessary for the shut-off capability. Uni-axial elongation of the membrane can also increase porosity and reduce the thickness of the membrane to a useful amount.

Similar reasoning can be used to determine worthwhile starting points for membrane development for membrane distillation (MD). In the introduction it was noted that MD requires a hydrophobic polymer, small pores with a tight distribution, and large porosities for optimal performance [6]. While current researchers are trying to make polymers hydrophobic by adding clay particulates [7], it is proposed to use a similar method to that described above for battery separators. An ultrahigh molecular weight PE or iPP provides hydrophobicity without modification, mechanical strength, and allows for low polymer concentrations that, in turn, increase porosity. Inducing spinodal decomposition will result in small pores with a tight pore size distribution. Stretching the membranes will reduce the minor axis length, which in turn increases the amount of pressure that can be applied to the fluids without wetting the membrane. The elongation will also thin the membrane, reducing the distance the water vapor must travel. Additionally, it is suggested to produce these membranes in a hollow fiber geometry with a large bore/lumen so that relatively large amounts of cold salt-free water can flow down the inside of the fiber. This large cold water flow will absorb the heat from the condensing water vapor without significantly increasing the temperature and reducing the driving force. These recommendations should allow for the development of a new MD membrane at the high end of the performance spectrum.

6.3 REFERENCES

1 K.D. Vos and F.O. Burris, *Drying cellulose acetate reverse osmosis membranes*, Industrial and Engineering Chemistry Product Research and Development, 8 (1969) 84-89.

2 A. Filippov, V.M. Starov, and S.V. Gleizer, *Mathematical modeling of the microfiltration process by means of a probabilistic-sieve mechanism*, Soviet journal of Water Chemistry and Technology, 12 (1990) 483-488.

3 A. Filippov, V.M. Starov, D.R. Lloyd, S. Chakravarti, and S. Glaser, *Sieve mechanism of microfiltration*, Journal of Membrane Science, 89 (1994) 199-213.

4 V. Starov, D.R. Lloyd, A. Filippov, and S. Glaser, *Sieve mechanism of microfiltration separation*, Separation Purification Technology, 26 (2002) 51-59.

5 J.A. Morehouse, D.R. Lloyd, B.D. Freeman, D.F. Lawler, K.M. Liechti, and E.B. Becker, *Modeling the stretching of microporous membranes*, Journal of Membrane Science, 283 (2006) 430-439.

6 K.W. Lawson and D.R. Lloyd, *Membrane distillation*, Journal of Membrane Science, 124 (1997) 1-25.

7 S. Bonyadi and T. Chung, *Flux enhancement in membrane distillation by fabrication of dual layer hydrophilic-hydrophobic hollow fiber membranes*, Journal of Membrane Science, 306 (2007) 134-146.

Appendix A: Nomenclature

Symbol	**Definition (Equation), Units**
a	Half-length of the major axis (5.10), μm
a_0	Average radius of two merging droplets (2.4), μm
a_t	Time shift factor (3.3)
A	Characteristic parameter of the membrane (5.6), μm^4
b	Half-length of the minor axis (5.10), μm
c	Concentration (5.2), #particles/volume
c_d	Concentration of particles greater than pore size *d* (5.2), #particles/volume
C_1	WLF constant (3.3)
C_2	WLF constant (3.3)
C_{10}	Neohookean constant describing hyperelasticity (3.1)
d	Pore diameter (5.1), μm
d_{max}	Maximum pore diameter, μm
d_{min}	Minimum pore diameter, μm
D	Particle diameter (5.2), μm
D_d^*	Diluent self-diffusion coefficient (2.2), cm^2/s
D_{obs}	Observed diameter of a cell (2.10), μm
D_{od}	Pre-exponential factor (2.3), cm^2, s
D_{max}	Maximum particle diameter (5.2), μm
D_{true}	True diameter of a cell (2.10), μm
D_1	Neohookean constant describing hyperelasticity (3.1)
E	Young's modulus (3.2), MPa
E_0	Glassy modulus (3.2), MPa
f_p	Distribution of particles (5.2)
f_m	Distribution of pore sizes (5.7)
h	Distance from the center of the cell to the plane on which the cell is fractured (2.10), μm
h_t	Total heat transfer coefficient (3.5), $J/(m^2sK)$
$\bar{I}_1$	First deviatoric strain invariant
j	Dimensionless flux
J	Dimensional flux (5.3), μm^3 permeate/(μm^2 s)
J^{el}	Elastic volume ratio (3.1)
J_0	Initial flux (5.6), μm^3 permeate/(μm^2 s)
K_{1d}	Free volume parameter for the diluent (2.3)
K_{2d}	Free volume parameter for the diluent (2.3), K
K_{1p}	Free volume parameter for the polymer (2.3)
K_{2p}	Free volume parameter for the polymer (2.3), K
l	Characteristic length scale, (5.1)
L	Length of membrane pore (5.5), μm
L_o	Initial length of a membrane sample (4.1), cm
L_f	Final length of a membrane sample (4.1), cm

M_w	Molecular weight (2.6), g/mol
n	Cross-link density of the polymer (2.7)
n	Number of particles (5.1)
N_m	Number of pores (5.6)
p_i	Prony series coefficient (3.2)
P	Probability a pore is open (5.1)
P_c	Capillary pressure (3.4), MPa
Q	Volumetric flow through an individual pore (5.5), μm^3
r	Radial position in spherical coordinates (5.21)
R	Radius of a spherical cell (2.10), μm
R	Radius of spherical particle (5.21), μm
S	Surface area of the membrane (5.1), μm
$\bar{t}$	Time (5.1), s
t	Dimensionless time (5.9)
t_f	Drying time in the first falling rate period (3.5), s
t_r	Relaxation time of two droplets (2.4), s
T	Temperature (2.3), K
T_c	Critical temperature of the system (2.6), K
T_g	Glass transition temperature (2.3), K
$T_{g,plasticizer}$	Glass transition temperature of the plasticizer (3.7), K
$T_{g, polymer}$	Glass transition temperature of the polymer (3.7), K
T_{ref}	Reference temperature for the WLF equation (3.3), K
T_s'	Surface Temperature (3.5), K
u	Integration variable for $\bar{t}$ (5.3), s
u_z	Stoke's flow velocity in the *z*-direction (5.20)
u_r	Stoke's flow velocity in the radial direction (5.20)
u_θ	Stoke's flow velocity in the angular direction (5.20)
U	Strain energy per unit of reference volume (3.1)
V	Volume (3.4), μm^3
V_d^*	Specific critical hole free volume of the diluent (2.3), cm^3/g
V_p^*	Specific critical hole free volume of the polymer (2.3), cm^3/g
$\tilde{V}_1$	Molar volume of diluent (2.7), cm^3/mole
W	Moisture content at a given time (3.5), % water, dry basis
W_c	Moisture content at the beginning of the first falling rate period (3.5), %water, dry basis
W_e	Equilibrium moisture content (3.5), % water, dry basis
w_{cryst}	Fraction of the polymer that is crystalline
x	Integration variable for pore diameter *d* (5.7), μm
x_{mp}	Fraction of the polymer-rich matrix phase that is polymer (2.8)
β	Contact angle (3.4), °
β	Parameter to characterize membrane pore influence (5.1)
γ	Surface tension (2.4), mN/m
γ	Free-volume overlap factor (2.2)

Δp	Pressure drop across the membrane (5.5), MPa
ε	Elongation (4.1), %
ζ	Integration variable for t (5.9)
θ	Angle (5.20), radians
κ	Experimentally determined constant (2.6)
λ	Latent heat of evaporation (3.5), J/kg
μ	Experimentally determined constant (2.6)
μ	Viscosity (5.5), cP
ξ	Ratio of the critical molar volumes of the diluent and polymer jumping units (2.2)
ρ_{amorph}	Density of the amorphous polymer (2.8), g/cm^3
ρ_{cryst}	Density of the crystalline polymer (2.8), g/cm^3
$\rho_{diluent}$	Density of the diluent (2.8), g/cm^3
$\rho_{L\text{-}L}$	Density of the liquid – liquid system (2.8), g/cm^3
ρ_{molten}	Density of the molten polymer (2.8), g/cm^3
ρ_s	Density of the bulk dry material (3.5), g/cm^3
$\rho_{S\text{-}L}$	Density of the solid – liquid system (2.8), g/cm^3
σ	Viscosity of solution (2.4), cP
σ_s	Yield stress, MPa
τ_i	Prony series coefficient, (3.2)
ϕ	Volume fraction of diluent (2.1)
ϕ_2	Volume fraction of polymer (2.7)
$\varphi(a/b,D/2b)$	Function representing the partial flow through a blocked elliptical pore (5.16)
χ	Interaction parameter (2.2)
ω_d	Weight fraction of diluent (2.2)
ω_p	Weight fraction of polymer (2.2)

Appendix B: Program Code

The files listed below are available electronically on a CD enclosed with this dissertation. Copies of the disk are available from D.R. Lloyd at *drl@che.utexas.edu* or by mail at:
Professor D.R. Lloyd
1 University Station, C0400
Austin, TX 78712-0231

Programs with names *.m run in MatLab, while programs with names *.cae run in ABAQUS CAE. DLOAD.f must be compiled by a FORTRAN compiler before it can be used in ABAQUS.

Chapter 2 – Matrix Solidification

- newestshrink.m
    - This program is the main program for modeling the growth of cells during matrix solidification of an iPP−DPE L−L TIPS system.
    - Requires a formatted text file with the results from a coalescence-induced-coalescence (CIC) run.
    - Requires IPPDPEbinodal.txt, which contains the binodal curve information as a set of coordinate pairs.
    - Requires the additional Matlab scripts: tally.m, merging3.m.
- tally.m
    - This script contains the code that determines the “sphere of influence” around each diluent droplet.
- merging3.m
    - This script determines which droplets are eligible to merge, the time required to merge, the position of the resultant drop, and the size of the resultant drop.

Chapter 3 – Drying of Microporous Membranes

- iPPcollapse.cae (and accompanying files)
    - This program set contains the part information, keywords, output database, and all other files required and generated by an ABAQUS model. The structure and material properties correspond to a cellular iPP – DPE membrane.
    - DLOAD.f contains the user defined FORTRAN function defining capillary forces over time and location.
- dSdVcalc.m
    - This Matlab program calculates the capillary forces for given sections of the membrane structure assuming a plane meniscus.
- sphere.m

    - This program is used to calculate the capillary forces generated in drying a sphere when the polymer – extractant have a defined contact angle.

Chapter 4 – Modeling of uni-axial elongation of track-etch membranes

- 2micronPET.cae (and accompanying files)
    - This program set contains the part information, keywords, output database, and all other files required and generated by an ABAQUS model. It corresponds to a range of stretches up to 35% of a membrane with a nominal 2 micrometer pore size.

Chapter 5 – Performance effects of pore shape change

- sieve.m
    - This Matlab program calculates the flux decline over time, volume of permeate generated, and pore size distribution over time for a membrane with circular pores using Equation 9 of Chapter 5.
- circularbrute.m
    - This Matlab program calculates the flux decline over time, volume of permeate generated, and pore size distribution over time for a membrane with circular pores using the discrete method.
- ellipticalsieve020508.m
    - This Matlab program calculates the flux decline over time, volume of permeate generated, and pore size distribution over time for a membrane with elliptical pores using Equation 19 of Chapter 5. This program requires that the user copy and paste the data in Table 1 of Chapter 5 into the variable “blockage” in order to calculate for flux through a partially blocked pore.
- ellipticalnormal.m
    - This Matlab program calculates the flux decline over time, volume of permeate generated, and pore size distribution over time for a membrane with elliptical pores using the discrete method. This program allows for distributions of the major axis, minor axis, and particle size. This program requires that the user copy and paste the data in Table 1 of Chapter 5 into the variable “blockage” in order to calculate for flux through a partially blocked pore.
- stokes.m
    - This Matlab program calculates the fractional flow compared to initial flow through a partially blocked pore as described in section 5.2.4.

Appendix C: Shrinkage dependence on extractant parameters

Table C1. Final cell diameters of membranes studied during the drying process.
Table C2. Contact angles for EVAL44 and various extractants.

Results for EVAL44 – glycerol membranes made from a 50 – 50 wt% by casting on a 150°F temperature controlled texture wheel.

Figure C1. Cell diameter as a function of the total solubility parameter for various families of extractants.
Figure C2. Cell diameter as a function of the difference of total solubility parameters between the polymer and extractant for various families of extractants.
Figure C3. Cell diameter as a function of the cohesive energy density (CED) for various families of extractants.
Figure C4. Cell diameter as a function of the cohesive energy density (CED) difference between the polymer and extractant for various families of extractants.
Figure C5. The relative cell size plotted as a function of a dimensionless grouping.
Figure C6. The relative cell size plotted as a function of a dimensionless grouping.
Figure C7. The relative cell size of the dried membrane plotted against the diffusion coefficient of the extractant in air.
Figure C8. The relative cell size of the dried membrane plotted against the heat of vaporization of the extractant.
Figure C9. The relative cell size of the dried membrane plotted against the boiling point of the extractant.
Figure C10. The relative cell size of the dried membrane plotted against the dielectric constant of the extractant.

Comparisons between membranes.

Figure C11. Relative cell size (final relative material volume for PE – mineral oil) as a function of the total solubility parameter.
Figure C12. Relative cell size (final relative material volume for PE – mineral oil) as a function of the dispersive solubility parameter.
Figure C13. Cell size as a function of the polar solubility parameter.
Figure C14. Cell size as a function of the hydrogen bonding solubility parameter.

Table C1. Final cell diameters of membranes studied during the drying process.

Extractant	Surface Tension[1] mN/m	Final Cell Diameter Micrometers	Final Cell Standard Deviation Micrometers
EVAL44 – glycerol, 50 – 50 wt%, 150°F take-up wheel			
Pentane	15.47	0.324	0.001
Hexane	17.98	0.273	0.001
Heptane	19.78	0.300	0.001
Octane	21.08	0.305	0.016
Acetone	23.10	0.262	0.052
Methyl ethyl ketone	23.96	0.332	0.019
2-pentanone	24.48	0.304	0.017
2-heptanone	26.12	0.293	0.010
Methanol	23.55	0.158	0.008
Ethanol	23.39	0.150	0.004
Pentanol	26.46	0.286	0.007
Hexanol	25.9	0.308	0.018
2-propanol	22.4	0.229	0.021
Cyclohexane	24.65	0.368	0.022
Water	72.50	0.173	0.009
EVAL44 – glycerol, 50 – 50 wt%, 170°F take-up wheel			
Pentane	15.47	0.560	0.011
Cyclohexane	24.65	0.564	0.035
Acetone	23.10	0.355	0.007
2-propanol	22.4	0.361	0.013
Methanol	23.55	0.257	0.024
Water	72.50	0.350	0.022
EVAL44 – glycerol, 40 – 60 wt%, 170°F take-up wheel			
Pentane	15.47	0.973	0.035
Cyclohexane	24.65	0.899	0.008
Acetone	23.10	0.815	0.013
2-propanol	22.4	0.857	0.004
Methanol	23.55	–	–
Water	72.50	–	–

[1] Values obtained from Yaws' Handbook of Thermodynamic and Physical Properties of Chemical Compounds.

Table C2. Contact angles for EVAL44 and various extractants.

Extractant	**Contact Angle, degrees**
Acetone	10.0
Pentane	5.0
2-propanol	7.5
Cyclohexane	9.5
Methanol	11.6
Water	54.7

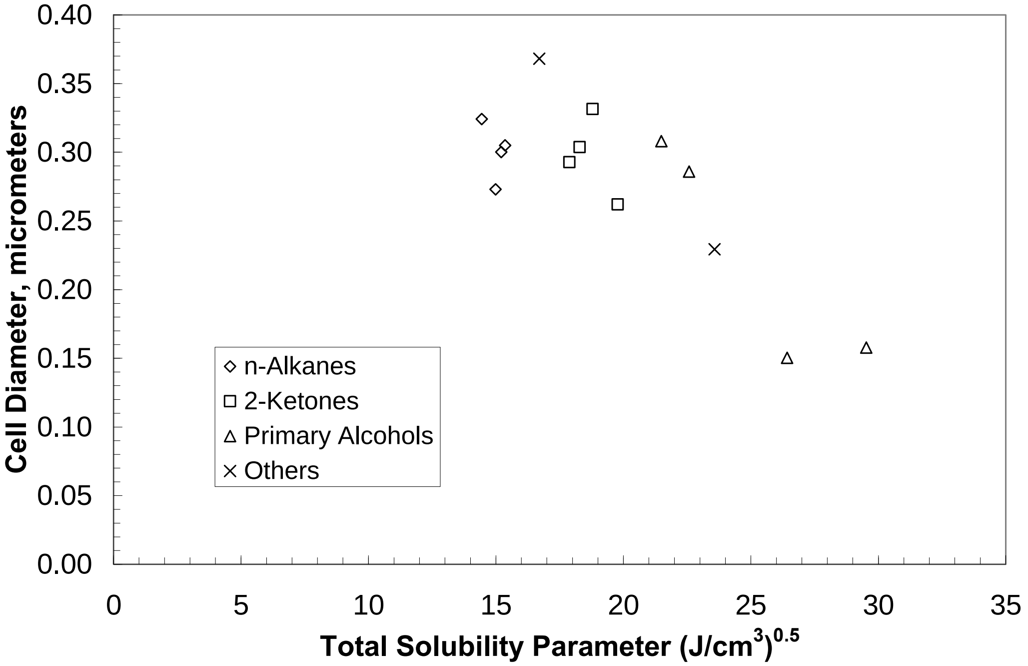

Figure C1. Cell diameter as a function of the total solubility parameter for various families of extractants.

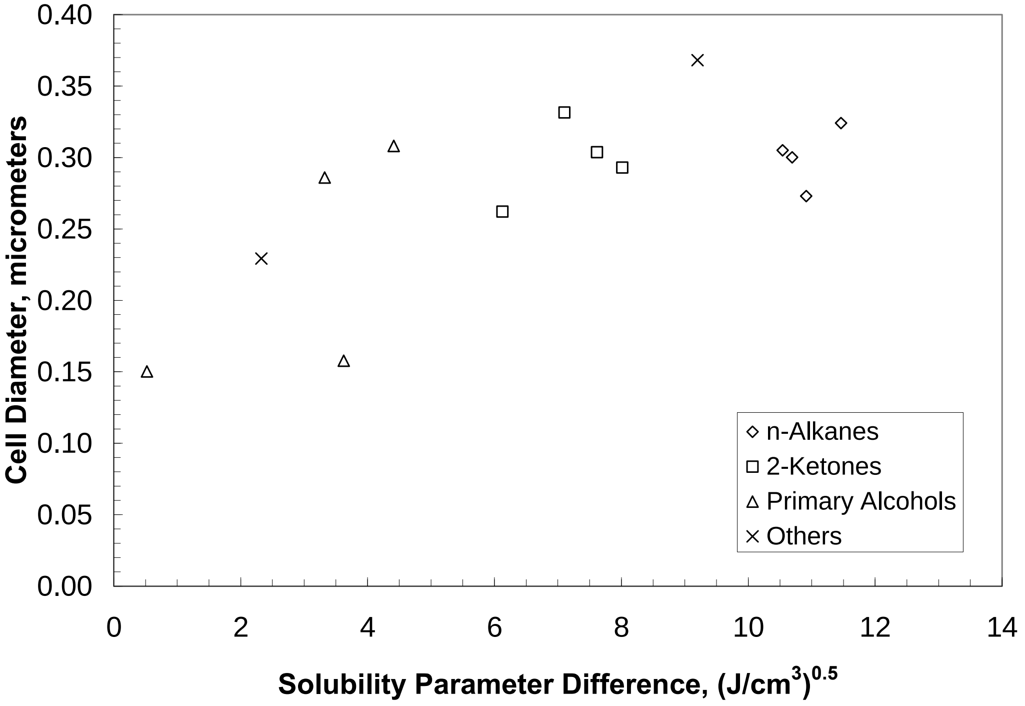

Figure C2. Cell diameter as a function of the difference of total solubility parameters between the polymer and extractant for various families of extractants.

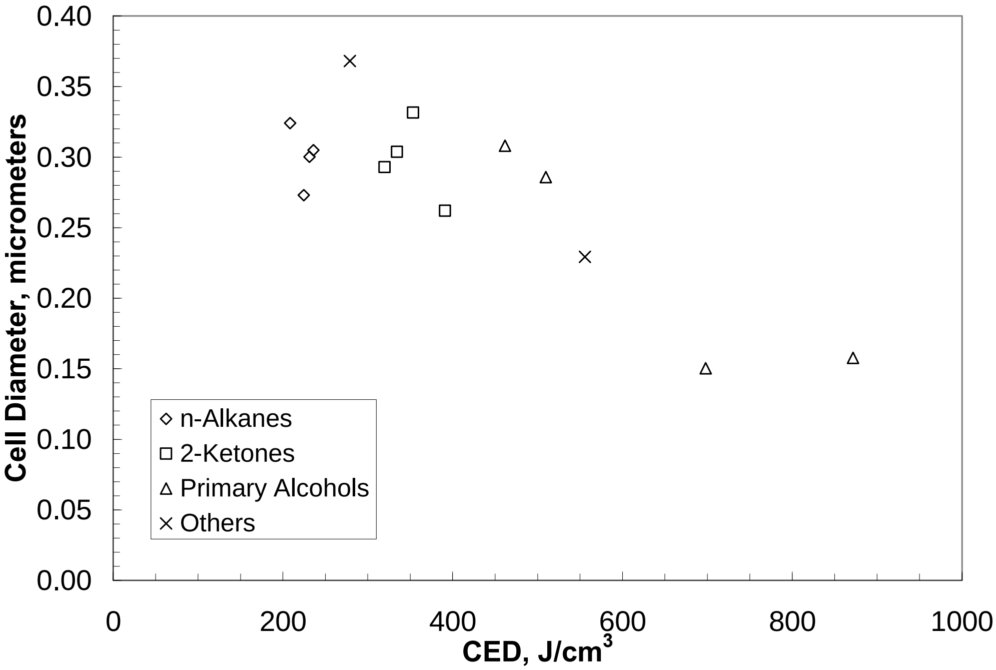

Figure C3. Cell diameter as a function of the cohesive energy density (CED) for various families of extractants.

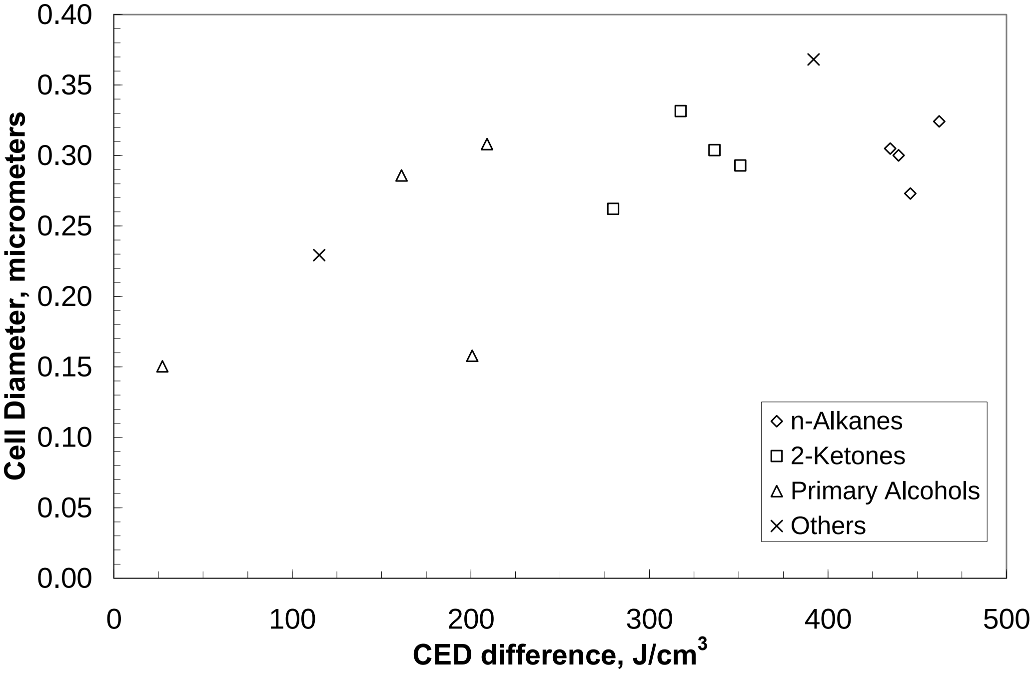

Figure C4. Cell diameter as a function of the cohesive energy density (CED) difference between the polymer and extractant for various families of extractants.

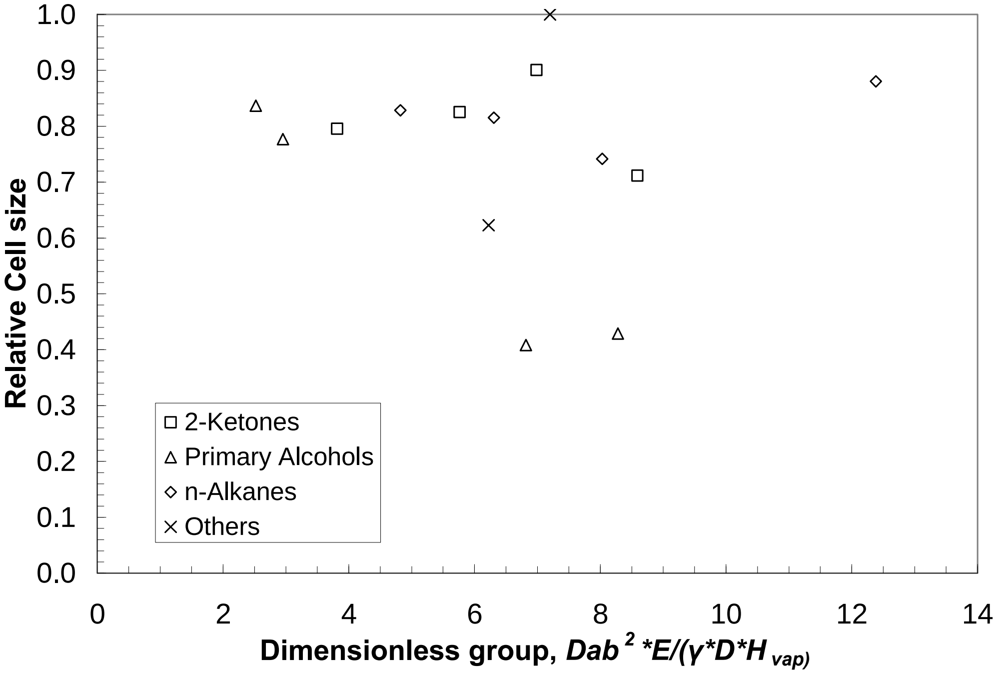

Figure C5. The relative cell size plotted as a function of a dimensionless grouping where D_{ab} is the diffusion coefficient of the extractant in air, E is Young's modulus, γ is surface tension, D is the cell diameter, and H_{vap} is the heat of vaporization of the extractant.

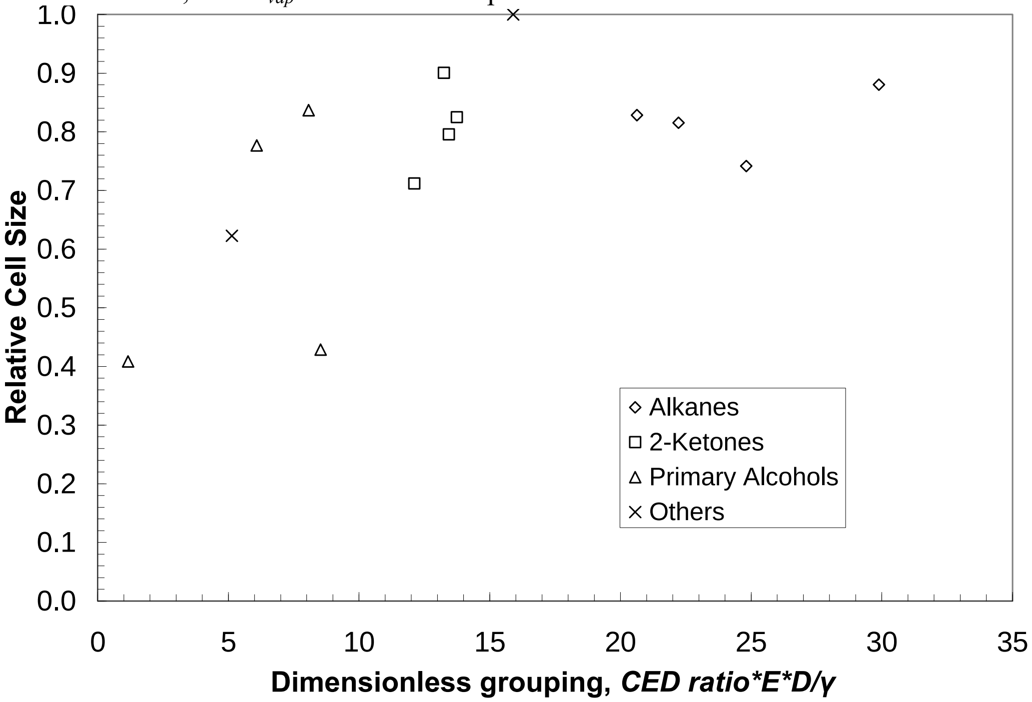

Figure C6. The relative cell size plotted as a function of a dimensionless grouping where *CED ratio* is the ratio of the cohesive energy density of the polymer to the extractant, E is Young's modulus, D is the cell diameter, and γ is surface tension.

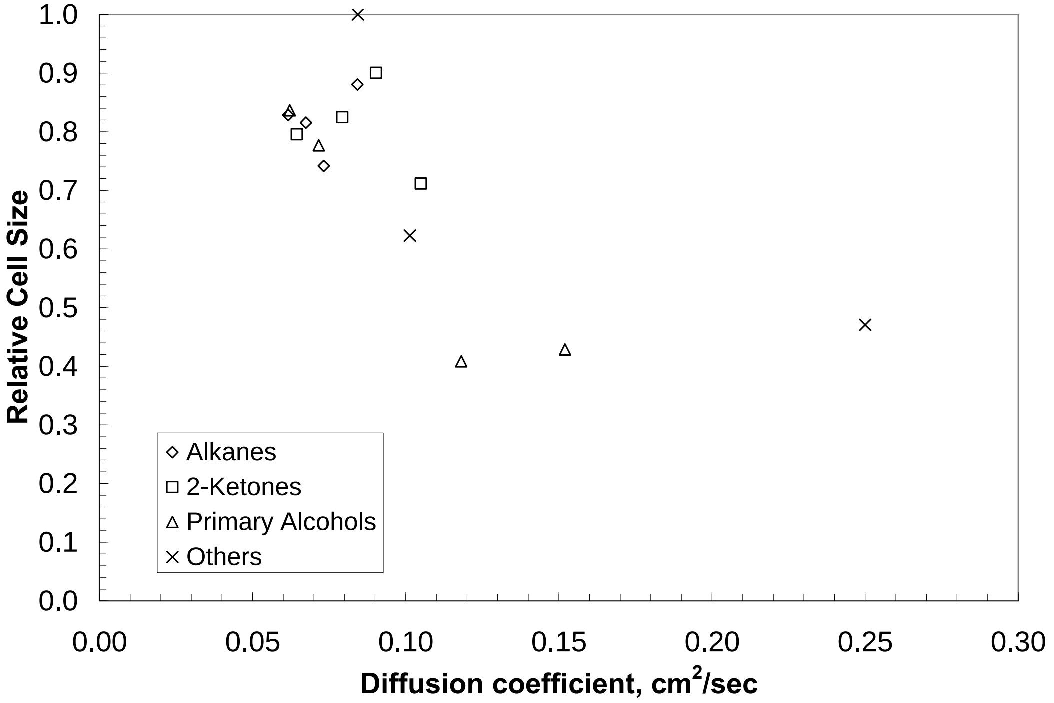

Figure C7. The relative cell size of the dried membrane plotted against the diffusion coefficient of the extractant in air.

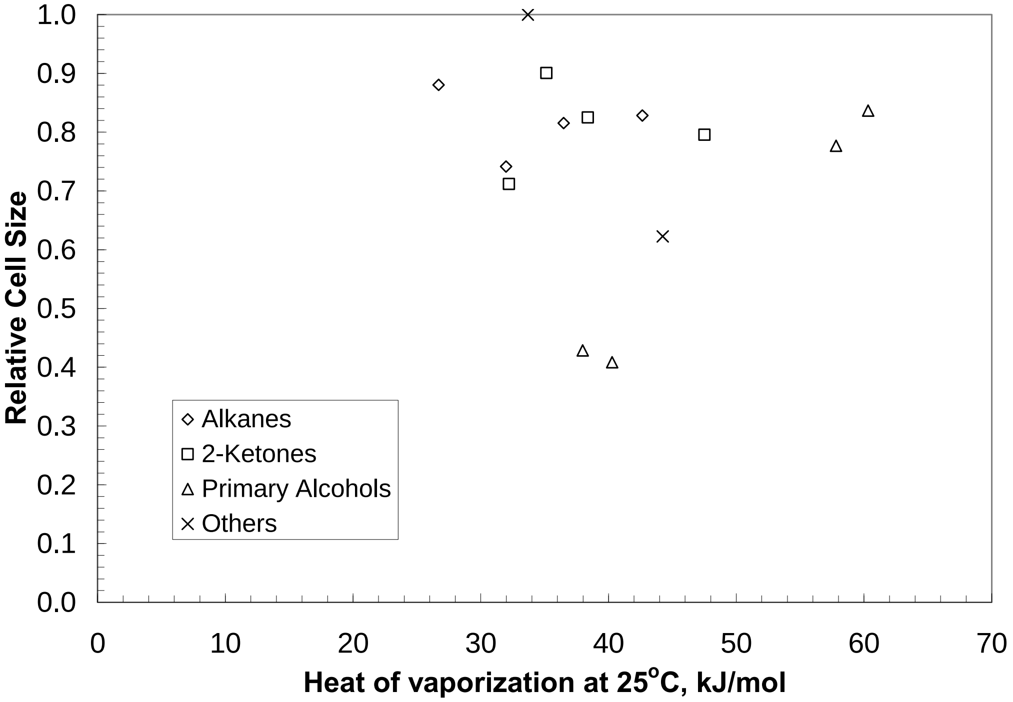

Figure C8. The relative cell size of the dried membrane plotted against the heat of vaporization of the extractant.

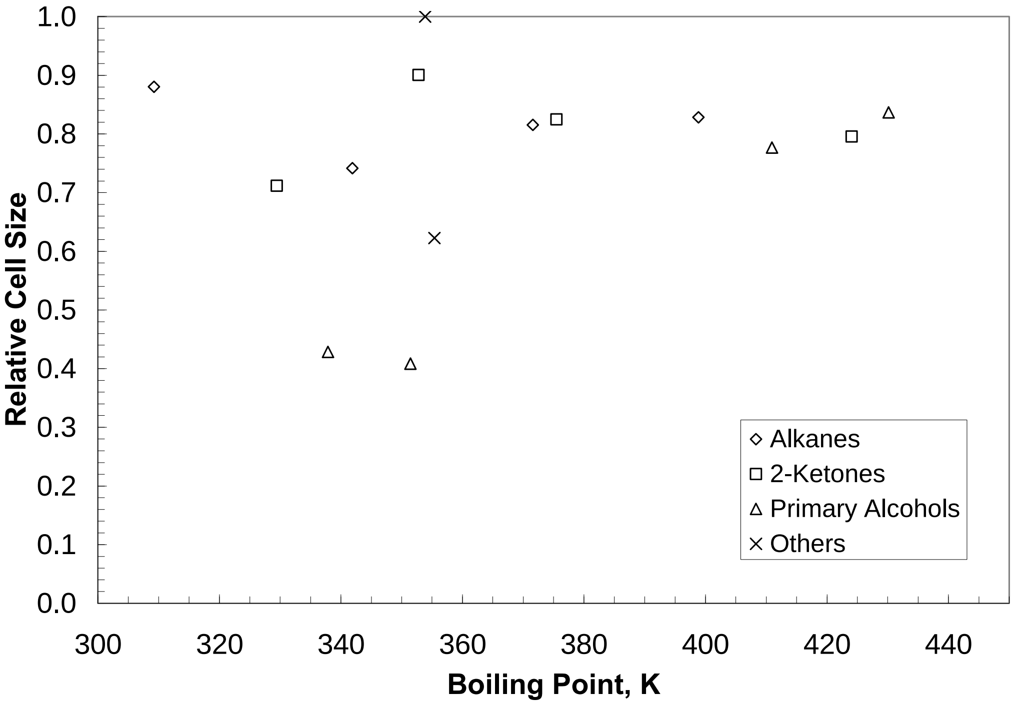

Figure C9. The relative cell size of the dried membrane plotted against the boiling point of the extractant.

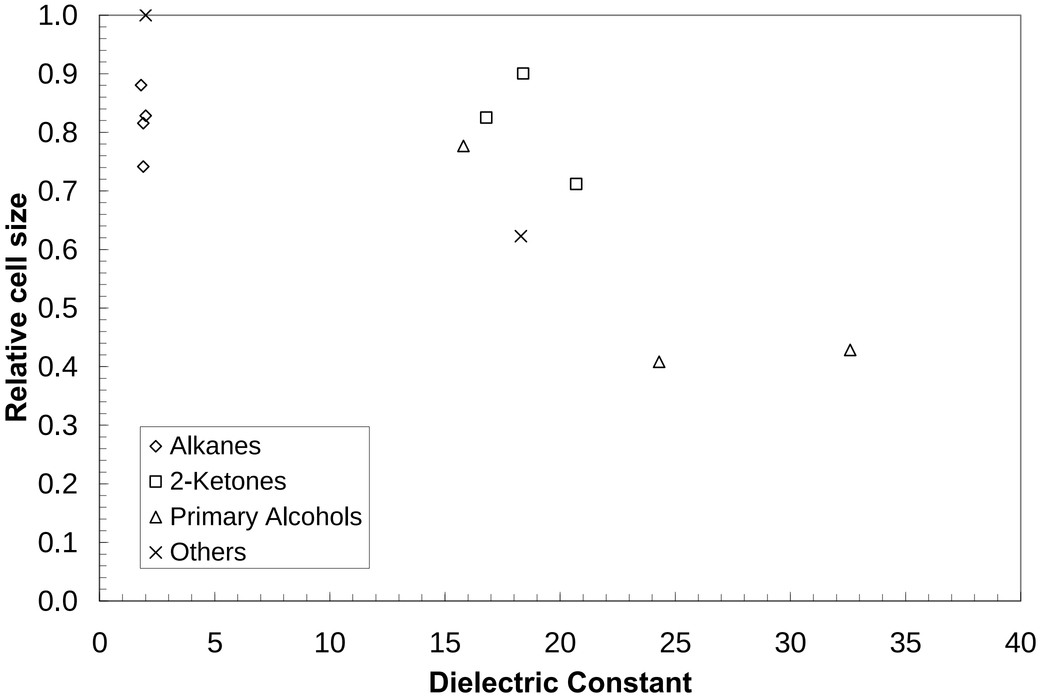

Figure C10. The relative cell size of the dried membrane plotted against the dielectric constant of the extractant.

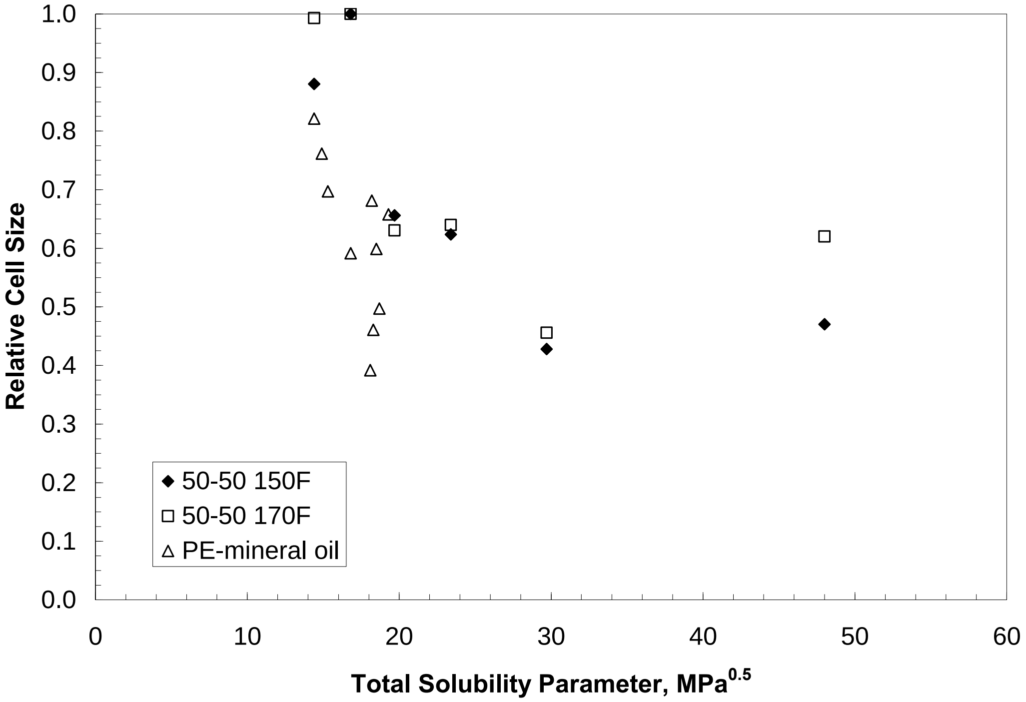

Figure C11. Relative cell size (final relative material volume for PE – mineral oil) as a function of the total solubility parameter.

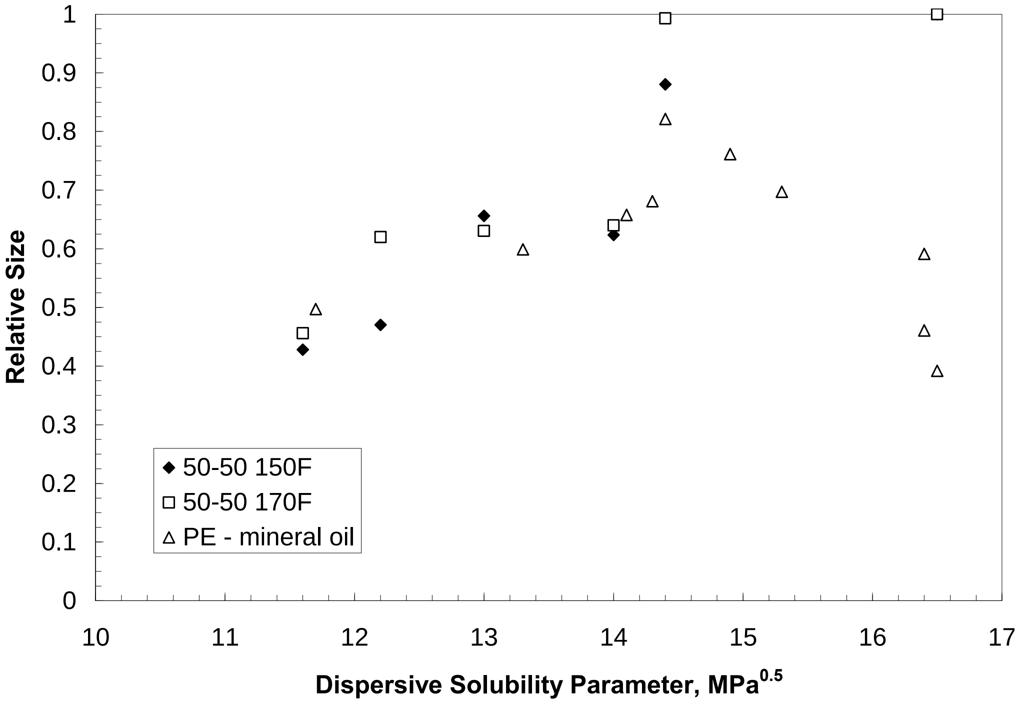

Figure C12. Relative cell size (final relative material volume for PE – mineral oil) as a function of the dispersive solubility parameter.

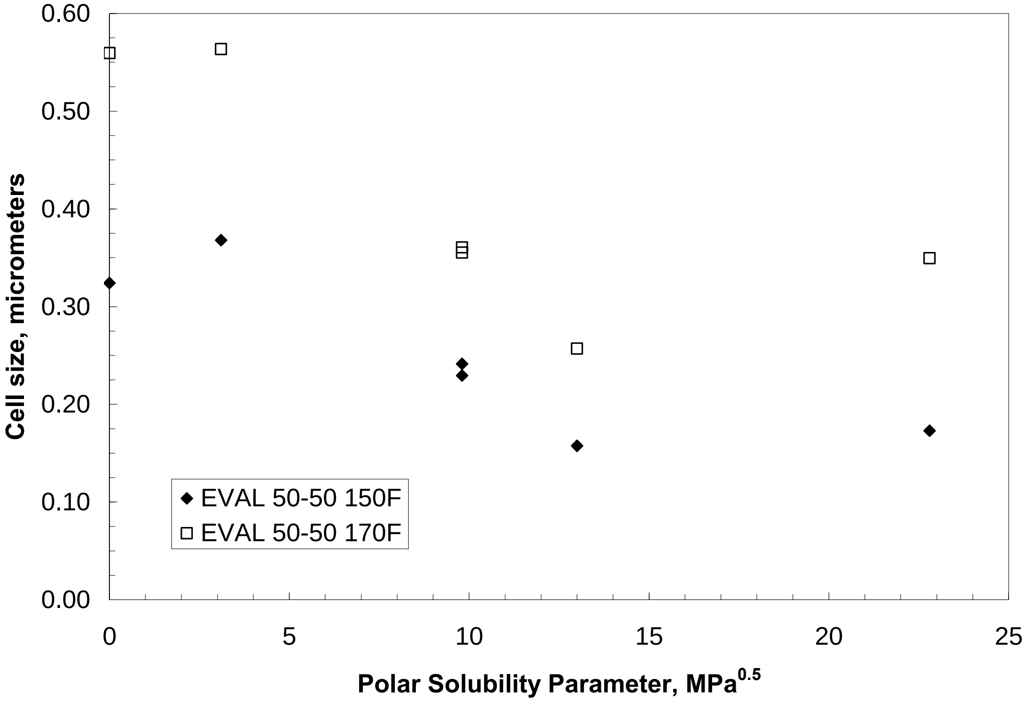

Figure C13. Cell size as a function of the polar solubility parameter.

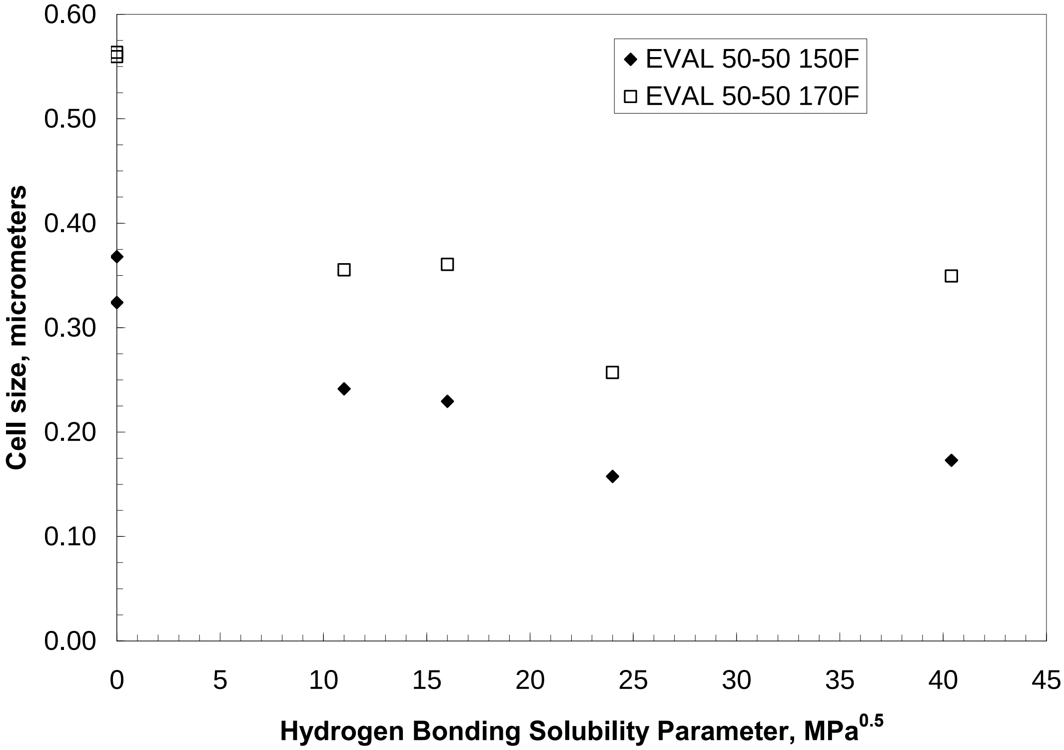

Figure C14. Cell size as a function of the hydrogen bonding solubility parameter.

Bibliography

K.M. Abraham, *Directions in secondary lithium battery research and development*, Electrochimica Acta, 38 (1993) 1233-1248.

W. Admassu, *Process for drying water - wet polycarbonate membranes*, US Patent 4843733, 1989.

A. Alwattari, *Thermally induced phase separation of isotactic polyproylene and hexamethylbenzene*, Dissertation, The University of Texas at Austin, 1990.

P. Apel, *Track etching technique in membrane technology*, Radiation Measurements, 34 (2001) 559-566.

S. Atlung, K. West, and T. Jacobsen, *Dynamic aspects of solid solution cathodes for electrochemical power sources*, J. of Electrocheical Science and Technology, 126 (1979) 1311-1321.

M. Avrami, *Kinetics of phase change, I: General theory*, Journal of Chemical Physics, 7 (1939) 1103-1112.

M. Avrami, *Kinetics of phase change, II: Transformation-time relations for random distribution of nuclei*, Journal of Chemical Physics, 8 (1940) 212-224.

M. Avrami, *Kinetics of phase change, III: Granulation, phase change and microstructure*, Journal of Chemical Physics, 9 (1941) 177-184.

B.F. Barton, P.D. Graham, and A.J. McHugh, *Dynamics of Spinodal Decomposition in Polymer Solutions Near a Glass Transition*, Macromolecules, 31 (1998) 1672-1679.

B.F. Barton and A.J. McHugh, *Kinetics of Thermally Induced Phase Separation in Ternary Polymer Solutions. I. Modeling of Phase Separation Dynamics*, Journal of Polymer Science: Part B: Polymer Physics, 37 (1999) 1449-1460.

P. Bassereau, D. Brodbeck, T.P. Russell, H.R. Brown, and K.R. Shull, *Topological coarsening of symmetric diblock copolymer films: model 2D systems*, Physical Review Letters, 71 (1993) 1716-1719.

M.T. Batarseh, *Formation of anisotropic hollow fiber membranes via TIPS*, Dissertation, The University of Texas at Austin, 1999.

M.A.M. Beerlage, *Polyimide ultrafiltration membranes for non-aqueous systems*, Dissertation, University of Twente, 1994.

A.R. Berker, *Integration des equations du mouvement d'un fluid visqueux incompressible*, Encyclopedia of Physics, vol. 8, S. Flugge, Ed. Berlin: Springer (1963).

R.B. Bird, W.E. Stewart, and E.N. Lightfoot, *Transport Phenomena*, 2nd ed, John Wiley and Sons Inc., New York, 2002.

S. Bonyadi and T. Chung, *Flux enhancement in membrane distillation by fabrication of dual layer hydrophilic-hydrophobic hollow fiber membranes*, Journal of Membrane Science, 306 (2007) 134-146.

J. Brandrup, E.H. Immergut, and E.A. Grulke, (Eds.), Polymer Handbook, 4th ed., John Wiley & Sons, New York, 1999.

H. Brenner, *The slow motion of a sphere through a viscous fluid towards a plane surface*, Chem. Eng. Sci., 16 (1961) 242-251.

C.J. Brinker and G.W. Scherer, *Sol-gel science: the physics and chemistry of sol-gel processing*, Academic Press, Boston, 1990. pages 908.

G. Brown and A. Chakrabarti, *Phase separation dynamics in off-critical polymer blends*, Journal of Chemical Physics, 98 (1993) 2451-2458.

B. Budiansky, J.W. Hutchinson, S. Slutsky, *Void Growth and Collapse in Viscous Solids*), Mechanics of Solids, Pergamon Press, Oxford, 1982, pp. 13-45.

G.T. Caneba and D.S. Soong, *Polymer membrane formation through the thermal-inversion process. 1. Experimental study of membrane structure formation*, Macromolecules, 18 (1985) 2538-2545.

G.T. Caneba and D.S. Soong, *Polymer membrane formation through the thermal-inversion process. 2. Mathematical modeling of membrane structure formation*, Macromolecules, 18 (1985) 2545-2555.

A.J. Castro, *Method for making microporous products*, US Patent 4,247,498, 1980.

M. Chandler and A. Zydney, *Effects of membrane pore geometry on fouling behavior during yeast cell microfiltration*, Journal of Membrane Science, 285 (2006) 334-342.

Y.C. Chou and W.I. Goldburg, *Angular distribution of light scattered from critically quenched liquid mixtures*, Physical Review A, 23 (1981) 858-864.

B.E. Clements, *Damage Evolution in Viscoelastic Polymers*, AIP Conference Proceedings, 505 (1999) 527-530.

P.W. Clinnton, *Microporous materials of ethylene-vinyl alcohol copolymer and method of making same*, US Patent 5,962,544, 1997.

M.B. Douglas, D.N. Gray, B. Watson, and C.S. Youngen, *Poly(sulfone-alpha-olefin) composite permselective membrane article for use in blood oxygenation*, US Patent 5,391,580, 1995.

C. Duclos-Orsello, W. Li, and C. Ho, *A three mechanism model to describe fouling of microfiltration membranes*, Journal of Membrane Science, 280 (2006) 856-866.

J.L. Duda, J.S. Vrentas, S.T. Ju, and H.T. Liu, *Prediction of Diffusion Coefficients for Polymer-Solvent Systems*, AIChE Journal, 28 (1982) 279-285.

J.D. Eshelby, *The determination of the elastic field of an ellipsoidal inclusion, and related problems*, Proceedings of the Royal Society (London), A241 (1957) 376-396.

EVALCA, *Technical Bulletin No. 100, Moisture absorption and drying of EVAL resins*, (2000) 4.

EVALCA, *EVAL E151 Data Sheet*, (2004).

A. Filippov, V.M. Starov, and S.V. Gleizer, *Mathematical modelling of the microfiltration process by means of a probabilistic-sieve mechanism*, Soviet journal of Water Chemistry and Technology, 12 (1990) 483-488.

A. Filippov, V.M. Starov, D.R. Lloyd, S. Chakravarti, and S. Glaser, *Sieve mechanism of microfiltration*, Journal of Membrane Science, 89 (1994) 199-213P. Flory and J. Rehner, *Statistical Mechanics of Cross-Linked Polymer Networks, II. Swelling*, Journal of Chemical Physics, 11 (1943) 521-526.

C.V. Funk and D.R. Lloyd, *Zeolite-filled microporous mixed matrix (ZeoTIPS) membranes: Prediction of gas separation performance.*, Journal of Membrane Science, 313 (2008) 224-231.

A.J. Goldmann, R.G. Cox, and H. Brenner, *Slow viscous motion of a sphere parallel to a plane wall. 1. Motion through a quiescent fluid*, Chem. Eng. Sci., 22 (1967) 637-652.

A.J. Goldmann, R.G. Cox, and H. Brenner, *Slow viscous motion of a sphere parallel to a plane wall. 2. Couette flow.*, Chem. Eng. Sci., 22 (1967) 653-660.

D. Graebling, R. Muller, and J.F. Palierne, *Linear Viscoelastic Behavior of Some Incompatible Polymer Blends in the Melt. Interpretation of Data with a Model of Emulsion of Viscoelastic Liquids*, Macromolecules, 26 (1993) 320-329.

P.D. Graham and A.J. McHugh, *Kinetics of thermally induced phase separation in a crystallizable polymer solution*, Macromolecules, 31 (1998) 2565-2558.

P.D. Graham, B.F. Barton, and A.J. McHugh, *Kinetics of thermally induced phase separation in ternary polymer solutions. II. Comparison of theory and experiments*, Journal of Polymer Science: Part B: Polymer Physics, 37 (1999) 1461-1467.

P.D. Graham, A.J. Pervan, and A.J. McHugh, *The dynamics of thermal-induced phase separation in PMMA solutions*, Macromolecules, 30 (1997) 1651-1655.

A.L. Gurson, *Continuum theory of ductile rupture by void nucleation and growth: Part 1. Yield criteria and flow rules for porous media.*, Journal of Engineering Materials and Technology, Transactions of the ASME, 99 (1977) 2-15.

A. Gusev, *Representative volume element size for elastic composites: a numerical study*, J. Mech. Phys. Solids, 45 (1997) 1449-1459.

C.K. Haas and J.M. Torkelson, *2D coarsening in phase-separated polymer solutions: dependence on distance from criticality*, Physical Review Letters, 75 (1995) 3134-3137.

C.K. Haas and J.M. Torkelson, *Two-dimensional coarsening and phase separation in thin polymer solution films*, Physical Review E, 55 (1997) 3191-3201.

T. Hasegawa and T. Kondo, *Polyethylene microporous film and process for producing the same*, US Patent 6,127,438, 2000.

T. Hasegawa and T. Kondo, *Microporous polyethylene membranes having low fusing temperatures*, US Patent 6,168,858, 2001.

T. Hashimoto, J. Kumaki, and H. Kawai, *Time-resolved light scattering studies on kinetics of phase separation and phase dissolution of polymer blends. 1. Kinetics of phase separation of a binary mixture of polystyrene and poly(vinyl methyl ether)*, Macromolecules, 16 (1983) 641-648.

Z. Hashin, *Viscoelastic Behavior of Heterogeneous Media*, Journal of Applied Mechanics, 32 (1965) 630-636.

W.C. Hiatt, G.H. Vitzthum, K.B. Wagener, K. Gerlach, and C. Josefiak, *Microporous membranes via upper critical temperature phase separation*, in: D.R. Lloyd (Ed.), Materials Science of Synthetic Membranes, ACS Symposium Series, #269, ACS Press, Washington, DC, 1985, pp. 229-244.

K. Hibbitt, and Sorensen, *ABAQUS Theory Manual*, 1998, pp. 4.6.1-1 - 4.7.2-10.

J.A. Howell, O. Velicangil, M.S. Le, and A.L. Herrera-Zeppelin, *Ultrafiltration of protein solutions*, Annals of the New York Academy of Sciences, 369 (1981) 355-366.

R.B. Isaacson and H.S. Bierenbaum, *Process for preparing microporous film*, US Patent 3,558,764, 1971.

P. Jacoby, C.W. Bauer, S.R. Clingman, and W.T. Tall, *Oriented polymeric microporous films*, USA Patent 5,317,035, 1992.

F.N. Kemmer (Ed.), *The NALCO Water Handbook*, 2nd ed, McGraw-Hill, New York, 1987.

R.E. Kesting, *Synthetic polymeric membranes: a structural perspective*, 2nd ed, John Wiley and Sons, New York, 1985.

S.S. Kim and D.R. Lloyd, *Microporous membrane formation via thermally-induced phase separation. III. Effect of thermodynamic interactions on the structure of isotactic polypropylene membranes*, Journal of Membrane Science, 64 (1991) 13-29.

K.E. Kinzer, *Oriented microporous films*, US Patent 4,867,881, 1989.

K.E. Kinzer, *Method for preparing oriented microporous film*, US Patent 5,238,619, 1993.

S. Kosvintsev, R. Holdich, I. Cumming, and V. Starov, *Modelling of dead-end microfiltration with pore blocking and cake formation*, Journal of Membrane Science, 208 (2002) 181-192.

S. Kosvintsev, I. Cumming, R. Holdich, D.R. Lloyd, and V. Starov, *Seive mechanism of microfiltration separation*, Colloids and Surfaces, 230 (2004) 167-182.

J. Lal and R. Bansil, *Light-scattering study of kinetics of spinodal decomposition in a polymer solution*, Macromolecules, 24 (1991) 290-297.

F.C. Laman, M.A. Gee, and J. Denovan, *Impedance studies for separators in rechargeable lithium batters*, J. of Electrochm. Soc., 140 (1993) L51-L53.

J.B. Laurindo and M. Prat, *Numerical and experimental network study of evaporation in capillary porous media. Drying rates*, Chemical and Engineering Science, 53 (1998) 2257-2269.

K.W. Lawson and D.R. Lloyd, *Membrane distillation. II. Direct contact MD*, Journal of Membrane Science, 120 (1996) 123-133.

K.W. Lawson and D.R. Lloyd, *Membrane distillation*, Journal of Membrane Science, 124 (1997) 1-25.

A. Laxminarayan, *The kinetics of membrane formation via thermally induced liquid-liquid phase separation*, Dissertation, The University of Texas at Austin, 1994.

D. Li, W.B. Krantz, A.R. Greenburg, and R.L. Sani, *Membrane formation via thermally induced phase separation (TIPS): Model development and validation*, Journal of Membrane Science, 279 (2006) 50-60.

G.B.A. Lim, *Effects of nucleating agent on thermally induced phase separation membrane formation*, Dissertation, The University of Texas at Austin, 1990.

D.R. Lloyd, K.E. Kinzer, and H.S. Tseng, *Microporous membrane formation via thermally-induced phase separation. I. Solid-liquid phase separation*, Journal of Membrane Science, 52 (1990) 239-261.

D.R. Lloyd, S.S. Kim, and K.E. Kinzer, *Microporous membrane formation via thermally-induced phase separation. II. Liquid-liquid phase separation*, Journal of Membrane Science, 64 (1991) 1-11.

J. Li and G.J. Weng, *A unified approach from elasticity to viscoelasticity to viscoplasticity of particle reinforced solids*, International Journal of Plasticity, 14 (1998) 293-208.

J. Li and G.J. Weng, *Void growth in viscoelastic polymeric materials*, Mechanics of Plastics and Plastic Composites, ASME 1995, 68 (1995) 409-421.

S. Loeb and S. Sourirajan, *Sea water demineralization by means of an osmotic membrane*, Advan. Chem. Ser. (ACS), 38 (1963) 117.

X.L. Luo, *Operator splitting algorithm for viscoelastic flow and numerical analysis for flow around a sphere in a tube*, J. Non-Newtonian Fluid Mech., 63 (1996) 121-140.

P. Manos, *Membrane Drying Process*, US Patent 4080743, 1978.

D.S. Martula, T. Hasegawa, D.R. Lloyd, and R.T. Bonnecaze, *Coalescence-induced coalescence of inviscid droplets in a viscous fluid*, Journal of Colloid and Interface Science, 232 (2000) 241-253.

D.S. Martula, *Coalescence-induced coalescence*, Dissertation, The University of Texas at Austin, 2000.

D.S. Martula, R.T. Bonnecaze, and D.R. Lloyd, *The effects of viscosity on coalescence-induced coalescence*, International Journal of Multiphase Flow, 29 (2003) 1265-1282.

T. Masuoka, O. Hirasa, M. Onishi, and Y. Seita, *Porous hydrophilic polypropylene membrane, method for production thereof, and blood plasma separation apparatus*, US Patent 5,186,835, 1993.

H. Matsuyama, S. Berghmans, and D.R. Lloyd, *Formation of anisotropic membranes via thermally induced phase separation*, Polymer, 40 (1999) 2289-2301.

H. Matsuyama, M.-M. Kim, and D.R. Lloyd, *Effect of extraction and drying on the structure of microporous polyethylene membranes prepared via TIPS*, Journal of Membrane Science, 204 (2002) 413-418.

F.A. McClintock, *A Criterion for Ductile Fracture by the Growth of Holes*, Journal of Applied Mechanics (1968) 363-371.

S.B. McCray, D.T. Friesen, D.R. Sidwell, D.K. Lyon, and D. Sakashita, *Ethylene-vinyl alcohol hollow fiber membranes*, USA Patent 6,793,820, 2001.

R.M. McDonogh, unpublished results, cited by Beerlage.

K.S. McGuire, *Membrane formation via liquid-liquid thermally induced phase separation*, Dissertation, The University of Texas at Austin, 1995.

K.S. McGuire, A. Laxminarayan, and D.R. Lloyd, *Kinetics of droplet growth in liquid-liquid phase separation of polymer-diluent systems: experimental results*, Polymer, 36 (1995) 4951-4960.

K.S. McGuire, A. Laxminarayan, D.S. Martula, and D.R. Lloyd, *Kinetics of droplet growth in liquid-liquid phase separation of polymer-diluent systems: model development*, Journal of Colloid and Interface Science, 182 (1996) 46-58.

L.P. McMaster, *Aspects of liquid-liquid phase transition phenomena in multicomponent polymeric systems*, in: N.A. Platzer (Ed.), Advances in Chemistry Series, 142, Washington, 1975, pp. 43-65.

R. Mohan and F.W. Brust, *On Void Growth in Elastic-Nonlinear Viscous Solids Under Creep and cyclic creep conditions*, Journal of Engineering Materials and Technology, 122 (2000) 283-293.

M. Montoya, M.J. Abad, L. Barral, and C. Bernal, *Mechanical and fracture behavior of polypropylene/poly(ethylene-co-vinyl alcohol) blends compatibilized with ionomer Na*$^+$, Euroupean Polymer Journal, 42 (2006) 265-273.

J. Morehouse, *The effect of uni-axial stretching on microporous phase-separation membrane structure and performance*, Dissertation, University of Texas at Austin, 2006.

J.A. Morehouse, D.R. Lloyd, B.D. Freeman, D.F. Lawler, K.M. Liechti, and E.B. Becker, *Modeling the stretching of microporous membranes*, Journal of Membrane Science, 283 (2006) 430-439.

J.S. Mrozinski, *Microporous materials incorporating a nucleating agent and methods for making same*, US Patent 4,726,989, 1988.

J.S. Mrozinski, *Multi-layer laminates of microporous film*, US Patent 4,863,792, 1989.

J.S. Mrozinski, *Method for preparing microporous polyolefin shaped articles*, US Patent 5,238,623, 1993.

A. Nakajima and H. Fujiwara, *Phase relationships and thermodynamic interactions in isotactic polypropylene-diluent systems*, Journal of Polymer Science: Part A-2, 6 (1968) 723-733.

A. Needleman, *Void growth in an elastic-plastic medium*, Transaction of Journal of Applied Mechanics (1972) 964-970.

S. Nojima, K. Tsutsumi, and T. Nose, *Phase separation in polymer systems. II. Microscopic studies on a polystyrene and diisodecyl phthalate mixture*, Polymer Journal, 14 (1982) 289-294.

T. Nose and T. Van Tan, *Interfacial tension of demixed polystyrene-methylcyclohexane solution*, Journal of Polymer Science: Polymer Letters Edition, 14 (1976) 705-712.

R.H. Perry, D.W. Green, and J.O. Maloney, (Eds.), Perry's Chemical Engineering Handbook, 6th ed., McGraw-Hill, New York, 1984.

M. Prat, *Recent advances in pore-scale models for drying of porous media*, Chemical Engineering Journal, 86 (2002) 153-164.

J.R. Rice, D.M. Tracey, *On the ductile enlargement of voids in triaxial stress fields*, Journal of the Mechanics and Physics of Science, 17 (1969) 201-217.

M. Shang, H. Matsuyama, T. Maki, M. Teramoto, and D.R. Lloyd, *Preparation and characterization of poly(ethylene-co-vinyl alcohol) membranes via thermally induced liquid-liquid phase separation.*, Journal of Applied Polymer Science, 87 (2003) 853-860.

G.H. Shipman, *Microporous sheet material method of making and articles made therewith*, US Patent 4,539,256, 1985.

E.D. Siggia, *Late stages of spinodal decomposition in binary mixtures*, Physical Review A, 20 (1979) 595-605.

K.K. Sirkar and W.S. Ho, *Membrane Handbook*, 1st ed, van Nostrand Reinhold, New York, 1992.

R.J.M. Smit, W.A.M. Brekelmans, H.E.H. Meijer, *Predictive Modelling of the properties and toughness of polymeric materials: Part III: Macrostructural Deformation of rubber modified polymers*, Journal of materials science, 35 (2000) 2881-2892.

C.A. Smolders, J.J.v. Aartsen, and A. Steenbergen, *Liquid-liquid phase separation in concentrated solutions of non-crystallizable polymers by spinodal decomposition*, Kolloid-Z. u. Z. Polymere, 243 (1971) 14-20.

S. Sourirajan, *Reverse Osmosis*, Academic Press, New York, 1970.

S. Sourirajan and T. Matsurra, *Reverse osmosis/ultrafiltration process principles*, National Research Council Canada, Ottawa, Canada, 1985.

Z.H. Stachurski, G.H. Edward, M. Yin, and Y. Long, *Particle coarsening in polypropylene/polyethylene blends*, Macromolecules, 29 (1996) 2131-2137.

V.M. Starov, D.R. Lloyd, and A.M. Filippov, *Interaction of charged colloid particles with charged membranes*, Advances in Filtration and Separation Technology, 7 (1993) 446-450.

V. Starov, D.R. Lloyd, A. Filippov, and S. Glaser, *Sieve mechanism of microfiltration separation*, Separation Purification Technology, 26 (2002) 51-59.

A.C. Steenbrink, E. Van Der Giessen, P.D. Wu, *Studies of the Growth of voids in amorphous glassy polymers*, Journal of materials science, 33 (1998) 3163-3175.

U. Sundararaj and C.W. Macosko, *Drop breakup and coalescence in polymer blends: the effects of concentration and compatibilization*, Macromolecules, 28 (1995) 2647-2657.K. Takita, K. Kono, T. Takashima, and K. Okamoto, *Microporous polyolefin membrane and method of producing same*, US Patent 5,051,183, 1991.

J. Sweeney, P. Caton-Rose, P.D. Coates, *The modeling of large deformations of pre-oriented polyethylene*, Polymer, 43 (2001) 899-907.

K. Takita, K. Kono, T. Takashima, and K. Okamoto, *The preparation method for microporous polyolefin membrane*, Japan Patent 364,334, 1991.

K. Takita, K. Kono, T. Takashima, and K. Okamoto, *Microporous polyolefin membrane and method of producing same*, US Patent 5,051,183, 1991.

H. Tanaka, *New coarsening mechanisms for spinodal decomposition having droplet pattern in a binary fluid mixture: collision-induced collision*, Physical Review Letters, 72 (1994) 1702-1705.

H. Tanaka, *A new coarsening mechanism of droplet spinodal decomposition*, J. Chem. Phys., 103 (1995) 2361-2368.

H. Tanaka, *Coarsening mechanisms of droplet spinodal decomposition in binary fluid mixtures*, J. Chem. Phys., 105 (1996) 10099-10114.

H. Tanaka, *Preservation of droplet collision history in phase separation of a binary mixture*, Physical Review E, 54 (1996) R2216-R2219.

H. Tanaka, *New mechanisms of droplet coarsening in phase-separating fluid mixtures*, Journal of Chemical Physics, 107 (1997) 3734-3737.

M. Taniguchi, J. Kilduff, and G. Belfort, *Modes of natural organic fouling during ultrafiltration*, Enviromental Science and Technology, 37 (2003) 1676-1683.

Tracey, *Strain-Hardening and Interaction Effects on the Growth of Voids in Ductile Fracture*, Engineering Fracture Mechanics, 3 (1971) 301-315.

V. Tvergaard, *Influence of voids on shear band instabilities under plane strain conditions.*, International Journal of Fracture, 17 (1981) 389-407.

V. Tvergaard, *On localization in ductile materials containing spherical voids*, International Journal of Fracture, 18 (1982) 237-252.

I.G. Voigt-Martin, K.-H. Leister, R. Rosenau, and R. Koningsveld, *Kinetics of phase separation in polymer blends for deep quenches*, Journal of Polymer Science B: Polymer Physics, 24 (1986) 723-751.

K.D. Vos and F.O. Burris, *Drying cellulose acetate reverse osmosis membranes*, Industrial and Engineering Chemistry Product Research and Development, 8 (1969) 84-89.

J.S. Vrentas and J.L. Duda, *Molecular Diffusion in Polymer Solutions*, AIChE Journal, 25 (1979) 1-24.

J.S. Vrentas, J.L. Duda, and H.C. Ling, *Self Diffusion in Polymer-Solvent-Solvent Systems*, J. Polym. Sci., Polym. Phys. Ed., 22 (1984) 459-469.

A. Vrij, *Equation for the interfacial tension between demixed polymer solutions*, Journal of Polymer Science: Part A-2, 6 (1968) 1919-1932.

Y.F. Wang, *Crystallization of isotactic polypropylene and dotriacontane: a study of kinetics and morphology*, Dissertation, The University of Texas at Austin, 1989.

Y.M. Wang and G.J. Weng, *Self-Similar and transient void growth in viscoelastic media at low concentrations*, International Journal of Fracture, 61 (1993) 1-16.

S. Whitaker, *The method of volume averaging*, 13, Kluwer academic publishers, Dordrecht, 1999. Pages 219.

S. Whitaker, *Coupled transport in multiphase systems: a theory of drying*), Advances in heat transfer, 31, Academic Press, San Diego, 1998, pp. 1-158.

F.M. White, *Viscous Fluid Flow*, 2nd ed, McGraw-Hill, New York, 1991.

W.R. White and P. Wiltzius, *Real space measurement of structure in phase separating binary fluid mixtures*, Physical Review Letters, 75 (1995) 3012-3015.

B. Widom, *Phase separation in polymer solutions*, Physica A, 194 (1993) 532-541.

M.L. Williams, R.F. Landel, and J.D. Ferry, *The temperature dependence of relaxation mechanisms in amorphous polymers and other glass-forming liquids*, Journal of the American Chemical Society, 77 (1955) 3701-07.

N.-C. Wong and C.M. Knobler, *Light scattering studies of phase separation in isobutyric acid + water mixtures*, Journal of Chemical Physics, 69 (1978) 725-735.

L.S. Worrel, *Modification of Track-Etched Membrane Structure and Performance via Uniaxial Stretching*, Dissertation, The University of Texas at Austin, 2005.

L.S. Worrel, L.A. Shimko, J.A. Morehouse, D. R. Lloyd, B.D. Freeman, and D.F. Lawler, *Enhancement of Track-etched Membrane Performance via Stretching*, Separation and Purifications Technology, 53 (2007) 71-80.

J.D. Wu and K.M. Liechti, *Multiaxial and Time Dependent Behavior of a Filled Rubber*, Mechanics of Time-Dependent Materials (2000) 293-331.

C.L. Yaws, *Yaws' Handbook of Thermodynamic and Physical Properties of Chemical Compounds* Knovel, Norwich, 2003.

A.G. Yiotis, A.K. Stubos, A.G. Boudouvis, and Y.C. Yortsos, *A 2-D pore-network model of the drying of single-component liquids in porous media*, Advances in Water Resources, 24 (2001) 439-460.

A.G. Yiotis, A.G. Boudouvis, A.K. Stubos, I.N. Tsimpanogiannis, and Y.C. Yortsos, *Effect of liquid films on the drying of porous media*, AIChE Journal, 50 (2004) 2721-2737.

H. Yoshida, K. Tomizawa, and Y. Kobayashi, *Effect of annealing at temperatures around glass transition temperature on molecular orientation and shrinkage of ethylene-vinyl alcohol copolymers*, Journal of Applied Polymer Science, 24 (1979) 2277-2287.

L.J. Zeman and A.L. Zydney, *Microfiltration and Ultrafiltration*, Marcel Dekker, Inc., New York, 1996.

A.R. Zembrodt, *Air freshener with microporous membrane*, US Patent 4,948,047, 1990.

J.M. Zielinski and J.L. Duda, *Predicting Polymer/Solvent Diffusion Coefficients Using Free-Volume Theory*, AIChE Journal, 38 (1992) 405-415.

Vita

Patrick Loring Hanks was born in Arlington, Texas on January 26, 1983, the son of Kathy Berryhill Hanks and Nelson Legrand Hanks. He completed his secondary education at the Alabama School for Mathematics and Science in Mobile, AL in 2001. That fall he entered Auburn University and received a Bachelors of Chemical Engineering Degree, summa cum laude, University Honors Scholar in 2004. Patrick entered graduate school at the University of Texas at Austin in the fall of 2004 to pursue a doctoral degree in Chemical Engineering. He married Rose Marie Cummings on August 11, 2006. After graduation, Patrick will work for ExxonMobil Research and Engineering in Annandale, NJ.

Permanent address: 10306 Morado Cove, Apt 261, Austin, TX 78759
This dissertation was typed by the author.